Fakultät für Physik
Lehrstuhl für Physik funktionaler Schichtsysteme, E10

Spin-orbit interaction and confinement effects in low-dimensional electron systems studied by torque magnetometry and anisotropic magnetotransport

Dissertation von Florian Herzog

Fakultät für Physik
Lehrstuhl für Physik funktionaler Schichtsysteme, E10

Spin-orbit interaction and confinement effects in low-dimensional electron systems studied by torque magnetometry and anisotropic magnetotransport

Florian Herzog

Vollständiger Abdruck der von der Fakultät für Physik der Technischen Universität München zur Erlangung des akademischen Grades eines

Doktors der Naturwissenschaften

genehmigten Dissertation.

Vorsitzender: Univ.-Prof. Dr. Martin Zacharias

Prüfer der Dissertation:

1. Univ.-Prof. Dr. Dirk Grundler
2. Univ.-Prof. Dr. Alexander Holleitner

Die Dissertation wurde am 12.11.2015 bei der Technischen Universität München eingereicht und durch die Fakultät für Physik am 14.12.2015 angenommen.

Short Abstract

Spin-orbit interaction effects in planar InP/InGaAs heterostructures are investigated experimentally via beating patterns in the quantum oscillations of magnetization, chemical potential and magnetoresistance in high magnetic fields and at low temperatures. A detailed theoretical analysis allows to extract the relevant Rashba and Dresselhaus parameters as well as the anisotropic $\overline{\overline{g}}^*$-tensor. The measured magnetization of etched quantum dots reflects screening of the lateral confinement potential and edge depletion.

Spin-Bahn Kopplungseffekte in planaren InP/InGaAs Heterostrukturen werden experimentell untersucht. Quantenoszillationen der Magnetisierung, des chemischen Potentials und des Magnetwiderstandes bei hohen Magnetfeldern und niedrigen Temperaturen zeigen dafür charakteristische Schwebungsmuster. Anhand detaillierter theoretischer Analysen werden die relevanten Rashba- und Dresselhausparameter sowie der anisotrope $\overline{\overline{g}}^*$-Tensor bestimmt. Magnetisierungsmessungen an geätzten Quantenpunkten zeigen indirekt eine Abschirmung des lateralen Einschlusspotentials sowie Randverarmungseffekte.

Abstract

Semiconductor spintronics aims to explore new functionalities exploiting the electron spin degree of freedom. Anticipated device concepts for digital information processing are predicted to be faster, less power-consuming and could be combined with established semiconductor technology. Here, spin-orbit-interaction (SOI) effects are key to address the spin electronically. In particular, the Dresselhaus (D)- as well as the gate-tunable Rashba (R)-SOI effect were reported to be suitable for spin manipulation and spin filtering in semiconductor hetero- and nanostructures.

In this work, R- and D-SOI effects in asymmetric InP/InGaAs heterostructures featuring a two-dimensional electron system (2DES) are investigated via beating patterns in the quantum magneto-oscillations of magnetization M, chemical potential μ and magnetoresistance ρ_{xx}. These quantities are addressed experimentally by cantilever magnetometry and magnetotransport measurements as a function of an external magnetic field B at low temperatures. Furthermore, confinement effects in laterally etched InP/InGaAs quantum dot ensembles are studied in the quantum oscillatory $M(B)$. All experimental data are compared with theoretical models describing relevant single-particle energies, facilitating the prediction of relevant beat node positions and enabling a direct simulation of the thermodynamic quantities $M(B)$ and $\mu(B)$. In the following, the individual results are briefly summarized:

The thermodynamic quantities $M(B)$ and $\mu(B)$ of gated InP/InGaAs 2DES samples are measured simultaneously during the same cool-down process via a combined static operation and resonant excitation of micromechanical cantilevers. Both quantities exhibit beating patterns in the $1/B$-periodic magneto-oscillations, which are attributed to SOI. Here, a sensitivity enhancement due to resonant excitation enables to resolve two beat nodes in $\mu(B)$, while only a single beat node is detected in $M(B)$. By fitting the experimental beat node positions with theoretical predictions, absolute values of both R- and D-SOI

constants, α_{R} and β_{D}, are extracted from the data. The analysis yields $\alpha_{\mathrm{R}} = 4.44 \times 10^{-11}\,\mathrm{eVm}$ and $\beta_{\mathrm{D}} \approx 0.1\alpha_{\mathrm{R}}$. A direct simulation of the curves $M(B)$ and $\mu(B)$ using one-and-the-same parameter set accurately reproduces the experiment. Moreover, the relation $\Delta M/N = \Delta\mu/B$ as predicted theoretically for the oscillation amplitudes is experimentally confirmed for the investigated samples.

Magnetotransport measurements are performed on InP/InGaAs Hall bar samples in tilted external magnetic fields with tunable out-of-plane angle θ and in-plane angle φ. Beating patterns in the Shubnikov-de-Haas oscillations reveal a φ-anisotropy of the first beat node position. Moreover, the angle of half a coincidence exhibits an anisotropy in φ. These observations are attributed to the presence of both R- and D-SOI terms in combination with an anisotropic $\overline{\overline{g}}^*$-tensor. Fitting the theoretical predictions to the experiment allows to unambiguously determine the strengths as well as the relative sign of the R and D constants. Extracted values of $\alpha_{\mathrm{R}} = 4.61 \times 10^{-11}\,\mathrm{eVm}$ and $\beta_{\mathrm{D}} = 0.47 \times 10^{-11}\,\mathrm{eVm}$ ($\alpha_{\mathrm{R}}/\beta_{\mathrm{D}} > 0$) are close to the ones determined previously from $\mu(B)$. Moreover, the fit revealed the full anisotropy of $\overline{\overline{g}}^*$ with $g_{\parallel} = -4.71$, $g_{\perp} = -2.9$ and $g_{xy} = 0.1$. The method described here thus enables to simultaneously address both SOI terms and $\overline{\overline{g}}^*$-tensor components in 2DESs with high accuracy, thereby providing a more comprehensive picture of spin physics in semiconductor heterostructures.

Finally, the magnetization of laterally etched InP/InGaAs quantum dot ensembles with 460nm diameter is studied by cantilever magnetometry. The measurements show $1/B$-periodic de Haas-van Alphen oscillations that fade out at $B < 2\,\mathrm{T}$ and are substantially reduced in amplitude as compared to reference 2DESs. Theoretical model calculations including ensemble broadening effects reveal that a hard-walled lateral confinement potential is suited best to describe the data. This is attributed to screening effects. Moreover, the modeling clarifies that ensemble broadening is small and the amplitude decrease is dominantly explained by an edge-depletion of $\approx 100\,\mathrm{nm}$ at the lateral borders of the dots. The presented technique thus provides a powerful tool to study the electronic structure of quantum dots containing many electrons. Signatures of spin splitting or SOI were not observed, however, the analysis suggests that an enlargement of the diameter should facilitate the detection of SOI-related beating patterns in $M(B)$ of quantum dots.

Contents

Scientific collaborations

The current work has profited from a scientific collaboration with the groups of Prof. Dr. Thomas Schäpers and Dr. Hilde Hardtdegen from Jülich research center, who provided the InP/InGaAs heterostructures that have been investigated throughout this thesis. Furthermore, Sebastian Heedt from the group of Prof. Schäpers performed the reactive ion etching of the InP/InGaAs quantum dots as investigated in chapter 7. The author would like to express his gratitude for the productive collaboration, the fruitful discussions and for proof-reading of the manuscripts that we submitted for publication.

1 Introduction

Digital information processing has revolutionized nearly every part of our daily and professional lives. This was accompanied by an astonishing progress in the development of microelectronics during the last decades. In traditional semiconductor devices, the underlying chips employ the *charge* of electrons to store, transmit and process information. However, due to the ongoing miniaturization of semiconductor building blocks, conventional charge-based electronics will eventually hit limits. In order to keep up with the demand for faster, smaller, and more energy-efficient devices, physicists started to search for novel functionalities going beyond established device concepts.

A promising approach is to exploit the second fundamental property of an electron apart from its charge, i.e., the electron *spin*. As experimentally demonstrated by Stern and Gerlach [GS22] and theoretically explained by Dirac [Dir28] in the 1920s, electrons can be understood as little magnets with a magnetic moment collinear with their spin. The electron spin itself is a quantum mechanical observable with two distinct states, namely "spin up" and "spin down". This property makes the spin an ideal candidate for information storage via quantum bits (Qubits) or for logical operations.

Attempts to combine spin information with conventional electronics gave rise to the emerging research field of "spintronics" [Wol+01; Gru02]. A cornerstone of the recent spintronics research was the discovery of the giant magnetoresistance (GMR) effect in layered magnetic materials by Fert and Grünberg in 1988/89 [Bai+88; Bin+89]. While enabling a tremendous increase of storage density in today's magnetic hard disks, spintronics applications based on GMR have already reached industrial production level and founded a billion dollar market. For their discovery of GMR, Fert and Grünberg received the Nobel prize in 2007.

Stimulated by the success of spintronics applications in magnetic materials, intensive research is going on to implement spin-related functionality also in semiconductors [AF07]. This would enable combining

logical and storage capabilities of spin with conventional semiconductor electronics in a single multifunctional device. Such devices are predicted to be faster and less energy-consuming and would allow a cost-effective fabrication using established semiconductor process technology. However, precise control of spin as a magnetic property in non-magnetic semiconductors is not straightforward. Moreover, technological challenges such as efficient spin injection and control of relevant spin lifetimes in envisaged devices are subject of intensive research activities.

The key mechanism to address spin electrically is the so-called spin-orbit interaction (SOI). As an electron moves through a semiconductor material (orbital movement) and is exposed to an electric field, special relativity transforms this field into an effective magnetic field in the electron's reference frame. The electron spin then interacts with this magnetic field in form of a precession movement. A prerequisite for SOI to occur in a crystal is a lifting of space inversion symmetry [Win03]. In semiconductors with a zinc-blende lattice, the inherent bulk inversion asymmetry gives rise to the so-called Dresselhaus (D) SOI effect [Dre55]. If the electrons are further confined within a heterostructure to form a two-dimensional electron system (2DES), an artificially tailored structural inversion asymmetry leads to a supplemental SOI contribution known as the Rashba (R) effect [BR84a]. The key aspect here is that the strength of the R effect can be tuned via an external electric field, opening the possibility to manipulate and control the electron spin electronically.

Both D and R mechanisms are subject of intensive research. The R effect was proven to be suitable for spin generation [Koh+12], spin manipulation [DD90; Nit+97; Eng+97; Gru02], and spin detection [Bru+10] in semiconductors. Furthermore, the interplay of both R and D effects can be used for effective spin filtering [SEL03]. Unfortunately, both mechanisms are also responsible for very short spin lifetimes in combination with electron scattering [DP72], which is one of the main problems on the way to semiconductor spintronics devices. Nonetheless, in a recent work it was shown that an elaborate combination of both R and D effects enabled to control and substantially increase spin lifetime [Bal+11].

Device miniaturization via nanopatterning of semiconductor structures leads to an additional confinement of the electron systems to one or even zero dimensions, and also influences the underlying physics

related to SOI effects. Very promising results were published for one-dimensional wires, where the fixed direction of electron movement fixes the direction of the effective magnetic field [Sas+14] and allows for a more precise manipulation of spin via SOI. Moreover, the spin lifetime was reported to be substantially enhanced in etched wire structures [Sch+06; Hol+06; Hol11]. Large spin lifetimes were also predicted for electrons in zero-dimensional confined structures [KN00]. Spin states in such "quantum dots" are considered promising candidates for Qubits in future quantum information processing devices. Still, SOI effects in quantum dots require detailed experimental investigations.

From the above considerations it is clear that a profound understanding of SOI mechanisms in confined electron systems is essential on the way to prospective spintronics applications. One of the main problems remains the accurate determination of the strength of R and D effects, which is crucial for the design of envisaged devices that rely on the interplay of both mechanisms. Therefore, the goal of the present thesis is to investigate SOI effects in InP/InGaAs semiconductor hetero- and nanostructures both experimentally and theoretically.

The thesis is organized as follows: First, a theoretical treatment will be presented in chapter 2 which allows to model the respective magneto-oscillations of a 2DES as a function of an external magnetic field. By calculating field-dependent energy spectra, it will be shown that characteristic beating patterns in these oscillations arise from SOI-induced spin splittings of formerly degenerate Landau levels. Employing a comprehensive theoretical model considering tilted fields and including both R and D terms, the evolution of beat node positions as a function of R and D parameters and tilt angles will be calculated and discussed. Moreover, a treatment of the energy spectra of circularly confined 2DESs in quantum dots will be given.

In chapter 3, proper sample structures and experimental setups of cantilever magnetometry and magnetotransport will be presented. Advancements of the cantilever magnetometer setup that were developed in the course of this thesis will be discussed in chapter 4. In particular, an improvement of the interferometric readout procedure and a novel technique to measure the chemical potential of gated 2DESs via a resonant excitation of micromechanical cantilevers will be introduced.

Simultaneous measurements of beating patterns in the quantum oscillatory magnetization and chemical potential, as facilitated by the

new technique, will be presented in chapter 5. Both quantities are thermodynamic functions of state that provide insights into the system's ground state and directly monitor changes in the Landau level structure as evoked by SOI. By comparing with model calculations it will be shown that both R- and D-SOI contributions are relevant to accurately describe the data. This will go beyond previous investigations of SOI-related beating patterns, where only the R contribution has been considered in the analysis. From the present simulations, it is possible to extract absolute strengths of both R and D terms.

Chapter 6 is dedicated to a new approach enabling the measurement of absolute values and relative sign of the R and D constants from magnetotransport experiments. In particular, it will be shown that the beat node positions perform shifts as a function of the in-plane angle of the external magnetic field, which allows for an unambiguous determination of R and D strengths. In addition, anisotropies in the effective electron $\overline{\overline{g}}^*$-tensor of the present samples will be extracted quantitatively.

Magnetization experiments on nanopatterned InP/InGaAs quantum dot ensembles will be presented in chapter 7. From measured magneto-oscillations and theoretical modeling, the shape of the lateral confinement potential and the amount of edge depletion will be clarified. Signatures of SOI are not observed for the dot ensembles, however, the relevance of SOI in the experiment will be discussed and conclusions will be drawn on future approaches to address SOI in the magnetization of dots. Finally, a summary of the results and a short outlook will be given in chapter 8.

2 Theoretical concepts

This work is dedicated to the electronic properties of unpatterned and nanopatterned two-dimensional electron systems that are formed in InP/InGaAs semiconductor heterostructures. The conduction electrons in these systems are subject to spin-orbit interaction (SOI) effects, which we address experimentally in the magneto-oscillations of, both, thermodynamic quantities and magnetotransport. In this chapter, we provide a fundamental theoretical treatment of the field-dependent energy spectra inherent to 2DES exhibiting SOI. We show how to extract relevant SOI-parameters from the magneto-oscillations and how to model these oscillations in respective thermodynamic quantities. Furthermore, we discuss how the energy spectra and quantum oscillations are altered, if the 2DES is laterally confined in quantum dots. The theoretical treatments presented in this chapter are the basis for analyzing and modeling the experimental data obtained via torque magnetometry and magnetotransport.

2.1 Crystallographic conventions

In order to treat the electronic structure of the relevant 2DESs in detail, we first introduce basic conventions on crystallographic directions. InP and InGaAs condense in the zinc blende structure. The zinc blende lattice consists of two fcc sub-lattices of type-III atoms (Ga, In) and type-V atoms (P, As), respectively, which are shifted by $^1/_4$ of the cubic space diagonal. We define our coordinate system such that one of the type-III atoms is located at the origin and $\hat{\mathbf{x}} \parallel [100]$, $\hat{\mathbf{y}} \parallel [010]$, $\hat{\mathbf{z}} \parallel [001]$. Thus, the lattice of the type-V atoms is shifted by $(^1/_4, ^1/_4, ^1/_4)$ with respect to the origin. A sketch of the so-defined conventional cubic unit cell is depicted in Fig. 2.1 (a). We note that the introduction of the shifted type-V sub-lattice breaks the inversion asymmetry of the crystal. This leads to the inequivalence of certain directions, e.g. [111] and $[\bar{1}\bar{1}\bar{1}]$

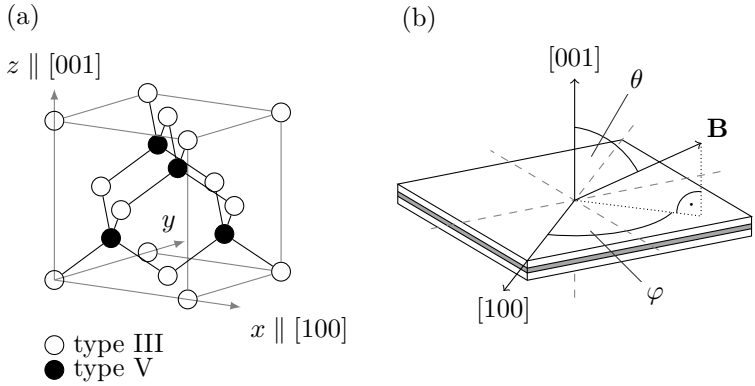

Figure 2.1: (a) Conventional cubic unit cell of the zinc-blende lattice. The fcc-lattice formed by the type-III atoms contains the origin $(0, 0, 0)$ of the defined coordinate system, while lattice of the the type-V atoms is shifted by $(1/4, 1/4, 1/4)$ with respect to the origin. (b) Schematic orientation of an external **B**-field with respect to a (001)-oriented 2D heterostructure as treated in this work. The polar or tilt angle θ is defined as the angle of **B** with the z-axis, while the azimuthal or in-plane angle φ is measured between the projection of **B** into the (x, y)-plane and the x-axis.

or [110] and $[1\bar{1}0]$. Care should be taken if type-III and type-V lattices in Fig. 2.1 (a) are swapped, since in that case relevant crystallographic directions will change sign. This affects the definitions of SOI-related effective fields as introduced in 2.3.2.

The InGaAs/InP heterostructures investigated in this work are grown along the [001]- or $\hat{\mathbf{z}}$-direction, i.e. the 2DES is located in the (x, y)-plane of the coordinate system [Fig. 2.1 (b)]. To address quantum oscillations of the 2DES, we apply a magnetic field **B** with its orientation defined in polar coordinates. Here, the polar or tilt angle θ is measured between **B** and the z-axis, while the azimuthal or in-plane angle φ is defined between the x-axis (or [001]-direction) and the projection of **B** to the (x, y)-plane.

2.2 The two-dimensional electron system

In this section, we discuss the quantum mechanical properties of two-dimensional electron systems formed in semiconductor heterostructures. After introducing the formalism of quasi-2DESs, we derive the energy spectrum of an ideal 2DES subjected to an external magnetic field $\mathbf{B}$ and outline the origin of quantum oscillations. Furthermore, we discuss effects of level broadening and finite temperature that allow for a realistic description of relevant thermodynamic quantities such as the magnetization M and the chemical potential μ.

We start with the dispersion relation of quasi-free conduction electrons in bulk semiconductors:

$$E = E_c + \frac{\hbar^2 \mathbf{k}^2}{2m^*} \tag{2.1}$$

Here, E_c is the energy of the conduction band minimum and m^* is the effective mass that arises due to the interaction of conduction electrons with the lattice-periodic potential of ionic cores [AM76]. In a 2D heterostructure, band discontinuities result in a potential $V(z)$ along the growth direction, enabling the effective confinement of electrons within, e.g., a quantum well (QW). The respective Hamiltonian decomposes into

$$\begin{aligned} H &= H_\perp + H_\parallel \\ &= \left(\frac{\hbar^2 p_z^2}{2m^*} + V(z) \right) + \frac{\hbar^2 (p_x^2 + p_y^2)}{2m^*} \ , \end{aligned} \tag{2.2}$$

where $H_\perp$ describes the movement of the electrons perpendicular to the plane and $H_\parallel$ addresses the parallel motion. Therefore, the wave function can be separated into $\Psi(x, y, z) = \psi(x, y)w(z)$, and the respective eigenenergies are obtained via

$$H_\perp |w(z)\rangle = E_{\perp,m} |w(z)\rangle \tag{2.3}$$

$$H_\parallel |\psi(x, y)\rangle = E_\parallel |\psi(x, y)\rangle \ . \tag{2.4}$$

The energy spectrum hence decomposes into subbands with index m where $w(z)$ is the subband wave function. The total energy can now be written as $E = E_c + E_{\perp,m} + E_\parallel$. If the number of confined electrons is

sufficiently low, only the lowest subband ($m = 0$) is occupied. Omitting the constant $E_c + E_{\perp,0}$, the energy spectrum of the system is solely given by Eq. (2.4), describing a two-dimensional electron system (2DES) in the (x, y)-plane. In the following, we will discuss the spectrum of $H_{\parallel}$ only, keeping in mind that the electron system has a finite thickness in z-direction, given by the subband wave function $w(z)$. This is referred to as a "quasi-2DES" in the literature.

2.2.1 Ideal 2DES in a magnetic field

We now consider the case of an ideal 2DES subject to an external magnetic field $\mathbf{B} = (0, 0, B_{\perp})$ perpendicular to the 2DES plane (i.e. $\theta = 0$) at temperature $T = 0\,\mathrm{K}$. Initially, we will neglect spin-related effects. The problem was first addressed by Landau in 1930 [Lan30]. Because of its fundamental importance to the phenomena discussed in this work, we will recapitulate the derivation of the respective eigenenergies E_n and eigenfunctions $|n\rangle$ in the following. Here, we will employ the algebraic method based on the formalism of ladder operators, which can be found, e.g., in Ref. [Rös09]. Later on, we will show that this formalism is especially suited to address further contributions including SOI. The problem without spin can be formulated via the Hamiltonian

$$H_0 = \frac{\pi_x^2 + \pi_y^2}{2m^*} \tag{2.5}$$

with the kinetic momentum for electrons $\boldsymbol{\pi} = -\mathrm{i}\hbar\nabla + e\mathbf{A}$, the vector potential $\mathbf{A}$ defined by $\mathbf{B} = \nabla \times \mathbf{A}$ and the effective electron mass m^*. The elementary charge e is defined as a positive constant. We now determine the energy eigenvalues E_n of H_0. Therefore, we define the annihilation and creation operators

$$a = \frac{l_B}{\sqrt{2}\hbar}(\mathrm{i}\pi_x + \pi_y) \quad \text{and} \quad a^\dagger = \frac{l_B}{\sqrt{2}\hbar}(-\mathrm{i}\pi_x + \pi_y)\ , \tag{2.6}$$

where a and $a^\dagger$ fulfill the commutation relation $[a, a^\dagger] = 1$. Here, we introduced the magnetic length $l_B = \sqrt{\hbar/(eB_\perp)}$. Using these operators, we can rewrite H_0 in the form

$$H_0 = \hbar\omega_c\left(a^\dagger a + \frac{1}{2}\right) , \tag{2.7}$$

with the cyclotron frequency $\omega_c = (eB_\perp)/m^*$. The Hamiltonian H_0 takes the form of a quantum mechanical harmonic oscillator with the eigenvalues

$$E_n = \hbar\omega_c\left(n + \frac{1}{2}\right), \qquad n = 0, 1, 2, \dots , \tag{2.8}$$

which are also known as Landau levels (LLs) after their theoretical prediction by Landau in 1930 [Lan30]. The corresponding wave functions $|\psi_n(x, y)\rangle$ can be found by solving

$$a|\psi_0(x, y)\rangle = 0 \tag{2.9}$$

and obtaining $|\psi_n(x, y)\rangle$ by applying the creation operator n-times on $\psi_0(x, y)$, i.e.

$$|\psi_n(x, y)\rangle = \frac{(a^\dagger)^n}{\sqrt{n!}}|\psi_0(x, y)\rangle \tag{2.10}$$

However, Eqs. (2.9) and (2.10) still depend on x and y, implying that the LLs are highly degenerate. By using the Landau gauge $\mathbf{A} = (0, xB_\perp, 0)$ and applying the separation ansatz $\psi_0(x, y) = \exp(-\mathrm{i}k_y y)u_0(x)$, we can rewrite Eq. (2.9) in real space coordinates

$$\left(\partial_x + \frac{x - x_0}{l_B^2}\right)u_0(x) = 0 \tag{2.11}$$

with the guiding center coordinate $x_0 = k_y l_B^2$. The solution of Eq. (2.11) takes the form $u_0(x) = \pi^{-1/4} l_B^{-1/2} \exp{(x - x_0)^2/(2l_B^2)}$. The degeneracy of $\psi_0(x, y)$ can be obtained by restricting the geometry of the 2DES to the area $A_\mathrm{m} = L_x L_y$. In this case, the distance between two neighboring guiding centers is given by $\Delta x_0 = \Delta k_y l_B^2 = (2\pi l_B^2)/L_y$. Hence, the

number of allowed k_y is finite and given by $N = L_x/\Delta x_0 = A_\mathrm{m} e B_\perp/h$. The degeneracy of a LL per unit area of the 2DES is thus

$$N_L = \frac{eB_\perp}{h} \cdot g_s \ . \tag{2.12}$$

Here, $g_s = 2$ for a spin-degenerate system. Note that this degeneracy is the same for all LLs n, since those are obtained independently from the N_L ground states $|\psi_0\rangle$ via Eq. (2.10). Since N_L is proportional to $B_\perp$ and a constant electron density n_2D is assumed, the number of LLs which are filled with electrons reduces in a discrete manner if the field is increased. In particular, the Fermi energy E_F jumps from one level to the next lower level at integer values of the filling factor

$$\nu = \frac{n_\mathrm{2D}}{N_L} = \frac{h}{eB_\perp} \cdot n_\mathrm{2D} \ , \tag{2.13}$$

as depicted in Fig. 2.2. These jumps in E_F give rise to quantum oscillations in the magnetization M, the chemical potential μ, the resistivity ρ_{xx} and further quantities which depend on the filling of the LLs. All of those types of oscillations have in common that their frequency in the inverse perpendicular field $1/B_\perp$ is equal to

$$f_{1/B_\perp} = \frac{1}{g_s}\frac{h}{e} \cdot n_\mathrm{2D} \ . \tag{2.14}$$

We note that this relation is based on the fact that the LL degeneracy changes with $B_\perp$ and is independent on the energy spectrum E_n itself. Therefore, Eq. (2.14) holds true for any 2DES, even if the E_n are altered due to perturbations of H_0, e.g., spin-orbit interaction or electron-electron interaction effects. It represents a powerful tool to determine the density of a 2DES.

Note that we neglected contributions introduced by in-plane components of the magnetic field $B_\parallel = (B_x, B_y)$ up to now. Still, tilted fields play an important role in this work. An in-plane field can modify the movement of the electrons perpendicular to the 2DES plane (i.e. the z-direction in our notation). It was shown that in real quantum wells, where the 2DES exhibits a finite thickness, an in-plane field barely affects the oscillatory parts of the quantum oscillations in M and μ, as

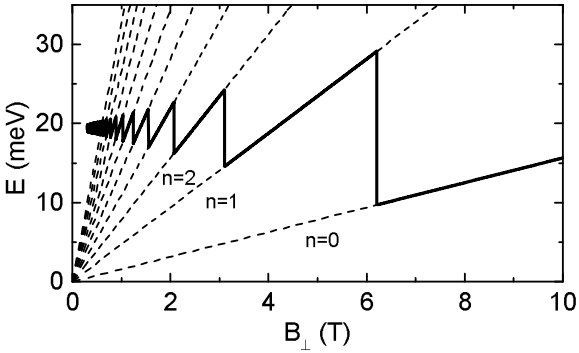

Figure 2.2: Fermi energy of an ideal 2DES as a function of $B_\perp$ for a constant density $n_{2\mathrm{D}}$. The dashed lines represent Landau levels with $E_n = (n+1/2)\hbar\omega_c$.

long as the Landau energy $\hbar\omega_{c,\parallel}$ is smaller than the energy separation of 2D subbands [Wil+09]. This is the case for the 2DESs and values of $B_\parallel$ used in this work. We therefore conclude that the omission of $B_\parallel$ in the orbital terms of the Hamiltonian is justified. However, the $B_\parallel$-components cannot be neglected in the Zeeman term, which will be discussed in detail in section 2.3.1.

2.2.2 Real 2DES: thermodynamic properties

In the following, we briefly outline how to derive fundamental thermodynamic quantities such as the free energy F, the chemical potential μ and the magnetization M from the energy spectrum $E_n(B_\perp)$. Here, we include effects of level broadening and a finite temperature to remodel experimental data. A detailed treatment can be found, e.g., in Refs. [UE09] and [Wil+08].

Following [Wil+08], we derive relevant thermodynamic quantities and relations by starting with the differential of the total free energy F of a 2DES

$$dF = -SdT - \mathbf{M}d\mathbf{B} + \mu dN \ . \tag{2.15}$$

Here, S is the entropy, T is the temperature, μ is the chemical potential and N is the total number of electrons. Using Eq. (2.15), the relations for $\mathbf{M}$ and μ read:

$$\mathbf{M} = -\left(\frac{\partial F}{\partial \mathbf{B}}\right)_{T,N} \qquad \mu = \left(\frac{\partial F}{\partial N}\right)_{T,\mathbf{B}} \tag{2.16}$$

If we are interested in the magnetization caused by the in-plane orbital motion of the electrons only and neglect contributions related to electron movement in z-direction, we find that $\mathbf{M}$ is always perpendicular to the 2DES plane. Therefore, we can replace the vectors $\mathbf{M}$ and $\mathbf{B}$ in Eq. (2.16) by the scalars M and $B_\perp$, respectively. A further differentiation of Eq. (2.16) yields the Maxwell-relation

$$-\left(\frac{\partial M}{\partial N}\right)_T = \left(\frac{\partial \mu}{\partial B_\perp}\right)_T , \tag{2.17}$$

which links both M and μ. Numerical access to the free energy F is gained via the density of states (DOS) of the electrons. For an ideal 2DES with level energies $E_n(B_\perp)$, the DOS per unit area is expressed as

$$D(E, B_\perp) = \frac{eB_\perp}{h} \sum_n \delta(E - E_n(B_\perp)) , \tag{2.18}$$

where the Dirac distribution $\delta(E)$ characterizes the DOS of a single level. However, in a real heterostructure, residual impurities and phonons provoke scattering, thereby leading to a broadening of the levels. Several approaches exist to address this aspect phenomenologically in the calculations [Wil+08; Pot+96]. We note that the exact level shape and the evolution of the broadening with $B_\perp$ is debated. Ando and Uemura, who treated this aspect theoretically, derived an analytical expression featuring Gaussian-broadened levels, with a width Γ that is proportional to $\sqrt{B_\perp}$ [AU74]. This ansatz was shown to describe the level broadening in the present InGaAs/InP-based 2DES quite well [Rup+13; Wil+14], and will thus be used in this work. Assuming Gaussian-broadened levels, the DOS can be written as

$$D(E, B_\perp) = \frac{eB_\perp}{h} \sum_n \frac{1}{\sqrt{2\pi}\Gamma} \exp\left[\frac{(E - E_n(B_\perp))^2}{2\Gamma^2}\right] . \tag{2.19}$$

Now, for a given electron density n_{2D} and assuming $T = 0$, the levels are filled with electrons up to the Fermi energy E_F. In case of a finite temperature, E_F is replaced by the chemical potential μ. Applying Fermi-Dirac statistics, we find

$$n_{2D} = \int_{-\infty}^{\infty} D(E, B_\perp) \, \frac{1}{1 + \exp \frac{E-\mu}{k_B T}} \, dE \tag{2.20}$$

where k_B is the Boltzmann constant and $n_{2D} = N/A_m$ (A_m is the total 2DES area). The chemical potential is obtained numerically by solving Eq. (2.20) for μ. Finally, μ is used to derive the free energy F of the 2DES via [UE09]

$$F(B_\perp) = \mu N - k_B T A_m \int_{-\infty}^{\infty} D(E, B_\perp) \ln \left[1 + \exp \frac{\mu(B_\perp) - E}{k_B T} \right] dE \; . \tag{2.21}$$

Using (2.21), the magnetization is calculated via $M = -\partial F / \partial B_\perp$ [c.f. Eq. (2.16)].

In Fig. 2.3, we show plots of $\mu(B_\perp)$ and $M(B_\perp)$ of a spin-degenerate 2DES subjected to a level broadening $\Gamma = 0.8\,\mathrm{meV}/\sqrt{\mathrm{T}}$ at different temperatures T (the case of $T = 0$ and $\Gamma = 0$ is also shown for comparison). Both μ and M exhibit sawtooth-like oscillations with the steep flanks corresponding to even integer filling factors ν, which smear out for increasing Γ and T. The smearing with temperature is more pronounced at smaller $B_\perp$, because the Landau gap $\hbar\omega_c$ decreases relatively to the thermal energy $k_B T$ as $B_\perp$ decreases. This explains the need for very low temperatures to address oscillations at large filling factors, i.e., small $B_\perp$. The oscillations in M are also referred to as de Haas-van Alphen (dHvA)-oscillations after their discovery by de Haas and van Alphen in bulk bismuth in 1930 [HA30]. The quasi-discontinuous jumps $\Delta\mu$ and ΔM (Fig. 2.3) are directly related via the Maxwell relation $(\partial M/\partial \mu)_{B,T} = (\partial N/\partial B)_{M,T}$. In a single particle picture and given that disorder and temperature related broadening effects are small, it was predicted that these jumps obey the relation [Wie+97]

$$\frac{\Delta M}{N} = \frac{\Delta \mu}{B_\perp} \; . \tag{2.22}$$

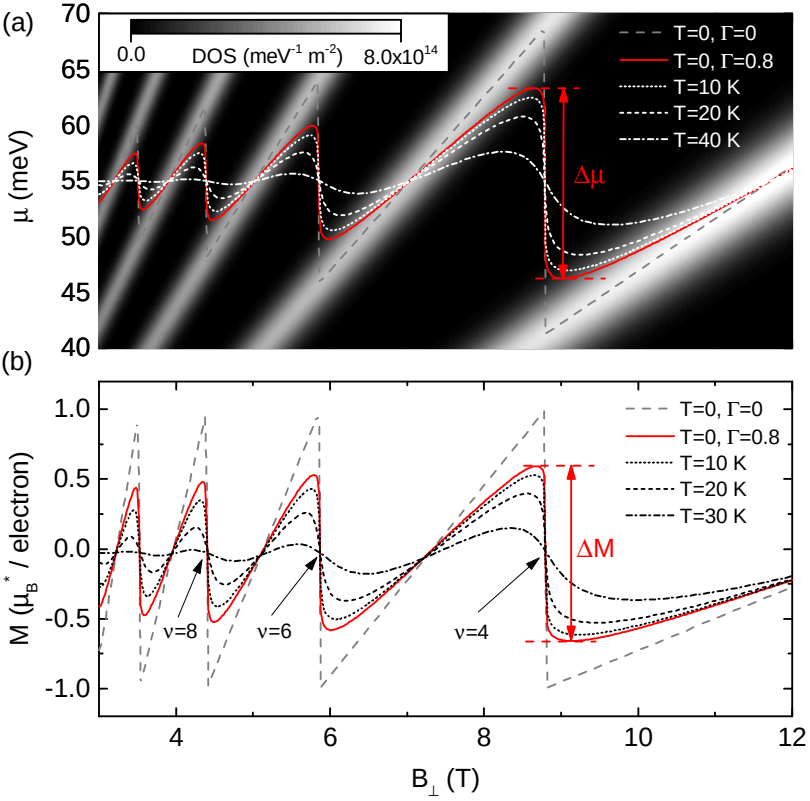

Figure 2.3: (a) Chemical potential $\mu(B_\perp)$ of a 2DES subject to a level broadening of $\Gamma = 0.8\,\mathrm{meV}/\sqrt{\mathrm{T}}$ at different temperatures T. In the background, the DOS of the broadened Landau levels is illustrated as a grayscale plot. The dashed curve in gray represents μ of an ideal 2DES at $T = 0\,\mathrm{K}$. (b) Corresponding magnetization $M(B_\perp)$ in units of the effective Bohr magneton $\mu_\mathrm{B}^* = (e\hbar)(2m^*)$ using the same parameters as in (a). The steep flanks corresponding to $\nu = \{4, 6, 8\}$ are indicated by arrows. The amplitudes $\Delta\mu$ and ΔM corresponding to $\nu = 4$ are indicated in both curves. For the calculations we used $n_\mathrm{2D} = 8.5 \times 10^{11}\,\mathrm{cm}^{-2}$ and $m^* = 0.037 m_0$.

The temperature-dependence of ΔM is approximately given by the Lifshitz-Kosevich (LK) formalism [Sho84], which yields

$$\Delta M = \Delta M_0 \frac{X}{\sinh X} \quad \text{with} \quad X = \frac{2\pi^2 k_B T}{\hbar \omega_c} \,, \tag{2.23}$$

where ΔM_0 denotes the dHvA amplitude at zero temperature. Equation (2.23) was derived for 3D electron systems in the limit of large quantum numbers and assuming $\mu = const.$, i.e., in a regime where the dHvA-oscillations are nearly sinusoidal. However, it was demonstrated that (2.23) provides a good approximation also for sawtooth-shaped dHvA-oscillations of 2DESs [Wil+08], thereby providing a tool to measure the energy gap $\hbar\omega_c$ and thus the effective mass m^* of the 2DES independent of the effect of disorder broadening.

2.3 Spin splitting in a 2DES

Spin degeneracy is a result of both space- and time inversion symmetry [Win03]. Inversion in space changes the wave vector **k** to -**k** but leaves the direction of the spin σ untouched, which gives

$$E(\mathbf{k})_+ = E(-\mathbf{k})_+. \tag{2.24}$$

Time reversal changes the direction of **k** and flips the spin and we find

$$E(\mathbf{k})_+ = E(-\mathbf{k})_- \,, \tag{2.25}$$

which is also called Kramers degeneracy. If we combine both equations, we obtain a twofold degeneracy of the energies

$$E(\mathbf{k})_+ = E(\mathbf{k})_- \,. \tag{2.26}$$

If one or both of these symmetries are broken, the degeneracy is lifted. In this case, we define the spin splitting $\Delta_s = E(\mathbf{k})_+ - E(\mathbf{k})_-$. This splitting can be caused by an external magnetic field **B**, which breaks time inversion symmetry, and is referred to as Zeeman splitting. Consequently, the LLs introduced in section 2.2.1 are spin-split because of the presence of the external magnetic field, but the Zeeman splitting

is sometimes neglected in the literature when it is small compared to $\hbar\omega_c$. Furthermore, spin splitting is also obtained at zero magnetic field if the space inversion symmetry is broken. This is the case in crystal structures where the periodic potential lacks a center of inversion (e.g. the zinc-blende lattice), which is known as bulk inversion asymmetry (BIA). Furthermore, the QW containing the 2DES can be asymmetric in the growth direction due to asymmetric modulation doping, differing band discontinuities at the QW edges or externally applied gate voltages. This "artificial" type of asymmetry is referred to as structural inversion asymmetry (SIA). In the general case, spin splitting can be understood as the interaction of the electron spin with an effective magnetic field $\mathbf{B}_{\text{eff}}$, which is a superposition of all contributions of the different spin splitting mechanisms. The Hamiltonian is extended by the term

$$H_{\text{s}} = \frac{1}{2} g^* \mu_{\text{B}} \, \boldsymbol{\sigma} \cdot \mathbf{B}_{\text{eff}} \, , \tag{2.27}$$

where $\boldsymbol{\sigma} = (\sigma_x, \sigma_y, \sigma_z)$ is the vector of the spin Pauli matrices which we define in the crystal basis (x, y, z), g^* is the effective electron Landé factor and μ_{B} is the Bohr magneton. Note that in absence of an external magnetic field, $\mathbf{B}_{\text{eff}} = \mathbf{B}(\mathbf{k})$ is a result of the interaction of electron spin with the orbital movement of the electron (spin-orbit interaction) and depends on the wave vector $\mathbf{k}$. In the following, we will discuss different contributions to spin splitting which occur in the 2DES within the InP/InGaAs heterostructures investigated in this work.

2.3.1 Zeeman splitting

Isotropic Zeeman splitting

The splitting due to the external applied field $\mathbf{B}$ is called Zeeman splitting and the respective Hamiltonian reads

$$H_{\text{Z}} = \frac{1}{2} g^* \mu_{\text{B}} \boldsymbol{\sigma} \cdot \mathbf{B} \, . \tag{2.28}$$

As a result, every LL with energy E_n splits up into two distinct sub-levels (Fig. 2.4)

$$E_{n,\pm} = E_n \pm \frac{1}{2} g^* \mu_{\text{B}} B \tag{2.29}$$

with a degeneracy per unit area of $N_L = eB_\perp/h$ [c.f. Eq. (2.12)]. We note that the Zeeman splitting $\Delta_{s,\mathrm{Z}} = g^*\mu_\mathrm{B}B$ depends on the *total* amplitude of the magnetic field $\mathbf{B}$ whereas the LL separation $\hbar\omega_c = \hbar eB_\perp/m^*$ depends on the perpendicular component $B_\perp = B\cos\theta$ only. Consequently, the ratio of $\Delta_{s,\mathrm{Z}}/(\hbar\omega_c)$ can be tuned by adjusting the tilt angle θ. Special values of this ratio of $(1/2, 1, 3/2, \ldots)$ define the so-called coincidence angles

$$\cos\theta_c^i = \frac{1}{i}\cdot\frac{g^*\mu_\mathrm{B}m^*}{e\hbar} \quad \text{with} \quad i = 1/2, 1, 3/2, \ldots . \tag{2.30}$$

If $i \in \{1/2, 3/2, 5/2, \ldots\}$, subsequent levels in the energy spectrum are equally spaced [half coincidence, Fig. 2.4 (b)] whereas integer numbers of i denote the case where a degeneracy of the levels occurs, and the gap at every second filling factor vanishes [full coincidence, Fig. 2.4 (c)]. Hence, the measurement of coincidence angles provides a tool to determine the effective g^* factor of the 2DES.

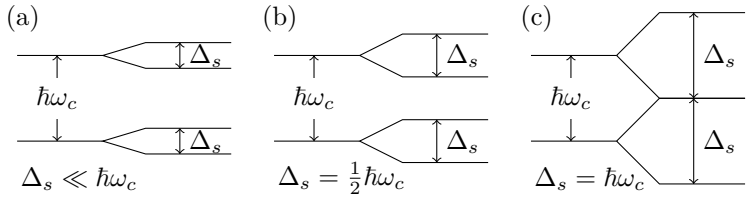

Figure 2.4: Schematic energy diagram of LLs for different splitting energies Δ_s. (a) Case of small spin splitting. (b) Half coincidence: all energy levels are equally spaced. (c) Full coincidence: neighboring LLs with opposite spin orientations are degenerate.

Anisotropic Zeeman splitting

In the previous section, the Zeeman splitting with an isotropic effective g^*-factor was discussed, which resulted in a spin splitting $\Delta_{s,\mathrm{Z}} = g^*\mu_\mathrm{B}B$ independent of the direction of $\mathbf{B}$. Corrections to the g^*-factor of free electrons in semiconductors originate from the coupling of the electron spin with the angular momentum of the lattice-periodic parts of the

orbital Bloch wave functions (similar to the derivation of the Landé g-factor in atoms) [RLZ59]. If the symmetry with respect to the 3D bulk material is reduced, the effective g^*-factor is no longer isotropic and needs to be replaced by an effective $\overline{\overline{g}}^*$-tensor. In the general case, the Zeeman term in the Hamiltonian is

$$H_{\mathrm{Z}} = \frac{1}{2}\mu_{\mathrm{B}} \sum_{i,j} g_{ij}\sigma_i B_j \ , \tag{2.31}$$

where g_{ij} are the components of $\overline{\overline{g}}^*$ and are obtained within the framework of $\mathbf{k}\cdot\mathbf{p}$ theory [Win03]. In quasi-2D systems, the reduction of symmetry gives rise to an out-of-plane anisotropy of $\overline{\overline{g}}^*$ into components $g_\perp$ for perpendicular and $g_\parallel$ for in-plane field direction [IK92; PZ06]. This is due to the $\mathbf{k}\cdot\mathbf{p}$ coupling to different subbands for $g_\perp$ and $g_\parallel$, respectively. The correct way of addressing this anisotropy theoretically is debated [PZ06]. Furthermore, $\mathbf{k}\cdot\mathbf{p}$-theory also predicts an in-plane anisotropy of $\overline{\overline{g}}^*$ in inversion-asymmetric systems if the QW is asymmetric in the growth direction, e.g., via a built-in electric field $\mathcal{E}$ as first discussed by Kalevich and Korenev [KK93]. In zinc-blende structures grown along the [001]-direction, this gives rise to an additional component g_{xy}, which is proportional to the Dresselhaus parameter γ (see 2.3.2) and depends on the exact form of the electron subband wave function. A quantitative derivation of the components of $\overline{\overline{g}}^*$ from theory is challenging, because exact microscopic details of a particular heterostructure are usually unknown. It is thus useful to determine these components experimentally. The $\overline{\overline{g}}^*$-tensor for a [001]-oriented QW now takes the form

$$\overline{\overline{g}}^* = \begin{pmatrix} g_\parallel & g_{xy} & 0 \\ g_{xy} & g_\parallel & 0 \\ 0 & 0 & g_\perp \end{pmatrix} . \tag{2.32}$$

Note that $\overline{\overline{g}}^*$ is diagonal in a basis with $x \parallel [110]$ and $y \parallel [1\bar{1}0]$, which reflects the symmetry of the zinc-blende crystal. Furthermore, the sign of g_{xy} depends on the direction of $\mathcal{E}$ for symmetry reasons. A diagonalization of (2.31) reveals that the energy spectrum $E_{n,\pm}$ can be

expressed with a scalar g^* as in (2.28), where g^* depends on the polar and azimuthal angles θ and φ (see Appendix B.3):

$$g^*(\theta,\varphi) = \sqrt{g_\perp^2 \cos^2\theta + (g_\parallel^2 + g_{xy}^2)\sin^2\theta + 2g_\parallel g_{xy}\sin^2\theta \sin 2\varphi}\ . \tag{2.33}$$

Neglecting the in-plane anisotropy g_{xy}, the out-of-plane anisotropy of g^* reads

$$g^*(\theta) = \sqrt{g_\perp^2 \cos^2\theta + g_\parallel^2 \sin^2\theta}\ . \tag{2.34}$$

On the other hand, if we address in-plane components of $\overline{\overline{g}}^*$ with a field $\mathbf{B}$ parallel to the 2DES plane ($\theta = 90°$) and assume $g_{xy} \ll g_\parallel$, Eq. (2.33) simplifies to

$$g^*(\varphi) = g_\parallel + g_{xy}\sin 2\varphi\ . \tag{2.35}$$

The components of $\overline{\overline{g}}^*$ can therefore be addressed independently by varying the angles θ and φ, respectively. As an additional remark, we state that the straightforward diagonalization (2.33) to obtain a scalar $g^*(\theta,\varphi)$ is *not* possible if the total Hamiltonian H contains additional terms that depend on the spin operator $\boldsymbol{\sigma}$, as will be discussed in detail in section 2.4.

2.3.2 Zero-field spin splitting

The lack of a center of inversion in bulk zinc-blende crystals lifts the space inversion symmetry. It was first shown by Dresselhaus [Dre55] that this so-called bulk inversion asymmetry (BIA) yields $\mathbf{B}_{\text{eff}}$ for conduction electrons of the form

$$\frac{1}{2}g^*\mu_{\text{B}}\mathbf{B}_{\text{eff}}(\mathbf{k})_{\text{BIA,3D}} = \gamma \begin{pmatrix} k_x(k_y^2 - k_z^2) \\ k_y(k_z^2 - k_x^2) \\ k_z(k_x^2 - k_y^2) \end{pmatrix} \tag{2.36}$$

with the bulk Dresselhaus parameter γ that can be obtained by $\mathbf{k}\cdot\mathbf{p}$-theory and depends mainly on the fundamental energy gaps between the conduction band and neighboring bands at $\mathbf{k} = \mathbf{0}$ [Win03]. However, in quasi 2D systems confined in a QW in z-direction, we can replace the wave vectors for a given subband k_z and k_z^2 by their (constant)

expectation values $\langle k_z \rangle = 0$ and $\langle k_z^2 \rangle \approx (\pi/L_z)^2$. Here, L_z is the width of the QW . We obtain

$$\frac{1}{2} g^* \mu_\mathrm{B} \mathbf{B}_\mathrm{eff}(\mathbf{k})_\mathrm{BIA,2D} = \gamma \langle k_z^2 \rangle \begin{pmatrix} -k_x \\ k_y \\ 0 \end{pmatrix} + \gamma \begin{pmatrix} k_x k_y^2 \\ -k_y k_x^2 \\ 0 \end{pmatrix} , \tag{2.37}$$

where the first term is linear in the wave vector $k_\parallel = (k_x, k_y)$ and the second term is cubic in $k_\parallel$. The cubic term is often neglected in narrow QWs, where $\langle k_z^2 \rangle$ is typically much larger than the in-plane Fermi wave vector $k_{\parallel,F}$. We define the coefficient $\beta_\mathrm{D} := -\gamma \langle k_z^2 \rangle$, which describes the strength of the k-linear Dresselhaus (D) term in a quasi-2DES. Note that β_D not only depends on bulk material parameters, but is also sensitive to the geometry of the heterostructure itself. It is thus difficult to obtain β_D by theoretical considerations because the exact band edge profile in growth direction is usually unknown. For this reason, β_D has to be determined experimentally.

Furthermore, structural inversion asymmetry (SIA) due to a built-in effective electric field $\mathcal{E}$ perpendicular to the QW plane leads to an additional contribution to spin splitting. Bychkov and Rashba first considered this effect which gives rise to the term [BR84b; BR84a]

$$\frac{1}{2} g^* \mu_\mathrm{B} \mathbf{B}_\mathrm{eff}(\mathbf{k})_\mathrm{SIA} = \alpha_\mathrm{R} \begin{pmatrix} k_y \\ -k_x \\ 0 \end{pmatrix} . \tag{2.38}$$

In a QW, the Rashba (R) parameter $\alpha_\mathrm{R} = \langle r_{41}^{6c6c} \mathcal{E} \rangle$ is obtained as the expectation value of a parameter r_{41}^{6c6c} times the effective electric field $\mathcal{E}$ for a given subband wave function, where r_{41}^{6c6c} is again obtained using $\mathbf{k} \cdot \mathbf{p}$-theory [Win03]. We note that α_R can be tuned by external gate voltages [Nit+97; Eng+97; Gru00], enabling the manipulation of spin by electric means. Like the Dresselhaus parameter β_D, the Rashba parameter α_R depends on microscopic details of the heterostructure as well as on material properties and needs to be determined experimentally. The measurement of β_D and α_R is one of the key aspects of this thesis.

In the following treatment, we will restrict ourselves to the the k-linear terms in the Hamiltonian. The influence of the k-cubic Dresselhaus

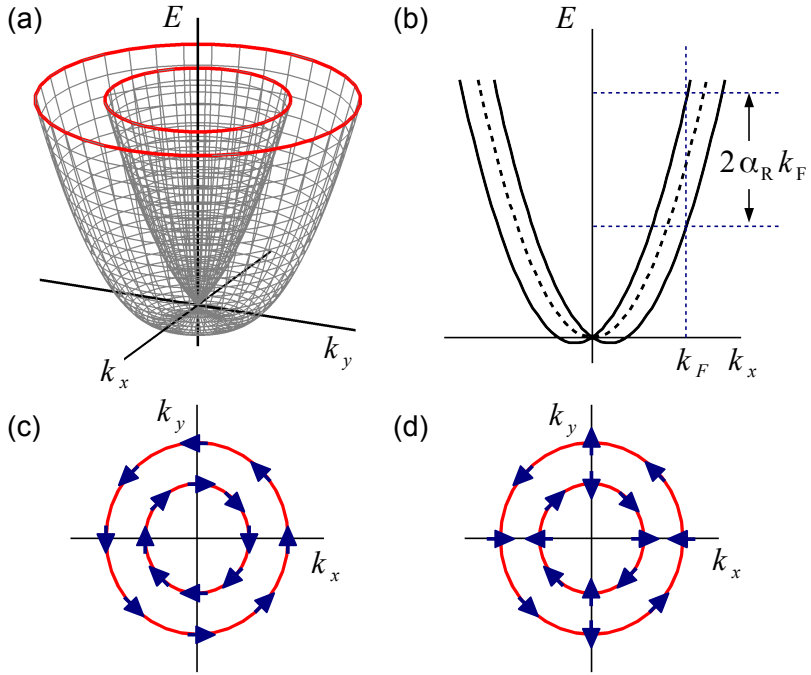

Figure 2.5: Dispersion relation (a) $E_{\pm}(k_{\parallel})$ and (b) $E_{\pm}(k_x)$ at $\mathbf{B} = 0$ and including Rashba-SOI. The zero-field spin splitting at the Fermi level $\Delta_0 = 2\alpha_{\mathrm{R}} k_{\mathrm{F}}$ is indicated in (b). (c) and (d) show cross-sections of $E_{\pm}(k_{\parallel})$ at E_{F} in case of pure Rashba and Dresselhaus SOI, respectively. The respective spin orientations (arrows) are marked for different directions of $k_{\parallel}$.

term is discussed in 2.4.4. Combining Eqs. (2.27), (2.37) and (2.38), the linear R- and D-contributions are

$$\begin{aligned} H_{\mathrm{D}} &= \frac{\beta_{\mathrm{D}}}{\hbar}(\sigma_x \pi_x - \sigma_y \pi_y) \\ H_{\mathrm{R}} &= \frac{\alpha_{\mathrm{R}}}{\hbar}(\sigma_x \pi_y - \sigma_y \pi_x)\,. \end{aligned} \tag{2.39}$$

Here, we replaced the wave vector by the in-plane kinetic momentum operator $\boldsymbol{\pi} = \hbar\mathbf{k}$. We now consider the case at zero magnetic field

if only one of the two contributions is present. A diagonalization of the problem yields the dispersion relation in presence of Rashba-SOI [BR84a]

$$E_{\pm}(\mathbf{k}) = \frac{\hbar^2 k_{\parallel}^2}{2m^*} \pm \alpha_{\mathrm{R}} |k_{\parallel}| \; . \tag{2.40}$$

If plotted in $k_{\parallel}$-space, (2.40) consists of two branches as depicted in Fig. 2.5 (a). The spin splitting Δ_s is not constant, but increases linearly with wave vector k. The zero field spin splitting $\Delta_0 = 2\alpha_{\mathrm{R}} k_{\mathrm{F}}$ is defined as the splitting present at the Fermi wave vector k_{F}, and depends on the electron density via $k_{\mathrm{F}} = \sqrt{2\pi n_{2\mathrm{D}}}$ [Fig. 2.5 (b)]. If only D-SOI is taken into account, α_{R} in Eq. (2.40) is replaced by β_{D}, and the qualitative shape of $E_{\pm}(k_{\parallel})$ remains the same. However, the spin orientations with respect to $k_{\parallel}$ are different for both cases, which can be seen from Eqs. (2.37) and (2.38), due to different $\mathbf{B}_{\mathrm{eff}}$, which defines the relevant spin quantization axes. The relevant spin orientations considering R- and D-SOI are depicted in Fig. 2.5 (c) and (d), respectively.

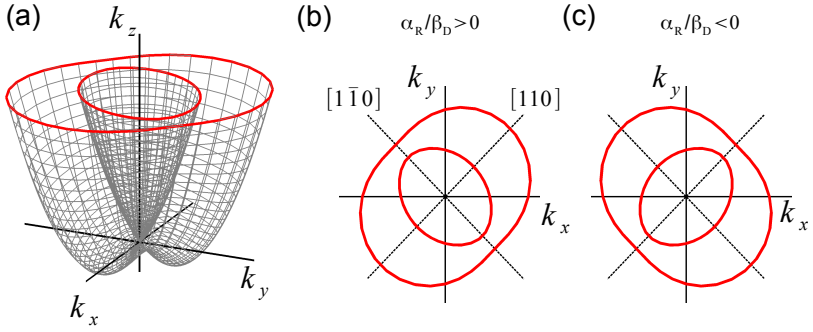

Figure 2.6: Dispersion relation $E_{\pm}(k_{\parallel})$ including both R and D terms. (b) and (c) show cross-sections at the Fermi level for different relative sign of the SOI parameters α_{R} and β_{D}.

As a consequence of the different symmetries of H_{R} and H_{D}, the dispersion relation is altered if both R- and D-interactions are considered,

because the spins couple differently to the respective terms in the Hamiltonian. The dispersion relation reads [And92]

$$E_{\pm}(k_{\parallel}) = \frac{\hbar^2 k_{\parallel}^2}{2m^*} \pm k_{\parallel}\sqrt{\alpha_{\mathrm{R}}^2 + \beta_{\mathrm{D}}^2 + 2\alpha_{\mathrm{R}}\beta_{\mathrm{D}}\sin 2\varphi}\ . \tag{2.41}$$

The splitting is now *anisotropic* in the (k_x, k_y)-plane with principal axes along the [110] and [1$\bar{1}$0] directions [Fig. 2.6 (a)]. The definition of a constant zero field spin splitting Δ_0 at the Fermi wave vector is no longer valid, because Δ_0 now depends on the in-plane angle φ. The orientation of the branches with respect to the principal axes is inverted if the relative sign of α_{R} and β_{D} is changed [Fig. 2.6 (b) and (c)]. An experimental determination of α_{R} and β_{D} and their relative ratio and sign is hence possible if one probes the in-plane anisotropy of the spin splitting. In the next section, we will show that signatures of this anisotropy can be addressed in the quantum oscillations introduced in 2.2.1 if tilted magnetic fields are applied and the in-plane angle φ is varied.

2.4 Spin splitting of Landau levels including spin-orbit interaction

In this section we will show how the energies of the Landau levels defined in section 2.2.1 are altered if SOI and Zeeman splitting are present, and how this will affect the magneto-oscillations which we will use as an experimental probe in this work. The Hamiltonian H including

tilted magnetic fields as well as an anisotropic $\overline{\overline{g}}^*$ tensor is formulated as follows:

$$
\begin{aligned}
H &= H_0 + H_\mathrm{s} = H_0 + H_\mathrm{Z} + H_\mathrm{R} + H_\mathrm{D} \\
H_0 &= \frac{\boldsymbol{\pi}^2}{2m^*} \\
H_\mathrm{Z} &= \frac{1}{2}\mu_\mathrm{B}\left[g_\perp \sigma_z B_\perp + g_\parallel(\sigma_x B_x + \sigma_y B_y) + g_{xy}(\sigma_x B_y + \sigma_y B_x)\right] \\
H_\mathrm{R} &= \frac{\alpha_\mathrm{R}}{\hbar}(\sigma_x \pi_y - \sigma_y \pi_x) \\
H_\mathrm{D} &= \frac{\beta_\mathrm{D}}{\hbar}(\sigma_x \pi_x - \sigma_y \pi_y)
\end{aligned}
$$

The Hamiltonian for free electrons in a magnetic field H_0 is extended by the spin splitting term H_s, which consists of the Zeeman term H_Z as well as the Rashba- and Dresselhaus terms H_R and H_D, respectively. Following Ref. [DDR90], we calculate the matrix elements $H_{ms_z,ns_z'} = \langle m, s_z|H|n, s_z'\rangle$ in terms of the eigenstates $|n, s_z\rangle$ of H_0 ($n = 0, 1, 2, .., s_z = \pm$). The only non-vanishing matrix elements (plus their Hermitian conjugates) are given by

$$
\begin{aligned}
\langle n, \pm|H|n, \pm\rangle &= \left(n + \frac{1}{2}\hbar\omega_c\right) \pm \frac{1}{2}\mu_\mathrm{B} g_\perp B_\perp \\
\langle n, -|H|n, +\rangle &= \frac{1}{2}\mu_\mathrm{B}\left[B_x(g_\parallel + \mathrm{i}g_{xy}) + B_y(g_{xy} + \mathrm{i}g_\parallel)\right] \\
\langle n, +|H|n+1, -\rangle &= \alpha_\mathrm{R}\sqrt{\frac{2e}{\hbar}}\sqrt{(n+1)B_\perp} \\
\langle n, -|H|n+1, +\rangle &= -\mathrm{i}\beta_\mathrm{D}\sqrt{\frac{2e}{\hbar}}\sqrt{(n+1)B_\perp}
\end{aligned}
\tag{2.42}
$$

For the benefit of the reader, the derivation of these matrix elements is carried out in detail in appendix B.1. It is instructive to display H in matrix form, as it is done in Fig. 2.7. The diagonal elements of H represent the energies of the unperturbed LLs including Zeeman splitting due to a perpendicular field. Tilted fields lead to off-diagonal Zeeman terms $Z_\parallel$ which couple states with the same LL index n but different spin orientation. This leads to an enhancement of Zeeman splitting if the tilt angle θ is increased. Both Landau and Zeeman elements depend

linearly on the magnetic field B. The R and D terms cause off-diagonal matrix elements which couple states with neighboring n and different spin orientations. If we are interested only in the energy levels close to the Fermi level E_F (which dominate the magneto-oscillations that we observe in the experiment), we can simplify the R-elements using the approximation $E_\mathrm{F} \approx n\hbar\omega_c$ and $n+1 \approx n$ if n is sufficiently large [DDR90]:

$$\alpha_\mathrm{R}\sqrt{\frac{2eB_\perp(n+1)}{\hbar}} \approx \alpha_\mathrm{R}\sqrt{\frac{2m^*E_\mathrm{F}}{\hbar^2}} = \alpha_\mathrm{R}k_\mathrm{F} \tag{2.43}$$

Equivalently, we obtain $\mp i\beta_\mathrm{D}k_\mathrm{F}$ for the D-elements. In this approximation, the SOI-related off-diagonal terms appear as *constants* in the matrix form of H and thus become more important if the magnetic field B becomes small. An analytic diagonalization of H is only possible if H decomposes into a block-diagonal form, i.e., if only one of the three off-diagonal elements is present. In order to obtain the eigenvalues $E_{n'}(B)$ in the general case, we follow Ref. [DDR90] and diagonalize H numerically by truncating H up to a finite n_max. Therefore, we choose n_max high enough such that the Fermi level E_F is always several levels below n_max within the field range of interest.

In the following, we will discuss the impact of the different off-diagonal terms on the energy spectrum $E_{n'}(B_\perp)$ and show how this influences the magnetic quantum oscillations. For particular examples and illustrations, we will use the basic parameters $m^* = 0.037$, $g^* = -4.63$ (isotropic) and $n_\mathrm{2D} = 8.5 \times 10^{11}\mathrm{cm}^{-2}$, which are already close to those experimentally observed in the 2DESs in InP/InGaAs QWs.

2.4.1 Rashba splitting in a perpendicular field

Let us first consider the simple case of perpendicular field orientation and isotropic g^*-factor if only R-interaction is present. The Hamiltonian

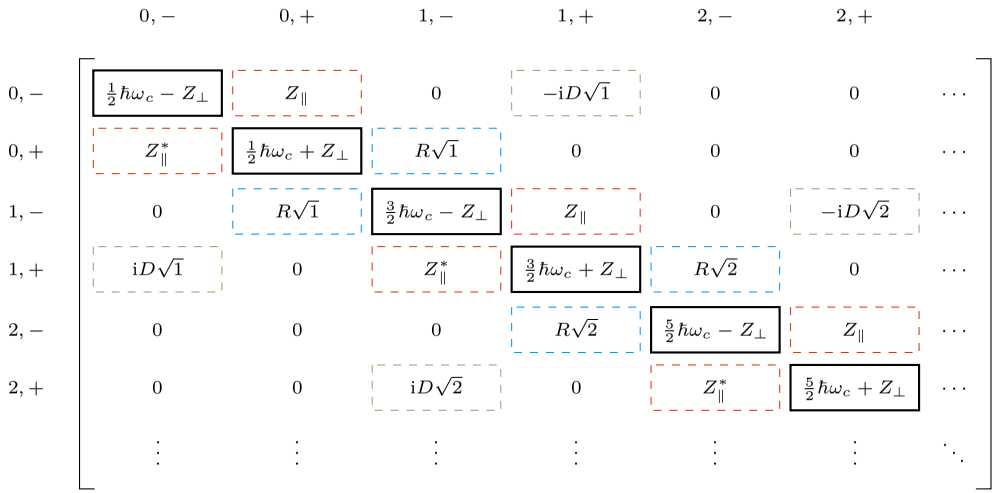

Figure 2.7: Hamiltonian of the problem in matrix notation. Here, $Z_\parallel = {}^1\!/_2\mu_B\big[B_x(g_\parallel + \mathrm{i}g_{xy}) + B_y(g_{xy} + \mathrm{i}g_\parallel)\big]$, $Z_\perp = \frac{1}{2}\mu_B g_\perp B_\perp$, $R = \alpha_\mathrm{R}\sqrt{(2eB_\perp)/\hbar}$ and $D = \beta_\mathrm{D}\sqrt{(2eB_\perp)/\hbar}$. Off-diagonal Zeeman, R- and D- elements are marked by dashed boxes in red, blue and green color, respectively.

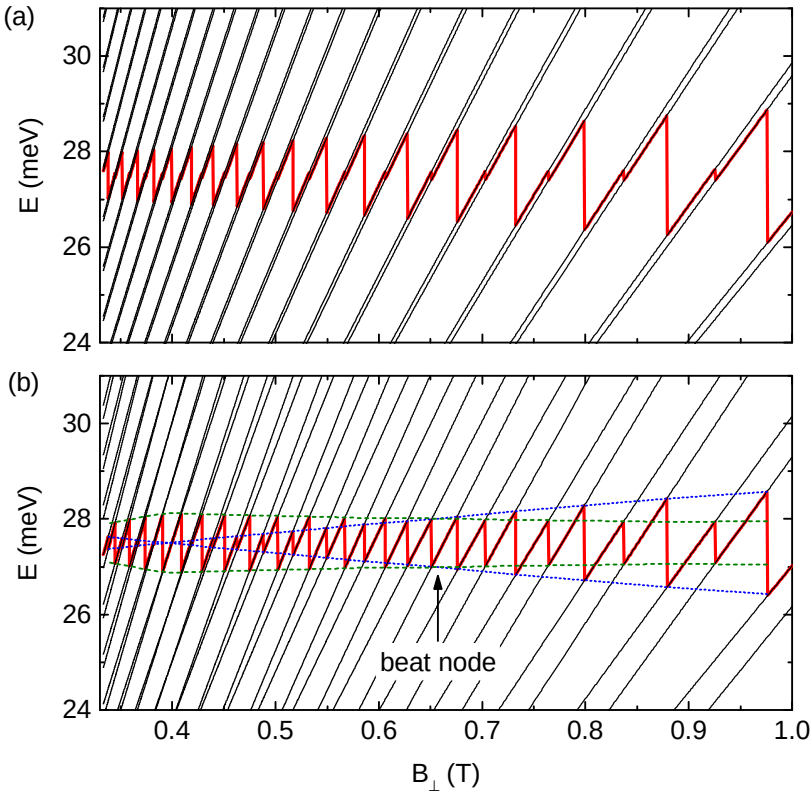

Figure 2.8: Energy spectra $E_{n'}(B_\perp)$ of LLs in a perpendicular field including (a) a small Zeeman term and (b) both Zeeman and Rashba terms (schematic). The Fermi level E_F is depicted in red in both plots. Envelopes of the jumps at even (dashed green curve) and odd (dotted blue curve) filling factors are illustrated in (b). A beat node position is indicated by an arrow.

H now takes a block-diagonal form, allowing for an exact diagonalization [BR84a]. The energy spectrum yields

$$\begin{aligned} E_{n'} =& E_{n,\pm} \\ =& \hbar\omega_c(n + 1/2 \pm 1/2) \\ & \mp \sqrt{(\hbar\omega_c - g^*\mu_B B_\perp)^2 + 8\alpha_R^2 \frac{eB_\perp}{\hbar}(n + 1/2 \pm 1/2)} \end{aligned} \tag{2.44}$$

Figure 2.8 (a) and (b) displays the spectra $E_{n'}(B_\perp)$ for pure Zeeman splitting and for Zeeman plus Rashba splitting, respectively. While in the former case the ratio of Landau and spin splitting gap $(\Delta_s)/(\hbar\omega_c)$ remains constant, the presence of the R-term causes a field-dependent enhancement of $(\Delta_s)/(\hbar\omega_c)$, which becomes more important as the field $B_\perp$ is *decreased*. Hence, the $E_{n'}(B_\perp)$ cross at field values where $(\Delta_s)/(\hbar\omega_c)$ becomes an integer number, which can be understood as SOI-induced level coincidences [c.f. Fig. 2.4 (c)]. Depending on the parity of this number, i.e., even or odd, the energy gap of even or odd filling factors ν vanishes while the opposite gap becomes a maximum. As a consequence, the discrete jumps in the Fermi energy E_F at even and odd integer filling factors perform diametrically opposed beatings as a function of $B_\perp$. This behavior is illustrated by the envelopes of the jumps at even and odd ν in Fig. 2.8 (b). We note that such beatings are present in all kinds of magneto-oscillations, whether they appear in M, μ or ρ_{xx}. We now define a *beat node position* as a field value where subsequent levels in the vicinity of E_F are equally spaced, as marked by an arrow in Fig. 2.8 (b). At these points, the amplitudes of the magneto-oscillations are minimum and eventually go to zero due to level broadening or finite temperature effects. These node positions are key to quantitatively determine the parameter α_R (and also β_D, as we will see later) from the measurements.

Let us now examine the splitting Δ_s in Eq. (2.44) in more detail. In the limit of large magnetic fields, the R-term in the square root of Eq. (2.44) can be neglected and the pure Zeeman splitting $\Delta_{s,Z} = g^*\mu_B B_\perp$ is recovered. On the other hand, if $B_\perp \to 0$ and using the approximation $(2eB_\perp n)/\hbar \approx k_F^2$ [c.f. Eq. (2.43)], we reproduce the zero field spin splitting of $\Delta_0 = 2\alpha_R k_F$. We now numerically calculate the splitting Δ_s as a function of $B_\perp$. Therefore, we start at large $B_\perp$ with two

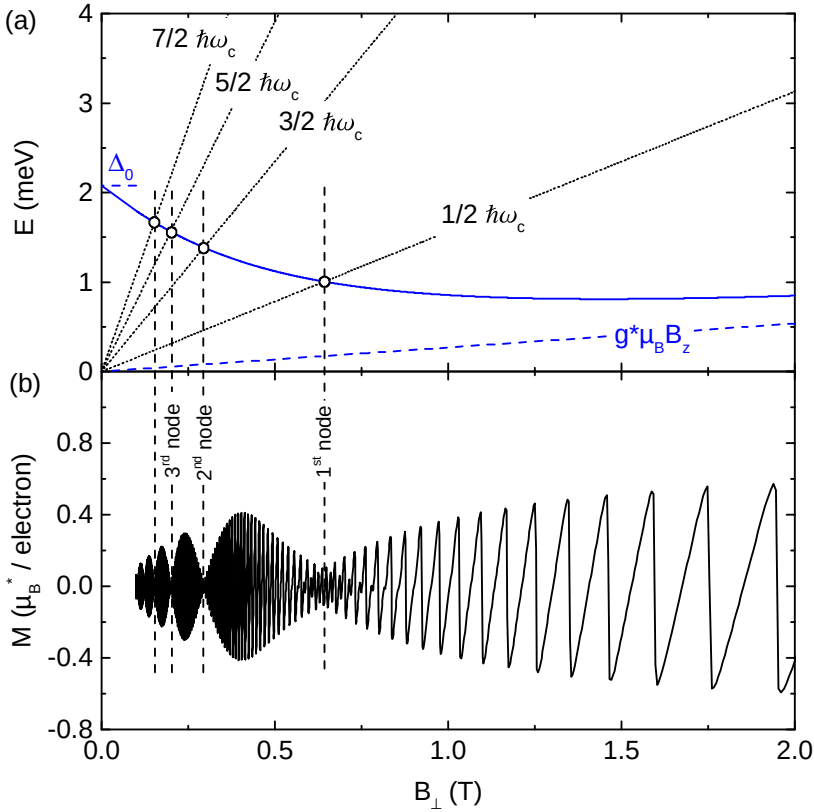

Figure 2.9: (a) Spin splitting Δ_s as a function of $B_\perp$ (solid blue line). Only Rashba SOI ($\alpha_R = 4.5 \times 10^{-12}$ eVm) as well as an isotropic g^* was taken into account. At $B_\perp = 0$, Δ_s is equal to the zero field spin splitting Δ_0, while at large fields the splitting approaches the Zeeman term $g^*\mu_B B$ (dashed blue line). Crossing points with energies $(j - 1/2)\,\hbar\omega_c$, $(j = 1, 2, ..)$ indicate beat node positions where the energy levels in the spectrum are equally spaced. (b) Corresponding magnetization curve $M(B_\perp)$ for the parameters used in (a), $\Gamma = 0.3\,\mathrm{meV}/\sqrt{\mathrm{T}}$ and $T = 0$.

neighboring states $|n, \pm\rangle$, and track the splitting between these states down to low $B_\perp$. This is done by diagonalizing H and finding the pair of eigenvectors with maximum projections on the initial eigenvectors of $|n, \pm\rangle$, respectively. $\Delta_s(B_\perp)$ is plotted in Fig. 2.9 (a). Starting from the zero field spin splitting $\Delta_0 = 2\alpha_R k_F$, Δ_s first decreases with increasing $B_\perp$ and finally approaches the Zeeman splitting $g^*\mu_B B_\perp$ [dashed line in Fig. 2.9 (a)]. The crossing points with energies $1/2\hbar\omega_c$, $3/2\hbar\omega_c$, ... indicate node positions as defined previously. In Fig. 2.9 (b), a corresponding magnetization $M(B_\perp)$ is displayed, using the same parameters as in (a) as well as $\Gamma = 0.3$ meV$/\sqrt{\mathrm{T}}$ and $T = 0$. The node positions found in (a) can be clearly identified in the quantum oscillations of M. While at the first node the amplitudes ΔM of even and odd filling factors are still finite, level broadening and a finite temperature reduce ΔM to zero at all subsequent node positions for this particular example.

2.4.2 Rashba splitting in tilted magnetic fields

We now allow the external field $\mathbf{B}$ to be tilted with respect to the 2DES plane by the polar angle θ. This manifests itself in the appearance of the off-diagonal Zeeman term in H, which depends linearly on the in-plane field $B_\parallel = (B_x, B_y)$. For the moment we still assume an isotropic g^* and neglect a Dresselhaus contribution. Hence, the energy spectrum remains independent of the azimuthal angle φ. If θ is increased, this will enlarge the Zeeman gap with respect to $\hbar\omega_c$, as discussed in section 2.3.1. This enlargement also enhances $\Delta_s(B_\perp)$ as displayed for different angles of θ in Fig. 2.10 (a). Most important is the fact that the node positions are shifted to higher field values as θ is increased. This shift is most pronounced for the first beat node. The evolution of the first node position as a function of θ is depicted in Fig. 2.10 (b). If the angle of half a coincidence $\theta_c^{1/2}$ is reached, the Zeeman gap becomes identical to $1/2\hbar\omega_c$. Hence, the crossing point of Δ_s with $1/2\hbar\omega_c$, i.e., the first beat node, is shifted to infinite $B_\perp$ and will disappear once $\theta > \theta_c^{1/2}$. A further increase of θ will move the second node until it disappears at $\theta_c^{3/2}$ etc.. This behavior has been addressed experimentally in magnetotransport measurements in Refs. [Luo+88; Das+89; Luo+90] and theoretically in Ref. [DDR90].

In addition to the shifts of node positions, a break-up of the degeneracy at level crossings for $\theta > 0$ is asserted because the off-diagonal Zeeman term leads to a coupling of previously degenerate states and opens an anticrossing gap. Therefore, the tracking of levels to calculate Δ_s fails at these field positions and $\Delta_s(B_\perp)$ is not continuous any more. This effect will reduce the oscillation amplitudes near the maxima of the beat envelopes.

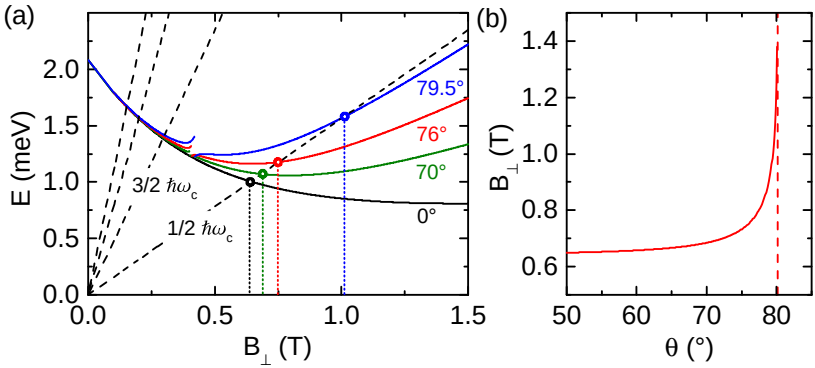

Figure 2.10: (a) Spin splitting Δ_s as a function of $B_\perp$ for four different tilt angles θ. The crossing points with $E = {}^1/_2\hbar\omega_c$ indicate the position of the first beat node. Interruptions of the curves at $B_\perp \approx 0.4\,\mathrm{T}$ at $\theta \neq 0$ are due to an anticrossing of levels. (b) Evolution of the first node position as a function of θ. The beat node vanishes once the coincidence angle $\theta_c^{1/2}$ is reached (dashed line). This graph revisits the work by Das, Datta and Reifenberger [DDR90].

2.4.3 Landau levels including both Rashba and Dresselhaus terms

Let us now consider the case if both Rashba and Dresselhaus terms are included in H. First, we restrict the discussion to perpendicular field orientation as well as an isotropic g^*-factor. As already pointed out in section 2.4, the definition of a zero-field spin splitting at the Fermi level Δ_0 becomes ambiguous in presence of R- and D-terms, because Δ_0 depends on the in-plane orientation of k_F [c.f. Fig. 2.6]. Nonetheless, it is instructive to calculate $\Delta_s(B_\perp)$ as described in section 2.4.1 to gain

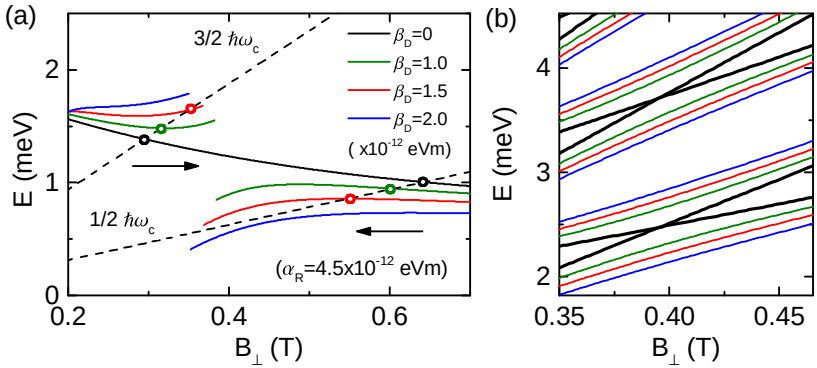

Figure 2.11: (a) Spin splitting $\Delta_s(B_\perp)$ for $\theta = 0°$, constant $\alpha_R = 4.5 \times 10^{-12}$ eVm and increasing β_D (solid curves). Field positions of the first and second beat node (indicated by circles) are the crossing points with $^1/_2\hbar\omega_c$ and $^3/_2\hbar\omega_c$ (dashed lines), respectively. (b) Corresponding energy spectra $E_{n'}(B_\perp)$. An anticrossing gap opens if $\beta_D \neq 0$ (colored curves) at previous crossing points present for $\beta_D = 0$ (black curve).

information about the node positions in $B_\perp$. We will start with a pure Rashba term ($\alpha_R = 4.5 \times 10^{-12}$ eVm) and illustrate what happens to the first and second node position if a Dresselhaus term $0 < \beta_D < \alpha_R$ is included. This is shown in Fig. 2.11 (a) for four different values of $\beta_D = (0, 1.0, 1.5, 2.0) \times 10^{-12}$ eVm. Similar to the presence of an off-diagonal Zeeman term, the Dresselhaus term opens an anticrossing gap at previous level crossing points [as illustrated in Fig. 2.11 (b)], but leaves the high-field asymptote $\Delta_s(B_\perp) \to g^*\mu_B B_\perp$ unchanged. Consequently, the first beat node moves in the *opposite* field direction, i.e. towards smaller fields. This means that first and second node move one toward another until they meet at a certain ratio of β_D/α_R and vanish afterwards, as it is the case for the blue curve in Fig. 2.11 (a). This is because the anticrossing gap has grown larger than $\hbar\omega_c$. For greater β_D (but still smaller than α_R), the beating in the amplitudes of the magneto-oscillations remains present, but the gap at odd ν will never exceed the one at even ν due to the absence of nodes. It has been pointed out by Tarasenko and Averkiev, that the beating in the magneto-oscillations in perpendicular fields vanishes completely once $\alpha_R = \beta_D$

and neglecting Zeeman splitting [TA02]. This is because the zero-field dispersion relation then consists of two horizontally shifted paraboloids in **k**-space with *identical* Fermi surfaces. These result in a two-fold degeneracy of the LLs similar to the case of an ideal spin-degenerate 2DES. [1]

As long as the first two beat nodes are still present, they can be used to derive α_R and β_D from the experimental magneto-oscillations under the assumption that m^*, g^* and $n_{2\mathrm{D}}$ are known for the given 2DES. However, there are two restrictions to that method. First, the energy spectrum $E_{n'}(B_\perp)$ is independent on the signs of α_R and β_D and depends only on their absolute values [Zha06]. For a qualitative understanding of this fact, we consider the zero-field DOS $D(E)$ of $|\alpha_R|, |\beta_D| > 0$, but for different relative signs, as illustrated in Fig. 2.6 (b) and (c). It is easy to see that $D(E)$ must be the same for both cases, because the respective dispersion relations in **k**-space are identical except for a 90°-rotation. A perpendicular magnetic field does not allow to distinguish between the two cases because it does not address any particular in-plane direction. Consequently, the $B_\perp$-dependent DOS $D(E, B_\perp)$, which effectively maps $E_{n'}(B_\perp)$, remains independent on $\mathrm{sgn}(\alpha_r/\beta_D)$. As a second restriction, we find that there are always two sets of (α_R, β_D), which yield the same set of node positions (e.g. a strong Rashba and a weak Dresselhaus contribution or vice versa). It is thus indispensable to use additional information in order to extract the correct parameter set from experimental magneto-oscillations.

In-plane anisotropy of node positions

In the following, we will show that both restrictions can be overcome by performing experiments in doubly tilted magnetic fields. Figure 2.12 (a) depicts $\Delta_s(B_\perp)$ at a tilt angle $\theta = 79°$ for two different in-plane orientations $B_\parallel \parallel [110]$ and $B_\parallel \parallel [1\bar{1}0]$, corresponding to $\varphi = 45°$ and $\varphi = 135°$, respectively. These are identical with the directions in **k**-space, where the zero-field spin splitting $\Delta_0(\varphi)$ exhibited extrema due to the presence of both R- and D-terms. One can see that the node positions vary for both orientations, most prominently for the first node. This is

[1] In presence of a Zeeman term, the LLs are generally not degenerate and the jumps in E_F will still perform weak beatings. However, the splitting Δ_s is always on the order of $g^*\mu_B B_\perp$ and does not lead to level crossings or beat nodes.

because we chose θ very close to the coincidence angle $\theta_c^{1/2} = 80.14°$ such that the crossing point of $\Delta_s(B_\perp)$ with $1/2\hbar\omega_c$ is very sensitive to the influence of off-diagonal terms in H. However, also for the second node, a shift in the opposite field direction is asserted. In Fig. 2.12 (b), the evolution of both node positions is plotted as a function of φ for different ratios β_D/α_R, while we kept $\alpha_R = 4.5 \times 10^{-12}$ eVm fixed. A significant anisotropy of both node positions is found once $|\beta_D| > 0$, with principal axes along the [110]- and [1$\bar{1}$0]- directions. This anisotropy is getting larger as $|\beta_D|$ is increased towards α_R. At a particular ratio of β_D/α_R, the first and second node meet at $\varphi = 135°$ and vanish upon a further increase of β_D/α_R, similar to the disappearance of the nodes in the perpendicular field case. However, the nodes are still visible within a certain φ-range around $\varphi = 45°$, which is getting smaller as $|\beta_D/\alpha_R|$ approaches one. In the case of $|\alpha_R| = |\beta_D|$, the nodes vanish completely and the condition of equally spaced levels is achieved only at the coincidence angle $\theta_c^{1/2}$ across the whole field range, similar to the case of pure Zeeman splitting.

Figure 2.12 (c) and (d) show polar plots of the two node positions for $|\beta_D/\alpha_R| = 0.33$ and different relative sign of α_R and β_D. We observe a 90°-rotation of the respective anisotropy-patterns for a sign reversal, which proves that tilted field experiments are sensitive to the relative sign as opposed to measurements with perpendicular field orientation. In addition, the combined φ-evolution of both nodes is *unique* for a particular set (α_R, β_D), i.e., there is no second set which leads to the same curves. Solely the absolute signs of α_R and β_D remain ambiguous, meaning that the cases (α_R, β_D) and $(-\alpha_R, -\beta_D)$ are not distinguishable.

Considering again the in-plane node evolutions shown in Fig. 2.12 (b), we conclude that the proposed method to extract α_R and β_D is suited especially for small ratios β_D/α_R, where both nodes are visible within the whole φ-range. A fitting of the model to experimentally observed node positions allows to determine the SOI parameters with high accuracy. The accuracy can even be enhanced by performing experiments at different tilt angles θ and considering additional nodes if they are visible in the experiment. If $\beta_D/\alpha_R \approx 1$, the absence of nodes within a rather large range of φ complicates the analysis of experimental data. In this case, different approaches have been proposed to address

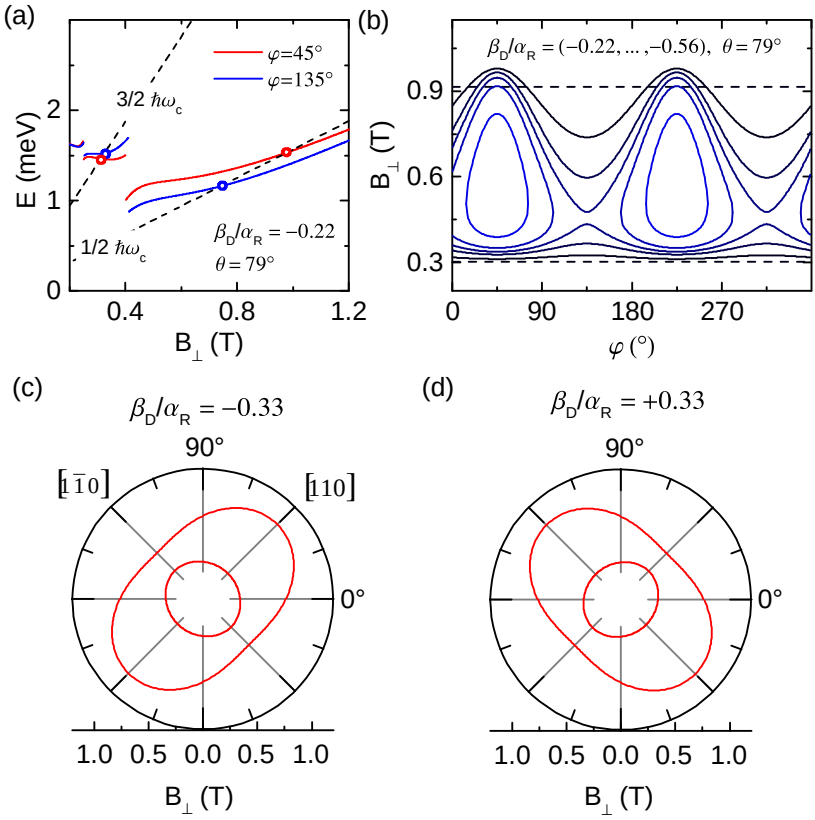

Figure 2.12: (a) Spin splitting $\Delta_s(B_\perp)$ and node positions for $\alpha_R = 4.5 \times 10^{-12}$ eVm and $\beta_D = -1.0 \times 10^{-12}$ eVm at a tilt angle $\theta = 79°$ for two different in-plane orientations $B_\parallel \parallel [110]$ ($\varphi = 45°$, red) and $B_\parallel \parallel [1\bar{1}0]$ ($\varphi = 135°$, blue). (b) Field positions of first and second node as a function of φ for different ratios $\beta_D/\alpha_R = (-0.22, -0.33, -0.44, -0.56)$ (from black to blue). α_R was fixed as in (a). Note that for larger β_D/α_R, both nodes meet at a particular φ and are absent within a certain range of φ. The dashed lines represent the (isotropic) case of $\beta_D = 0$. Polar plots of the node positions for different relative sign of α_R and β_D are depicted in panels (c) and (d), respectively.

α_R and β_D, e.g. to measure the anticrossing gap that occurs at a full coincidence as a function of the in-plane angle φ of the applied magnetic field $\mathbf{B}$ [WG13].

Finally, we want to discuss the case of an anisotropic $\overline{\overline{g}}^*$-tensor, as introduced in section 2.3.1. As opposed to an isotropic g^*, three independent parameters $g_\perp$, $g_\parallel$ and g_{xy} enter the Hamiltonian H [Eq. (2.42], while $g_\perp$ enters the diagonal terms and $g_\parallel$ and g_{xy} are present in the off-diagonal Zeeman term. It is generally not possible to simply replace the scalar g^* by the angle-dependent, but scalar $g^*(\theta, \varphi)$ [c.f. Eq. (2.33)] if off-diagonal SOI matrix elements are present. Quite the contrary, it is inevitable to know all of these parameters for a correct description of the system. Especially the in-plane anisotropy of $\overline{\overline{g}}^*$, provoked by the parameter g_{xy}, will affect the in-plane evolution of the node positions as discussed previously. This is because the asymptote $g^*\mu_B B$ will vary as a function of in-plane orientation and significantly shift the curve $\Delta_s(B_\perp)$. Hence, the position of the first beat node, i.e., the crossing point of Δ_s with $1/2\hbar\omega_c$, will shift with the in-plane angle φ. The in-plane anisotropy of $\overline{\overline{g}}^*$ thus causes an additional contribution to the in-plane evolution of node positions as introduced in Fig. 2.12 (b), which is not separable from the node-shift due to R- and D-terms. Consequently, the parameters of the $\overline{\overline{g}}^*$-tensor, especially g_{xy}, have to be determined in independent experiments.

2.4.4 Contribution of k-cubic terms

In this section we briefly outline the impact of k-cubic terms stemming from the BIA contribution and discuss their relevance on the energy spectrum for the specific InP/InGaAs heterostructure observed in this work. Starting from Eq. (2.37), we re-write the full BIA Hamiltonian H_D as

$$H_\mathrm{D} = -\gamma\langle k_z^2\rangle(\sigma_x k_x - \sigma_y k_y) \;+\; \gamma(\sigma_x k_y k_x k_y - \sigma_y k_x k_y k_x)\,. \qquad (2.45)$$

The first summand is the (k_x, k_y)-linear term which we already included in the modeling, while the second summand represents the previously neglected (k_x, k_y)-cubic contribution. Note that in Eq. (2.45), the k_i are *operators* defined as $\hbar k_i := \pi_i$. At nonzero $\mathbf{B}$, the k_i do not commute. For this reason, the symmetric order of the k_i in the (k_x, k_y)-cubic

summand is essential for H_D to be Hermitian [GFR85]. If we calculate the non-zero matrix elements of H_D and use the approximation (2.43), we find [DDR90]

$$\langle n,-|H_\mathrm{D}|n+1,+\rangle = i\gamma\left(\langle k_z^2\rangle - \frac{1}{4}k_\mathrm{F}^2\right)k_\mathrm{F} = -i\beta_\mathrm{D}' k_\mathrm{F} \tag{2.46}$$

$$\langle n,+|H_\mathrm{D}|n+3,-\rangle = -\frac{i\gamma}{4}k_\mathrm{F}^3\,. \tag{2.47}$$

A detailed derivation of these terms is given in appendix B.2. First, we find that the original matrix element $\langle n,-|H_\mathrm{D}|n+1,+\rangle = i\gamma\langle k_z^2\rangle k_\mathrm{F}$ is replaced by the term (2.46). This does not change the energy spectrum qualitatively, but necessitates the replacement of the Dresselhaus parameter $\beta_\mathrm{D} = -\gamma\langle k_z^2\rangle$ by a corrected $\beta_\mathrm{D}' = -\gamma(\langle k_z^2\rangle - {}^1\!/_4 k_\mathrm{F}^2)$. Consequently, we always measure β_D' instead of β_D in the experiment. Nevertheless, we will use the notation β_D for the D-parameter in the discussion of experiments because we cannot distinguish between the two. The second matrix element [Eq. (2.47)] arises as an additional term and thus influences $E_{n'}(B_\perp)$ qualitatively. We now want to estimate the quantitative impact of Eq. (2.47) on the spectrum using realistic system parameters. An approximate value for $\langle k_z^2\rangle$ is given by $(\pi/w)^2$, where w is the width of the QW [DDR90]. The Fermi wave vector k_F is given by the electron density via $k_\mathrm{F} = \sqrt{2\pi n_\mathrm{2D}}$. For our InP/InGaAs heterostructure, $w \approx 10\,\mathrm{nm}$ and $n_\mathrm{2D} \approx 8.5\times10^{15}\,\mathrm{m}^{-2}$, and we obtain

$$|\langle n,-|H_\mathrm{D}|n+1,+\rangle| \approx \gamma \times (0.02\,\mathrm{nm}^{-3}) \tag{2.48}$$

$$|\langle n,+|H_\mathrm{D}|n+3,-\rangle| \approx \gamma \times (0.003\,\mathrm{nm}^{-3})\,. \tag{2.49}$$

Obviously, the additional matrix element $\langle n,+|H_\mathrm{D}|n+3,-\rangle$ is by a factor of ≈ 7 smaller than $\langle n,-|H_\mathrm{D}|n+1,-\rangle$. Furthermore, with second order perturbation theory we can estimate the correction induced by an off-diagonal matrix element on a specific energy E_n via $\Delta E_n \approx |\langle n|H_\mathrm{D}|m\rangle|^2/(E_n - E_m)$. Since Eq. (2.46) couples states with orbital quantum number n and $n+1$, the energy difference yields $\hbar\omega_c$. The additional matrix element [Eq. (2.47)] couples n and $n+3$, implying $E_{n+3} - E_n = 3\hbar\omega_c$. Following this evaluation, we find that the correction of E_n due to Eq. (2.47) is by more than two orders of magnitude smaller. We therefore conclude that the negligence of (2.47) is justified

in the modeling of $E_{n'}$ for the specific heterostructure treated in this work. The main impact of the cubic terms is included in the effective Dresselhaus parameter β'_{D}.

2.5 Energy levels of quantum dots

In chapter 7 we will present experimental magnetization data on nanopatterned InP/InGaAs heterostructures forming arrays of quantum dots. The nanopatterning leads to an additional lateral confinement of the 2DES in the (x, y)-plane. Due to the circular symmetry of the dots, a confinement potential of the form $V(x, y) = V(r)$ is assumed. In this section, we will recapitulate the single-particle energy spectra of quantum dots considering different shapes of $V(r)$. Furthermore, we calculate corresponding magnetization curves and show how the dHvA-oscillations are altered in the presence of different $V(r)$. We restrict ourselves to the widely used cases of a parabolic confinement potential [Ker+90; KS05] and a flat potential with hard walls (HW potential) [LFS88; KLS90]. In anticipation of the experimental results, we state that signatures of spin splitting were not observed in the data. Therefore we neglect these terms in the following treatment. The Hamiltonian of the problem reads

$$H = \frac{\boldsymbol{\pi}^2}{2m^*} + V(r) \ . \tag{2.50}$$

We assume a magnetic field $\mathbf{B} = (0, 0, B)$ perpendicular to the 2DES plane and neglect effects of an in-plane field on the energy spectrum. This is justified for $\hbar\omega_c$ much smaller than the 2DES subband confinement, which holds true for the observed structures. Furthermore, we neglect effects of finite T, since in the experiment $k_B T \ll \hbar\omega_c$ within the relevant field range.

To derive magnetization curves from the calculated spectra, we first calculate the free energy $F(B)$ by successively filling up single particle levels with electrons up to a fixed electron number N. Secondly, we derive the magnetization via $M = -\partial F/\partial B$.

2.5.1 Parabolic confinement

A parabolic confinement potential is defined as

$$V(r) = \frac{1}{2} m^* \omega_0^2 r^2 \ , \tag{2.51}$$

where $\hbar\omega_0$ is referred to as the confinement energy. The given eigenvalue problem was first addressed by Fock and Darwin in the late 1920s [Foc28; Dar31]. They found an analytic solution, yielding the so-called Fock-Darwin (FD) energies

$$E_{nl} = \left(n + \frac{|l|}{2} + \frac{1}{2} \right) \hbar\omega + \frac{l}{2} \hbar\omega_c \ . \tag{2.52}$$

Here, $\omega_c = eB/m^*$ is the cyclotron frequency, $\omega = \sqrt{\omega_c^2 + 4\omega_0^2}$ and $n = \{0, 1, 2, ...\}$, $l \in \mathbb{Z}$ are two independent quantum numbers. We can express the energy spectrum (2.52) in dimensionless units by substituting $x_0^{\mathrm{FD}} = \omega_c/\omega_0$ and $\epsilon_{nl} = E_{nl}/(\hbar\omega_0)$ and obtain

$$\epsilon_{nl} = \left(n + \frac{|l|}{2} + \frac{1}{2} \right) \sqrt{\left(x_0^{\mathrm{FD}}\right)^2 + 4} + \frac{l}{2} x_0^{\mathrm{FD}} \ . \tag{2.53}$$

Using this transformation, also the magnetization can be expressed in dimensionless units after calculating the dimensionless free energy f for a fixed number of electrons N and evaluating $m = -\partial f / \partial x_0^{\mathrm{FD}}$. The actual magnetization $M(B)$ is then obtained via $M = m(e\hbar)/m^*$, while $B = ((m^*\omega_0)/e) \cdot x_0^{\mathrm{FD}}$. From this transformation one can see that the *shape* of the magnetization curve $M(B)$ depends on the number of electrons N only and *does not depend* on the input parameters ω_0 and m^*. We calculated $m(x_0^{\mathrm{FD}})$ for $1 \leq N \leq 2000$ and derived $M(B)$ for specific ω_0, m^* and N by simply rescaling the m and x_0^{FD}-axes. This approach enabled an enormous speed-up of the computation of large sets of $M(B)$ for different ω_0, m^* and N. In particular, this is facilitated the calculations including inhomogeneous broadening (see 7.3), which required the superposition of thousands of curves with distributed input parameters.

In Fig. 2.13 $E_{nl}(B)$ and $M(B)$ are plotted in units of $\hbar\omega_0$ and $(e\hbar)/m^*$, respectively. The Fermi energy E_{F} for $N = 100$ is indicated by a thick

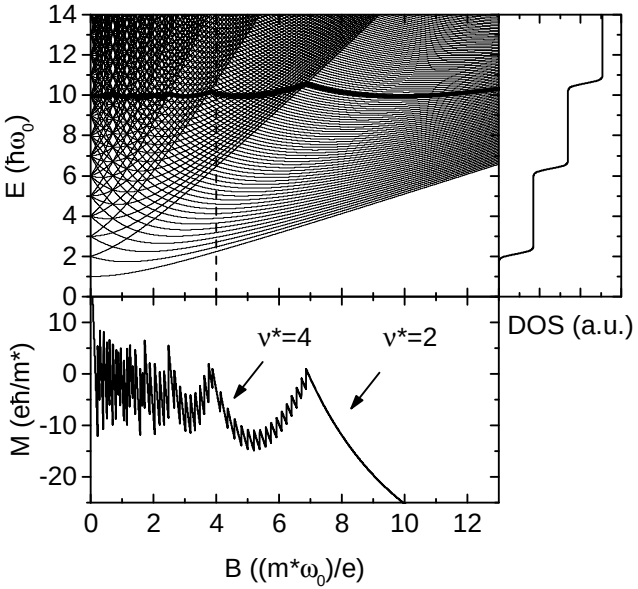

Figure 2.13: Energy spectrum $E(B)$ in units of $\hbar\omega_0$ for a parabolic confinement potential $V(r) = {}^1\!/_2\, m^*\omega_0^2 r^2$ (top panel). A vertical cross-section (dashed line in the spectrum) was employed to calculate the (broadened) density of states $D(E)$ at a particular field B (right panel). The Fermi energy for $N = 100$ is emphasized with a thick line in the spectrum. The corresponding magnetization curve $M(B)$ is plotted in the bottom panel. Effective filling factors $\nu^* = 2$ and $\nu^* = 4$ as attributed to the downward flanks of M are indicated by arrows.

line in the spectrum. We observe that the discrete eigenstates of a 2D harmonic oscillator at $B = 0$ perform level crossings if B is increased and group together into sets at large B, similar to the grouping of free electron levels into highly degenerate Landau levels in a 2DES. However, a degeneracy of levels at high magnetic fields is not asserted. We illustrate this by calculating the density of states

$$D(E) = \sum_{n,l} \delta_a(E - E_{nl}) \tag{2.54}$$

for a specific field B (dashed line in the spectrum in Fig. 2.13) with a Gaussian kernel function $\delta_a(E)$. The width of $\delta_a(E)$ was chosen such that the DOS is smeared out over neighboring single particle levels while preserving features on the scale defined by the level sets. It is clear from the plot that $D(E)$ increases in a stepwise manner as E increases from one level set to the next and does not exhibit a condensation of levels at certain energies, as it is the case for 2DES Landau levels.

Similar to the Fermi energy E_F, the magnetization $M(B)$ exhibits two types of oscillations: a fast oscillation due to crossings of single particle levels and a much slower oscillation, which is governed by the transition of the Fermi energy from one level set to the next. The former is known to be quasi-periodic in B and therefore referred to as Aharonov-Bohm (AB)-type [SI88]. The latter is dHvA-type and quasi-periodic in $1/B$. The period of the AB-type oscillation in the magnetic field B is on the order of one magnetic flux quantum $\Phi_0 = h/e$ per dot area [SI88]. In an ensemble, the amplitude of the AB-type oscillations is expected to decrease with the square root of the total number of dots compared to the dHvA-type oscillations due to the statistical spread of input parameters such as N and ω_0 [SI88]. The rapid oscillations are thus likely to be suppressed in a large ensemble as treated in this work, and we therefore neglect them in the following.

The dHvA-type oscillations exhibit a cusp-like shape as opposed to sawtooth-shaped dHvA-oscillations of a 2DES. This is a consequence of the modified DOS. Due to the lack of condensed level sets, the Fermi energy does not exhibit discrete jumps, but performs a continuous transition from one level set to the next. This is also reflected in the magnetization signal. It is instructive to define effective filling factors ν^*, which we attribute to the downward flanks of the dHvA-type oscillations in $M(B)$, or to the upward flanks in $M(1/B)$. The ν^* are chosen to be consistent with the definition of $\nu = n_\mathrm{2D}/(eB/h)$ of a 2DES with similar dHvA frequency.

Estimation of the dHvA frequency

The dHvA-type oscillations in M produced by the FD model show slight deviations from a strict $1/B$- periodicity. In the following, we derive an approximate value of the oscillation frequency $f_{1/B}$ in terms of input parameters m^*, ω_0 and N. The estimation of $f_{1/B}$ from the full

quantum mechanical treatment as presented above is difficult, because a definition of field values with equivalent phase is not straightforward. We therefore employ a simplified approach to model these oscillations that has been put forward by Fogler *et. al.* [FLS94]. In their model they assumed that at a certain position r, the energy spectrum still consists of Landau levels with a degeneracy per unit area $N_L = 2eB/h$. However, the energy of the LLs varies in space according to the shape of the lateral confinement potential $V(r)$ as depicted in Fig. 2.14 (a). The Fermi energy is assumed to be constant, which results in a filling of the LLs that varies in space. This approach is able to model the dHvA-type oscillations, but does not account for the quick AB-type oscillations, because single particle levels are not reproduced. A comparison of the magnetization derived by both models with identical input parameters is depicted in Fig. 2.14 (b). Considering the dHvA-type oscillations, both curves agree quite well at high magnetic fields. Only in the low field limit the FD model predicts phase-shifts towards lower field values. Fogler's approach is thus well suited to extract an approximation for $f_{1/B}$.

In the following, we use the peak positions of the cusp-like dHvA-type oscillations to address their periodicity in $1/B$ and to estimate $f_{1/B}$. To do that, it is not necessary to perform the complete derivation of E_F, F and M using Fogler's model. However, we identify that the peaks occur at field values, where E_F touches the next LL in the center of the dot as sketched in Fig. 2.14 (a). If we denote the number of filled LLs below E_F at the center of the dot by n_f, we obtain for the total number of electrons

$$N = \sum_{n=0}^{n_f-1} (\pi r_n^2) N_L \tag{2.55}$$

with the LL index n and the LL degeneracy $N_L = 2eB/h$. Here, the LL with index n is filled with electrons within a disk of radius r_n. In the special case where E_F just touches the LL with index n_f, r_n is given by

$$r_n^2 = \frac{2}{m^* \omega_0^2} (n_f - n) \hbar \omega_c \ . \tag{2.56}$$

Notice that r_n decreases with increasing level index n and becomes zero if $n = n_f$, i.e., the level with index n_f is empty and just about to get

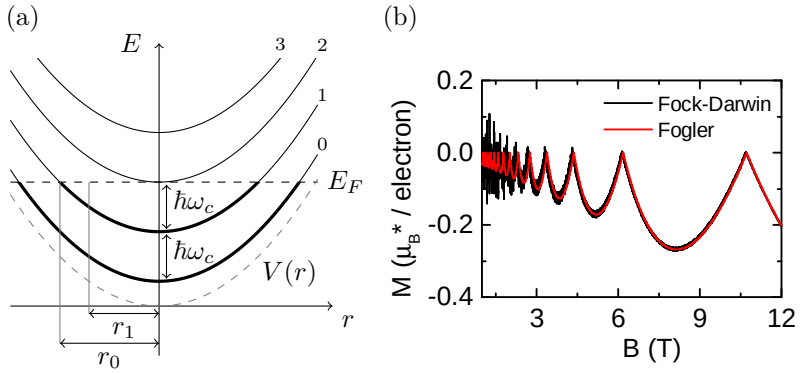

Figure 2.14: (a) Sketch of Fogler's ansatz [FLS94] to model parabolic confinement. The degenerate LLs $(n + 1/2)\hbar\omega_c$, shown for $n = 0, 1, 2, 3$ are bent in space according to $V(r) = 1/2 m^* \omega_0^2 r^2$. Levels that lie partly below E_F are filled within a particular disk of radius r_n, as indicated by thick lines for $n = 0$ and $n = 1$. (b) Comparison of calculated magnetization curves using FD (black) and Fogler's model (red). Simulation parameters were $\hbar\omega_0 = 1.5\,\mathrm{meV}$, $N = 1000$ and $m^* = 0.037$.

filled. In that sense, $n_f = 2\nu^*$ can be understood as twice the effective filling factor as defined previously, while the factor of two stems from spin degeneracy. Using Eq. (2.56), the summation in Eq. (2.55) yields

$$N = \frac{\omega_c^2}{\omega_0^2} n_f (n_f + 1) \approx \frac{\omega_c^2}{\omega_0^2} n_f^2 \,. \tag{2.57}$$

Here, we made the approximation $n_f \gg 1$, which implies that the estimation of $f_{1/B}$ in this model is valid only for large n_f. Now we can reconvert Eq. (2.57) to reveal $1/B$ positions of the sharp dHvA-type peaks as a function of n_f:

$$\left(\frac{1}{B}\right)_{n_f} = \frac{e}{\omega_0 m^* \sqrt{N}} \, n_f \tag{2.58}$$

We notice that $(1/B)_{n_f}$ increases linearly with n_f, and the frequency $f_{1/B}$ is given by the inverse of the respective prefactor:

$$f_{1/B} = \omega_0 \sqrt{N} \frac{m^*}{e} \tag{2.59}$$

From the analysis it is clear that $f_{1/B}$ is only an estimate of the dHvA-frequency. Without the above approximations, the dHvA-type oscillations predicted by the the FD model deviate from the strict $1/B$-periodicity. A more detailed analysis of periodicity and phase of the dHvA-type oscillations in M produced by the FD model will be discussed in 7.3.

2.5.2 Hard-wall confinement

We now review the energy spectrum of a flat confinement potential with hard walls at the edges, defined as

$$V(r) = \begin{cases} 0, & r \leq R_0 \\ \infty, & r > R_0 \end{cases} , \tag{2.60}$$

where R_0 is the confinement radius. For the exact derivation of the eigenvalues $E_{nl}(B)$ we refer the reader to the paper of Geerinckx *et. al.* [GPD90]. Following their analysis, $E_{nl}(B)$ can be expressed as

$$E_{nl} = \hbar\omega_c \left(\alpha_{nl} + \frac{l + |l|}{2} + \frac{1}{2} \right) , \tag{2.61}$$

where α_{nl} is calculated numerically via

$${}_1F_1(-\alpha_{nl}, |l| + 1, x_0^{\mathrm{HW}}) = 0 , \tag{2.62}$$

with the confluent hypergeometric function ${}_1F_1$ and $x_0^{\mathrm{HW}} = R_0^2/(2l_B^2)$. In analogy to the FD states, we find a dimensionless representation of (2.61):

$$\epsilon_{nl} = \left(\alpha_{nl} + \frac{l + |l|}{2} + \frac{1}{2} \right) x_0^{\mathrm{HW}} , \tag{2.63}$$

where $B = (2\hbar)/(eR_0^2)x_0^{\mathrm{HW}}$ and $E_{nl} = (2\hbar^2)/(m^*R_0^2)\epsilon_{nl}$. Similar to the FD model, the shape of ϵ_{nl} does not depend on R_0 or m^* and the magnetization $M(B)$ is obtained for a specific N via rescaling the relevant axes. The attained speed-up in computation is even more effective for the HW model, because the numerical calculation of the α_{nl} is computationally more expensive.

We plotted the spectrum $E_{nl}(B)$ together with $E_{\mathrm{F}}(B)$ and $M(B)$ for a dot with $N = 100$ in Fig. 2.15. As in the FD model, single particle levels group into level sets as B is increased. However, the levels of the HW model approach $E = (n + 1/2)\hbar\omega_c$ and the case of an unconfined 2DES is recovered for $R_0 \to \infty$ (i.e. $N \to \infty$). This also manifests itself in the respective DOS, where pronounced peaks are present near LL positions $(n + 1/2)\hbar\omega_c$. A close look reveals that the peaks in the DOS are asymmetric. This is because the single particle levels approach the LL positions from the high-energy side only, thereby increasing the DOS on that side. Between the peaks a small background DOS background is present which linearly increases with n. The dHvA-type oscillations predicted by the HW model resemble a sawtooth waveform, but the slope of the downward flanks in $M(B)$ is finite due to the residual DOS between the LL-related peaks. This effect becomes more pronounced for larger ν^* where the asymmetry of the oscillation even gets reversed, i.e., the upward flanks are getting steeper than the downward flanks. However, these effects become less prominent if more and more electrons are added to the dot and the spectrum approaches the 2DES limit.

The frequency of the dHvA-type oscillations predicted by the HW model can be estimated by calculating the respective 2D density within one dot as $n_{\mathrm{2D}}^{\mathrm{dot}} = N/(2\pi R_0^2)$ and by using Eq. (2.14). We obtain

$$f_{1/B_\perp} = \frac{N}{\pi R_0^2}\frac{h}{e} \,. \tag{2.64}$$

2.5.3 Comparison of 2DES, HW and FD models

We now briefly compare the magnetization curves predicted by FD and HW model. For this, we assumed $N = 1600$ for both models and chose $\hbar\omega_0 = 1.557\,\mathrm{meV}$ and $R_0 = 230\,\mathrm{nm}$ to obtain similar dHvA-frequencies (the effective mass was set to $m^* = 0.037m_0$).

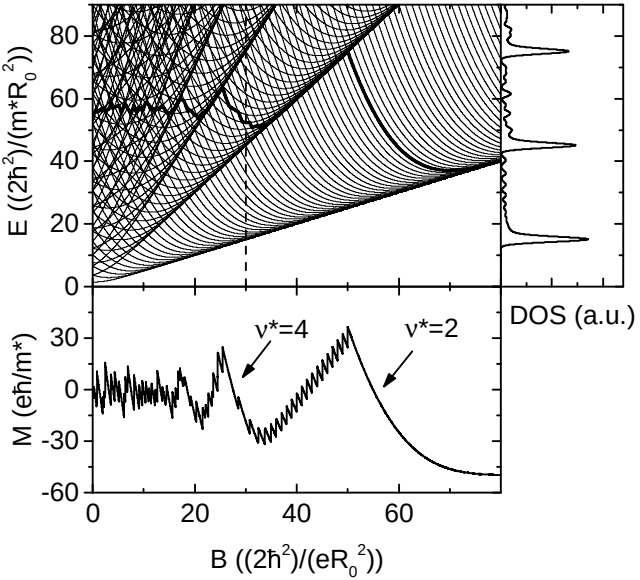

Figure 2.15: Energy spectrum $E(B)$ (top panel), density of states $D(E)$ (right panel) and magnetization $M(B)$ as calculated for hard-wall confinement. For the Fermi energy $E_\mathrm{F}(B)$ (thick line in the spectrum) and the magnetization $M(B)$, $N = 100$ was assumed. Effective filling factors $\nu^* = 2$ and $\nu^* = 4$ as attributed to the downward flanks of M are indicated by arrows.

Calculated magnetization curves are plotted in Fig. 2.16 as a function of $1/B$ in units of the effective Bohr magneton $\mu_\mathrm{B}^* = (e\hbar)/(2m^*)$. $M(B)$ of an ideal 2DES is also plotted for comparison. First, we note that the dHvA-type oscillations predicted by both FD and HW model fade out towards small B, because the energy spectrum is governed more and more by confinement effects rather than Landau quantization as B is decreased. Second, we observe a notable overall reduction of the dHvA amplitude of the FD model with respect to the HW model and the ideal 2DES. This can be explained by the strong modification of the DOS due to the absence of LL-like condensation of levels and discontinuous jumps of E_F, thereby leading to a smoothing of the oscillations. Using Fogler's model, the signal in M can be understood as the superposition of

many different sawtooth-shaped signals with individual dHvA frequency, stemming from the variation of the local density $n_{2D}(r)$ generated by the parabolic $V(r)$. Such a distribution of frequencies naturally reduces the amplitude of the sum signal.

For the HW model, the asymmetry of the oscillations in M changes from from 2DES-like (steep upward flanks) to the opposite (steep downward flanks) as B decreases, while no significant asymmetry is asserted for the FD model. Both curves show deviations from the strict $1/B$ periodicity that is present for an ideal 2DES. These deviations are more pronounced for the FD model. We will discuss these deviations in detail in section 7.3, where we compare the models to experimental data.

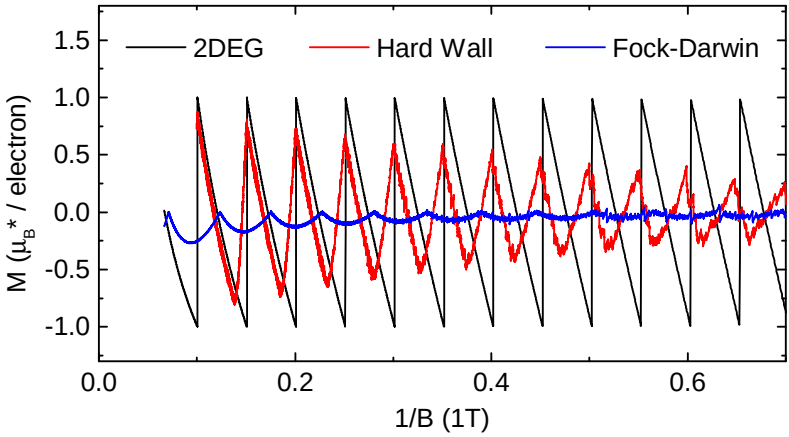

Figure 2.16: Comparison of the magnetization $M(1/B)$ of an ideal 2DES (black curve), and quantum dots with hard wall confinement (red curve) and parabolic confinement (blue curve). Parameters were $N = 1600$ and $m^* = 0.037$ (all models) as well as $\hbar\omega_0 = 1.557\,\text{meV}$ and $R_0 = 230\,\text{nm}$ for FD and HW model, respectively. The parameters were chosen to obtain similar $f_{1/B}$ for all curves.

3 Samples and experimental setup

In this chapter, we present sample details and describe the different experimental techniques that were employed in this thesis. The chapter is organized as follows. First, we outline the investigated sample structures and preparation methods. Second, we introduce the technique of torque cantilever magnetometry and discuss different readout schemes. Finally, we sketch our setup used for magnetotransport measurements.

3.1 Sample details and preparation

All samples investigated in this thesis were prepared from InP/InGaAs heterostructures provided by H. Hardtdegen and Th. Schäpers from Jülich research center. These structures were grown on (001)-oriented InP substrates by metal organic vapor phase epitaxy (MOVPE) [Har+93], with a layer sequence as sketched in Fig. 3.1 (a). A strained modulation-doped 10 nm-wide $In_{0.77}Ga_{0.23}As$ quantum well (QW) was sandwiched between InP and lattice-matched $In_{0.53}Ga_{0.47}As$ barrier layers. These structures had been carefully engineered in order to optimize the electron mobility in the QW, which allowed to investigate quantum oscillations down to very low magnetic fields. The choice of InP substrates enabled defect-free epitaxial growth of InGaAs layers with high In content featuring small effective electron masses.

Furthermore, the large atomic mass of In gave rise to strong spin-orbit interaction (SOI) for conduction electrons. The present structure was optimized to exhibit dominant Rashba-SOI due to the asymmetry of the QW barrier heights as well as a built-in electric field induced by single-sided modulation doping. A plot of the calculated conduction band edge of the layer cross section [Fig. 3.1 (b)] illustrates this asymmetry.

The investigation of SOI effects in these structures was one of the main purposes of this thesis.

In the following, we briefly outline the design and preparation of 2DES flip-chip samples, Hall-bars and quantum dot mesa structures that were prepared from this type of InP/InGaAs heterostructures.

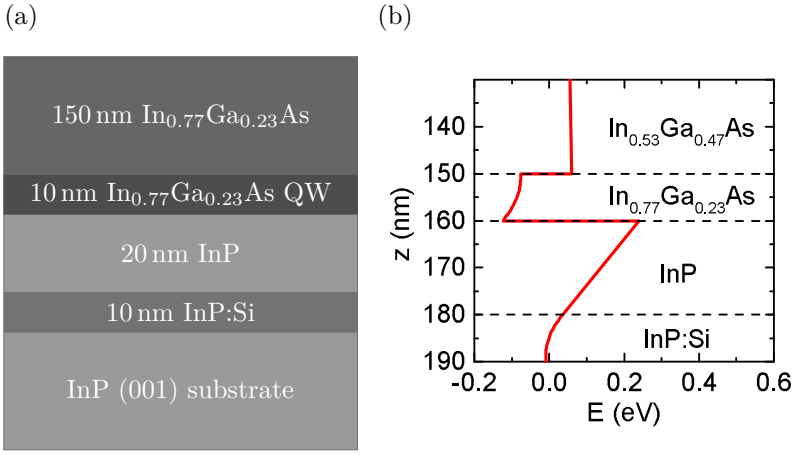

Figure 3.1: (a) Epitaxial layer sequence of the investigated InP/InGaAs heterostructure with the growth direction $\hat{z} \parallel [001]$. Numbers denote thicknesses. (b) Calculated energy diagram of the conduction band edge as a function of z [Kno04].

3.1.1 2DES flip-chip samples

Magnetometry experiments were performed on contacted and gated flip-chip samples which were subsequently placed on dedicated micromechanical cantilever magnetometers as explained further down in 3.2.3. A schematic cross-sectional view of these samples is depicted in Fig. 3.2 (a). Detailed information on the preparation process can be found in Ref. [Ibr13]. The structure consisted of a rectangular mesa of $(1.23 \times 0.78)\,\mathrm{mm}^2$ in size as defined by optical lithography and wet chemical etching. Four AuGe ohmic contacts at the corners were created

by evaporation and thermal annealing. The Au top gate was separated from the mesa surface by a 60 nm-thick Al_2O_3 insulating layer grown by atomic layer deposition (ALD). In a final step, the actual flip-chip samples were micro-machined from the bulk InP wafer. They were thinned down to $\approx 10\,\mu$m to reduce their weight and properly sized ($1.1 \times 1.9\,\text{mm}^2$) to fit on the paddle of the cantilever. A photograph of such a flip-chip sample including mesa, contacts and gate is shown in Fig. 3.2 (b).

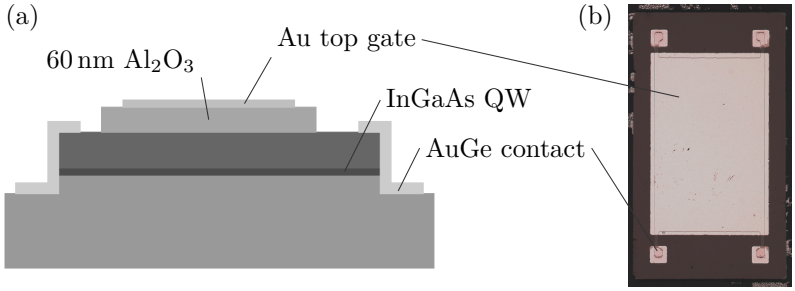

Figure 3.2: (a) Schematic cross-sectional view of the flip-chip sample including evaporated AuGe contacts, 60 nm Al_2O_3 gate insulating layer and Au top gate. (b) Optical microscope image of a prepared flip chip sample (top view).

3.1.2 Hall bar samples

Samples structured into Hall bars were provided by the group of Th. Schäpers at Jülich research center. These samples were used for magnetotransport measurements. The Hall bar mesa structures were $(700 \times 200)\,\mu\text{m}^2$ in size and featured two contacts for current injection and six contacts serving as voltage probes. A photograph of such a Hall bar sample is shown in Fig. 3.3 (a).

For the magnetotransport experiments presented in chapter 6, it was crucial to know the in-plane crystallographic orientation of the samples. For this, we performed a surface etch test following the experiment. The sample Hall bars were etched for 2 min in a HCl:H_3PO_4 (1:5) solution. A microscope image of the etched surface is depicted in Fig. 3.3 (b).

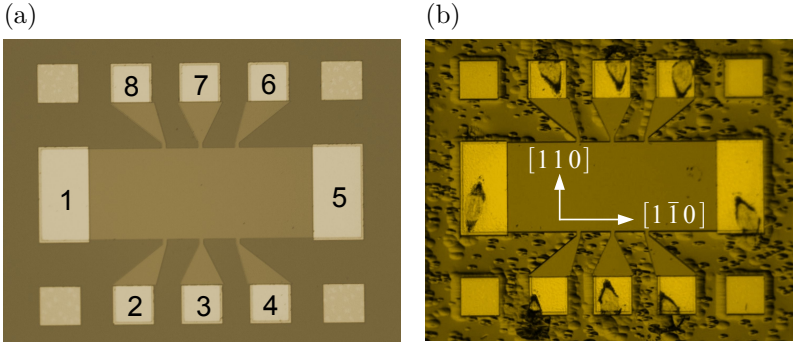

Figure 3.3: (a) Optical microscope image of a Hall bar mesa structure featuring two contacts for current injection (indexed 1 and 5) and six contacts that served as voltage probes (2-4, 6-8). (b) Microscope image of the same Hall bar after bonding and etching for 2 min in HCl:H_3PO_4 (1:5) solution. Oval-shaped surface pits revealed the in-plane orientation with respect to the crystal axes (indicated by arrows).

On the (001)-InP-facet that surrounds the mesa, oval-shaped surface pits with orientation parallel to the Hall bar were asserted. Following Refs. [Eli+99; Eli+04], these pits are oriented along the $[0\bar{1}1]$ direction. Hence, we assigned the in-plane orientation with $[0\bar{1}1]$ parallel to the Hall bar mesa, as indicated in Fig. 3.3 (b).

3.1.3 Quantum dot mesa structures

In order to study the quantum oscillatory magnetization of confined electron systems, we prepared etched ensembles of quantum dots. The preparation process is outlined in Fig. 3.4 (a)-(c). Via electron beam lithography, we defined 2D hexagonal arrays of circular dots with a lattice constant of 750 nm and a dot diameter of 460 nm. Each individual sample contained $4 \times 8 = 32$ write fields of $(200 \times 200)\,\mu\text{m}^2$ in size, totaling a number of $\approx 2.5 \times 10^6$ dots. After developing, a 30 nm-thick layer of Ti was evaporated. For the e-beam process, we used a double layer polymethyl methacrylate (PMMA) resist (50k / 950k) to facilitate the lift-off process. The Ti hard mask was used to obtain a better selectivity towards reactive ion etching (RIE) of the mesa. The

RIE etching was done by Sebastian Heedt at Forschungszentrum Jülich using a H_2/CH_4-process, which allowed for steep etch profiles. The etch depth of 320 nm was chosen to be below the InP:Si doping layer. Next, the Ti mask was removed by short HF wet chemical etching. A scanning electron microscopy (SEM) image of the prepared dot ensemble is depicted in Fig. 3.4 (d).

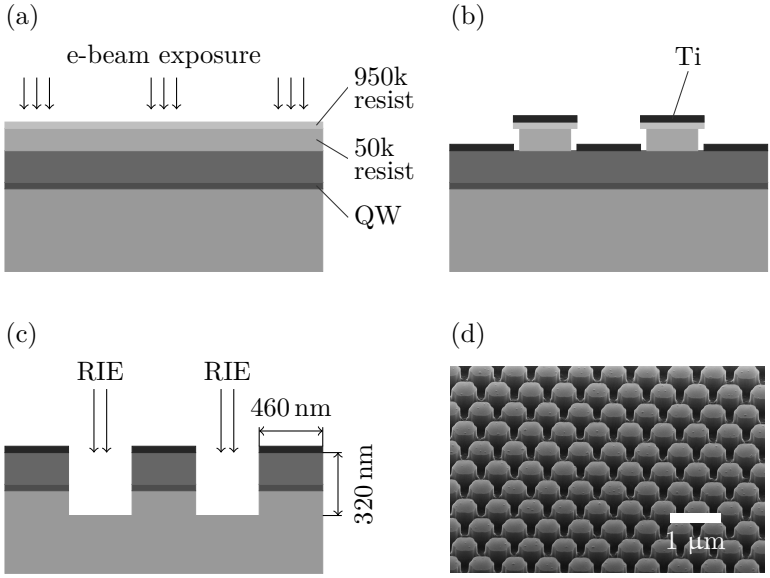

Figure 3.4: (a)-(c) Preparation process of quantum dot mesa structures. The dots were defined by e-beam lithography using a double-layer PMMA resist. A Ti hard mask was defined via subsequent evaporation and lift-off. The mesa dots were then etched by a RIE H_2/CH_4-process. (d) SEM image (bird's eye view) of the quantum dot ensemble after preparation.

In a final step, the samples were thinned and sized to fit on the paddle of capacitive micromechanical cantilevers. This was done by micro-machining the bulk InP wafers, similar to the fabrication of the flip-chip samples.

3.2 Micromechanical cantilever magnetometer

The measurement of the quantum oscillatory magnetization $M(B)$, i.e., the de Haas-van Alphen effect, is experimentally challenging for single-layered 2DES due to the very small signal strength of order 10^{-13} J/T per mm^2 of sample area. Therefore, dedicated magnetometers featuring a high sensitivity are needed for these kind of experiments. Reviews which summarize the available methods can be found e.g. in Refs. [UE09] and [WGH10]. Most commonly, the detection of $M(B)$ of 2DESs was carried out with superconducting quantum interference devices (SQUIDs) [Stö+83; Mei+01] as well as torsional [HA30; Eis85; Tem88; Wie+97] or cantilever magnetometers [CCN92; Har+99; Sch+00].

In this thesis, a cantilever magnetometer based on the design developed by Schwarz *et. al.* [Sch+00] was used. In the following, we briefly explain the principle of operation and discuss capacitive and optical readout schemes as well as absolute calibration procedures. Furthermore, we report on an improvement of the optical readout technique that allowed to effectively decrease the sample temperature.

3.2.1 Principle of operation

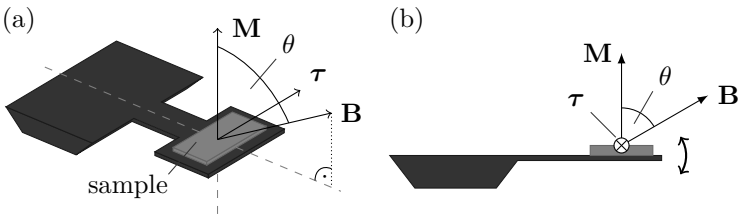

Figure 3.5: (a) Schematic drawing of the micromechanical cantilever magnetometer (MCM) with a sample placed on the cantilever paddle. If the magnetization of the sample **M** and the external magnetic field **B** form an angle θ, a torque τ acts on the sample and deflects the paddle from its zero field position. (b) Side-view of the MCM.

A sketch of the micromechanical cantilever magnetometer (MCM) used in this work is depicted in Fig. 3.5 (a). The device was micro-

machined from bulk GaAs wafers with functional AlGaAs layers grown by MBE using the toolbox of micro-electromechanical system (MEMS) fabrication. A detailed description of the preparation process can be found, e.g., in Ref. [Cha12]. The MCM consisted of a flexible beam and a paddle of size $(2.0 \times 1.2)\,\mathrm{mm}^2$ to attach the sample on top. The thickness of the beam was as small as $\approx 4\,\mu\mathrm{m}$, accounting for small spring constants, enabling high mechanical sensitivity towards an external force or torque.

The magnetization caused by the orbital motion of the electrons in an ideal 2DES is perpendicular to the sample surface. If a magnetic field $\mathbf{B}$ is applied at an angle θ with respect to the surface normal of the sample, a torque

$$\boldsymbol{\tau} = \mathbf{M} \times \mathbf{B} \tag{3.1}$$

will act on the cantilever and deflect the paddle from its zero-field position. This deflection can be detected via capacitive or optical methods and calibrated against a known force or torque as discussed below. In the present setup, the in-plane direction of $\mathbf{B}$ was chosen to be parallel to the cantilever beam to avoid a torsional twist of the paddle and to address the longitudinal bending component only. With this particular configuration, Eq. (3.1) can be expressed in terms of absolute values of the respective vectors as $\tau = MB\sin\theta$. By knowing the torque τ, the magnetization M is thus obtained via

$$M = \frac{\tau}{B\sin\theta}\ . \tag{3.2}$$

Equation (3.2) implies that for a constant sensitivity of the device in terms of the torque $\Delta\tau$, the sensitivity in the magnetization ΔM increases linearly with increasing magnetic field B. Furthermore, and recapitulating that the dHvA-effect in 2DES is mainly governed by the perpendicular field component $B_\perp$, we find that ΔM for a certain $B_\perp = B\cos\theta$ increases with $\sin\theta/\cos\theta = \tan\theta$.

3.2.2 Capacitive readout

A straightforward way to address cantilever deflection is via a capacitive readout scheme as used in Refs. [CCN92; Sch+00]. For the MCMs used in this work, this technique allowed for a sensitivity in M on the order

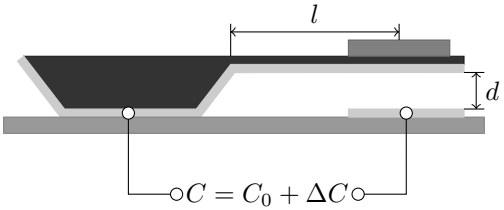

Figure 3.6: Capacitive readout scheme of the MCM. The metalized backside of the cantilever and a fixed counter electrode with area A_C form a capacitor with $C = \epsilon_0 A_C/d$. The capacitance change due to a deflection Δd of the cantilever paddle is measured with a capacitance bridge.

of $\Delta M \approx 5 \times 10^{-15}\,\mathrm{J/T}$ at $B = 10\,\mathrm{T}$ and $\theta = 15°$ [Sch+02a], limited by electrical and mechanical noise. Cantilevers used for capacitive readout featured a metalized backside and were glued onto a sapphire substrate with a fixed counter electrode, as depicted in Fig. 3.6. The capacitance $C = \epsilon_0 A_C/d$ between the paddle and the counter electrode depends on the distance d between the two plates (A_C is the effective area of the capacitor). We measured C by means of a capacitance bridge[1]. For small changes Δd, we can approximate the change in capacitance ΔC via the linear relation

$$\Delta C \approx \frac{C_0}{d}\Delta d, \tag{3.3}$$

where C_0 is the capacitance at zero torque. Furthermore, Hooke's law holds true in the regime of small Δd, which results a linear dependence between τ and Δd. Taken together, we obtain

$$\tau = K_C \Delta C\ , \tag{3.4}$$

where K_C is the calibration constant for capacitive readout. Following Ref. [Wil04], calibration of the setup was performed by applying an additional DC voltage between the two capacitor plates, which results in a well-defined force that pulls the paddle towards the counter electrode.

[1] Andeen Hagerling 2500 A / 2700 A

We recorded $\Delta C(U_C)$ and fitted the resulting curve via $\Delta C = \kappa_U U_C^2$. The calibration constant K_C was then obtained via

$$K_C = \frac{\beta C_0^2 l}{2\epsilon_0 A_C \kappa_U} \ . \tag{3.5}$$

Here, $\beta = 0.73$ is a correction factor that accounts for differences in the deflection due to a force or a torque [Wil04] and $l = 1.6\,\mathrm{mm}$ is the distance between the suspension point of the beam and the center of the paddle.

3.2.3 Interferometric readout

The capacitive readout scheme is straightforward but has some limitations. First, the readout via the capacitance bridge is relatively slow, and fast motions of the cantilever are difficult to monitor with this technique. Second, the investigation of electrically contacted samples featuring gate electrodes is hindered by crosstalk effects. Therefore, Springborn *et. al.* introduced an alternative readout technique based on a fiber optic interferometer integrated into ^{3}He-systems used for experiments in this work [Spr+06]. This method guaranteed a fast monitoring of the cantilever deflection and enabled an enhancement of resolution in M by a factor of ≈ 10 as opposed to the capacitive readout scheme. Furthermore, gate-controlled magnetization and magnetotransport experiments could be performed simultaneously during the same cool-down process [Ruh+06].

For this purpose, the design of the MCM was slightly altered, as sketched in Fig. 3.7 (a). Dedicated cantilevers featured a reflective Au pad forming one mirror of the interferometer. Furthermore, evaporated Au leads were integrated to address sample contacts and gate as well as a thin film single turn coil used for calibration and active damping. Flip-chip samples (c.f. section 3.1.1) were mounted upside-down on the paddle using a conductive epoxy bonding technique. An optical microscope image of the setup showing cantilever and optical fiber is depicted in Fig. 3.7 (b).

In the following, we briefly explain the interferometric readout process. For a more detailed description we refer to Ref. [Spr07]. A sketch of the readout scheme is presented in Fig. 3.8. Laser light ($\lambda = 1310\,\mathrm{nm}$)

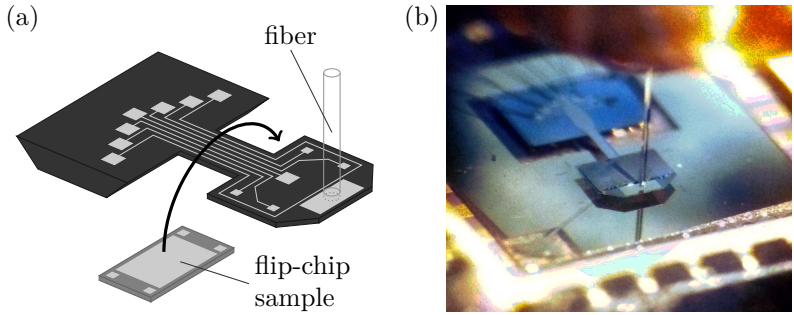

Figure 3.7: (a) Sketch of MCM design for interferometric readout. The cleaved edge of an optical fiber and an Au reflective pad on top of the cantilever paddle formed a Fabry-Perot interferometer. The readout procedure is illustrated in detail in Fig. 3.8. The MCM featured Au leads to address electrical contacts of dedicated flip chip samples as well as a thin film coil. (b) Optical microscope image of the setup with attached flip-chip sample and optical fiber.

was coupled into a single-mode optical fiber. Via a beam splitter, 10 % of the light was guided to the cantilever that was mounted inside a ^{3}He cryostat. An acusto-optical modulator (AOM) was used to adjust the laser power. The Au reflective pad on the cantilever paddle and the cleaved edge of the fiber formed a Fabry-Perot interferometer (blow-up in Fig. 3.8). The reflected light was detected with a photo diode. The photo voltage exhibited a characteristic interference pattern $U_{\mathrm{PD}}(d)$, as depicted in the inset in Fig. 3.8. We measured the deflection of the cantilever by adjusting the vertical fiber position with a piezoceramic tube in order to keep the distance d constant. This was achieved via a closed feedback loop with the point of operation chosen to be one of the inflection points of the interference pattern [marked with a dot in the inset of Fig. 3.8 (b)]. Low-pass filtering (LPF) was used to average over fast vibrations of the cantilever.

The voltage U_{piezo} at the piezo-electric tube was proportional to the quasi-static cantilever deflection and provided the raw measurement signal. A second feedback loop was used for active damping of fast oscillations of the cantilever via the thin-film coil. The damping mechanism

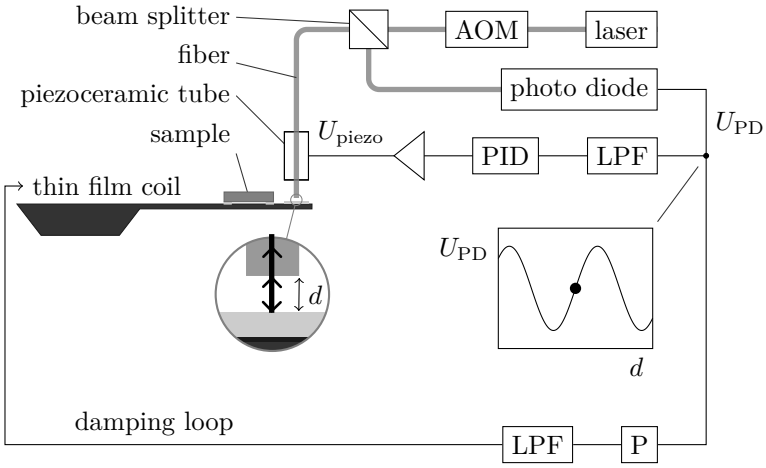

Figure 3.8: Schematic of the interferometric readout process. The cleaved edge of the optical fiber and the mirror plate on top of the cantilever formed a Fabry-Perot interferometer (see blow-up). The interference pattern (see inset) was detected with a photo diode. By means of a piezoceramic tube, the distance between fiber and cantilever was held constant via a closed feedback loop using a PID controller. The piezo voltage U_{piezo} was used to measure the deflection. In a second feedback loop, fast motions of the paddle were damped via the integrated thin film coil.

is explained in detail in section 4.2.2. With this setup, deflections of the cantilever < 1Å could be detected, which allowed for a resolution of order $\Delta M \approx 5 \times 10^{-16}\,\mathrm{J/T}$ at $B = 10\,\mathrm{T}$ and $\theta = 15°$.

The torque τ is expressed as

$$\tau = K_I U_{\mathrm{piezo}} \ , \tag{3.6}$$

where K_I is the calibration constant for interferometric readout. Absolute calibration was performed by passing a DC current I through the thin film coil, thereby evoking a well-defined magnetic moment $M = I\,A_{\mathrm{coil}}$ (A_{coil} is the area surrounded by the coil). We measured

U_{piezo} as a function of I and extracted the slope $\kappa_I = dI/dU_{\text{piezo}}$. Following [Spr07], K_I was then obtained via

$$K_I = \kappa_I A_{\text{coil}} B \sin\theta \ . \tag{3.7}$$

We notice that K_I was independent on the applied laser power as well as the configuration parameters of the feedback loop, because U_{piezo} directly translated into a deflection $\Delta d' = 1.7\,\text{nm/V} \cdot U_{\text{piezo}}$.

3.3 Magnetotransport measurements

Transport experiments are most commonly used to study quantum oscillatory behavior of 2DESs in high magnetic fields and cryogenic temperatures because they are straightforward to implement and do not require involved experimental techniques as needed to measure thermodynamic quantities. The transport of charge in response to an electric field depends, among others, on the number of free states in the vicinity of the Fermi level E_{F} and thus on the density of states. As explained in 2.2, E_{F} passes through Landau levels with enhanced DOS as the magnetic field B increases, which modifies the longitudinal resistivity ρ_{xx}. ρ_{xx} performs $1/B_\perp$-periodic oscillations, which are also known as Shubnikov-de Haas (SdH) oscillations [SH30]. Qualitatively, these oscillations also reveal SOI effects in form of beating patterns and exhibit the same node positions as M or μ.

In a diffusion picture by Ando and Uemura, the conductivity σ_{xx} of a 2DES at applied field $B_\perp$ and $T = 0$ is predicted to be proportional to the DOS at the Fermi energy [AU74]

$$\sigma_{xx} = e^2 D(E_{\text{F}}) D^* \tag{3.8}$$

with a diffusion constant $D^* \sim (2n+1) l_B^2/\tau'$ (τ' is the electron lifetime and n is the LL index at the Fermi level). Equation (3.8) is valid if the LLs do not overlap (i.e. the level broadening Γ is much smaller than $\hbar\omega_c$). In this case, $D(E_{\text{F}}) \propto \exp\left[-(E_{\text{F}} - E_n)^2/\Gamma^2\right]$. If $\Gamma \gtrsim \hbar\omega_c$, a

summation over n has to be performed. Moreover, if spin splitting is included, σ_{xx} can be modeled via [Eng+82]

$$\sigma_{xx} \propto \sum_{n,\pm} \left(n + \frac{1}{2} \right) \exp - \frac{(E_\mathrm{F} - E_{n,\pm})^2}{\Gamma^2} \ . \tag{3.9}$$

Here, $E_{n,\pm}$ are energies of the spin-split LLs. If the magnetic field is sufficiently large, we can use

$$\rho_{xx} = \frac{\sigma_{xx}}{(\sigma_{xx}^2 + \sigma_{xy}^2)} \approx \sigma_{xx} \left(\frac{B_\perp}{e\, n_\mathrm{2D}} \right)^2 , \tag{3.10}$$

i.e., oscillations in σ_{xx} are directly reflected in the longitudinal resistance ρ_{xx}. The above models predict that minima of $\rho_{xx}(B_\perp)$ occur at $B_\perp$ where E_F resides in between two neighboring levels of the energy spectrum $E_{n'}$ and thus can be identified with integer values of the filling factor ν.

Neglecting quantization effects, the transverse resistance ρ_{xy} of a 2DES yields [YC13]

$$\rho_{xy} = -\frac{B_\perp}{e\, n_\mathrm{2D}} \ . \tag{3.11}$$

This is the famous classical Hall effect [Hal79] which allows to extract the sheet electron density n_2D from the slope of ρ_{xy} measured as a function of $B_\perp = B \cos\theta$. Consequently, the classical Hall measurement is suitable to accurately determine the tilt angle θ of the sample once n_2D is known. At high magnetic fields, also ρ_{xy} of a 2DES can exhibit signatures of Landau quantization in form of quantum Hall plateaus [KDP80]. However, these effects were not addressed in the current work.

Using the Hall bar samples introduced in 3.1.2, ρ_{xx} and ρ_{xy} were determined by injecting a current I of order 10 - 100 nA between contacts 1 and 5 and simultaneously measuring the voltage drop U_{xx} between contacts 2 and 4 as well as U_{xy} between contacts 3 and 7 (c.f. Fig. 3.9). These measurements were performed using standard low-frequency lock-in technique. Here, we modulated the current with $f = 17.3\,\mathrm{Hz}$ and

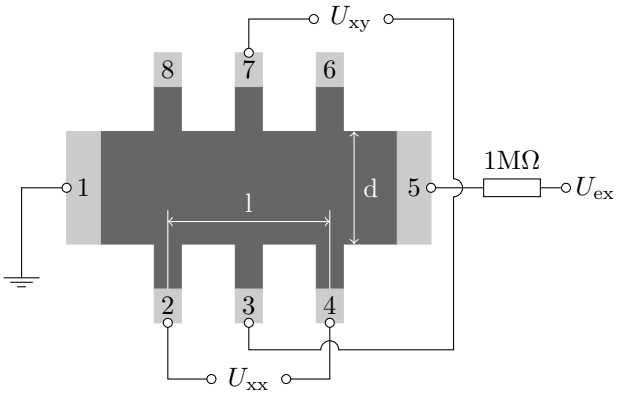

Figure 3.9: Connection scheme for simultaneous R_{xx} and R_{xy} measurements on Hall bar samples. An AC current was injected by applying an AC excitation voltage with amplitude U_{ex} over a resistance of 1.0 MΩ, while U_{xx} and U_{xy} were detected with two coupled lock-in amplifiers.

detected U_{xx} and U_{xy} using two coupled lock-in amplifiers. From the Hall bar geometry, we obtain

$$\rho_{xx} = \frac{E_x}{j_x} = \frac{U_{xx}d}{Il} = R_{xx}\frac{d}{l} \tag{3.12}$$

and

$$\rho_{xy} = \frac{E_y}{j_x} = \frac{U_{xy}}{I} = R_{xy} \tag{3.13}$$

with the current density $j_x = I/d$. When presenting experimental results, we will report on the measured resistances R_{xx} and R_{xy} instead of the resistivities ρ_{xx} and ρ_{xy}.

The flip-chip samples with four contacts at the corners in the so-called Van-der-Pauw configuration enabled to measure only one of the two quantities at the same time. Here, R_{xx} was determined by injecting a current between contacts 1 and 2 and measuring U_{xx} between 3 and 4 [see Fig. 3.10 (a)]. Despite from the rectangular geometry, R_{xx} was proportional to ρ_{xx} because no net current passed between contacts 3

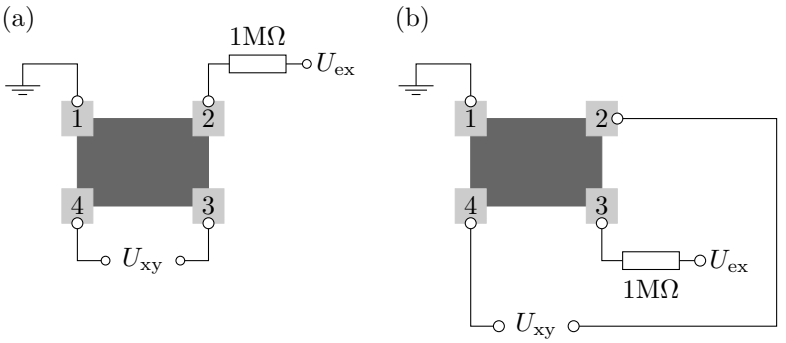

Figure 3.10: Connection scheme for magnetotransport on rectangular flip-chip samples. Here, (a) R_{xx} and (b) R_{xy} had to be measured in separate configurations.

and 4, and thus no Hall signal caused by ρ_{xy} was superimposed to R_{xx} [Pau58]. For determining R_{xy}, we injected I between contacts 1 and 3 and measured the voltage drop U_{xy} between 2 and 4 [see Fig. 3.10 (b)]. This signal, however, was a superposition between longitudinal and Hall voltages [Pau58]. In order to extract the Hall resistance only, we performed measurements at positive and negative $B_\perp$ and subtracted the two signals:

$$R_{xy} = \frac{1}{2}\frac{U_{xy}(B_\perp) - U_{xy}(-B_\perp)}{I} \tag{3.14}$$

This removed the longitudinal contribution which was independent on the sign of $B_\perp$ while keeping the transverse contribution with odd parity in $B_\perp$.

4 Advancements of the cantilever magnetometer setup

In this chapter, we report on new developments of the cantilever magnetometer setup with interferometric readout (c.f. section 3.2) that were elaborated in the course of this thesis. These advancements substantially increased the performance of the device and led to a better understanding of the device characteristics. First, we were able to measure the electron temperature T of the flip chip sample directly as a function of the applied laser power, clarifying that T was significantly increased compared to the temperature of the sample stage. We improved the readout procedure using lock-in technique, allowing for a substantial reduction of the required laser power and enabling sample temperatures in the mK range. Second, we report on a new method to simultaneously measure the magnetization M and the chemical potential μ of a 2DES via a combined static operation and resonant excitation of the MCM. While the feasibility of this technique was already demonstrated by Ruhe and Stracke [Ruh08; Str08], we combined the technique with the improved interferometric readout procedure and found that the resonant excitation significantly increased the sensitivity of the MCM by about one order of magnitude. Finally, we analyzed mechanical resonance curves of the MCM, demonstrating that the Q-factor and hence the mechanical response of the MCM to a resonant excitation can be tuned by modifying the parameters of the active damping loop.

4.1 Power-modulated interferometric readout scheme

The fiber-optics interferometer described in 3.2.3 was usually operated at a laser power of $P \approx 10\,\mu$W leaving the fiber edge above the cantilever paddle. At cryogenic temperatures in the mK range, however, such a power was sufficient to increase the electron temperature T of the sample. For the present InGaAs/InP flip chip samples, we could measure $T(P)$ via the amplitudes of Shubnikov-de Haas (SdH) oscillations as determined from magnetotransport, i.e., the sample itself served as a temperature sensor.

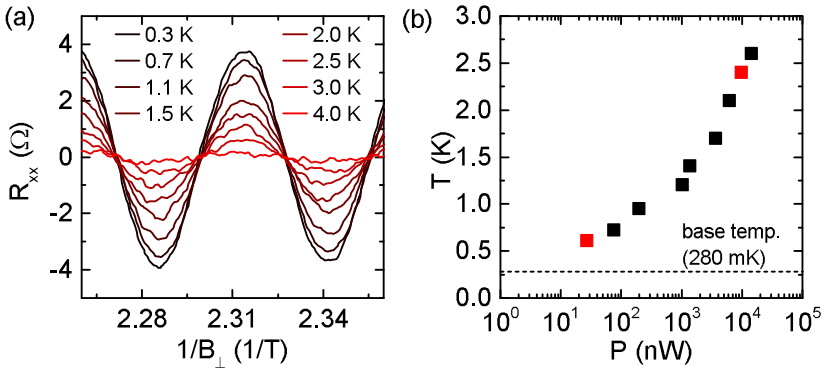

Figure 4.1: (a) Magnetotransport data $R_{xx}(1/B_\perp)$ of sample #4069-5B measured at different temperatures T with the laser switched off. The amplitudes of the SdH-oscillations were used to calibrate the sample temperature. (b) Sample temperature as a function of laser power P based on the calibration shown in (a). Here, the temperature of the sample stage was $T_{\mathrm{stage}} = 280\,$mK. The red data points mark the measurement conditions before ($P = 20\,\mu$W) and after improvement of the setup ($P = 20\,$nW).

To determine $T(P)$, we first switched off the laser and calibrated the SdH amplitudes against a temperature sensor mounted on the sample stage next to the cantilever. The recorded R_{xx} oscillations as a function of $1/B_\perp$ for different T are shown in Fig. 4.1 (a). Next, we returned to base temperature and recorded $R_{xx}(1/B_\perp)$ again for different laser powers P, and extracted the respective sample temperatures from the

previous calibration. The resulting $T(P)$ is plotted in Fig. 4.1 (b). With a laser power of $P \approx 10\,\mu$W, we found a sample temperature of $\approx 2.5\,$K as compared to $T_{\text{stage}} = 280\,$mK at the sample stage. We attributed this behavior to the small heat conductivity of the thin cantilever beam, which hindered the effective dissipation of heat away from the paddle.

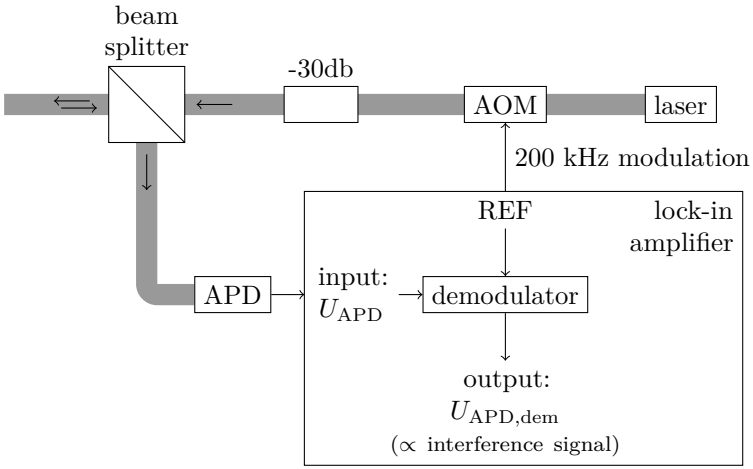

Figure 4.2: Schematic of the technique to measure the interference pattern with lock-in technique. Via the acusto-optical modulator (AOM), the laser power was modulated with a frequency of 200 kHz. The optical response of the interferometer was detected with a low-noise avalanche photo diode (APD) and demodulated in a phase-locked loop using a lock-in amplifier. The output signal $U_{\text{APD,dem}}$ was proportional to the interference pattern.

It is clear from the data in Fig. 4.1 (b) that only a substantial reduction of P enabled temperatures in the mK range, which, however, were crucial for the detection of SOI-related beating patterns in the dHvA oscillations. Since such a decrease of P was not possible using the original setup, we developed an improved version of the readout scheme optimized for small laser powers. A schematic of the modified parts of the setup is depicted in Fig. 4.2. For an effective filtering of broadband noise, we modulated the laser power with 200 kHz via the AOM, and demodulated the response signal using a lock-in amplifier.

We replaced the original photo diode by an avalanche photo diode (APD) with increased sensitivity for small light intensities. The demodulated signal was finally converted to an output voltage $U_{\mathrm{APD,dem}}$. Integration with a time constant of 100 μs still allowed to detect vibrations of the cantilever paddle on the order of 100 Hz. In that sense, $U_{\mathrm{APD,dem}}(d)$ exhibited the same interference pattern as measured directly by the photo voltage $U_{\mathrm{PD}}(d)$ in the previous setup with constant laser power.

With this modification of the setup, a reduction of P by more than a factor of 1000 still allowed to detect the deflection of the cantilever with high sensitivity, while simultaneously facilitating sample temperatures in the mK range. Figure 4.3 shows recorded magnetization curves of an InGaAs flip-chip sample for different P, ranging from 2.5 nW up to 60 nW. While no significant loss in sensitivity was asserted above 20 nW, the signal-to-noise ratio in M started to degrade as soon as $P < 20$ nW. For the measurements performed on InGaAs/InP flip-chip samples we used $P = 20$ nW in order to account for maximum sensitivity at a sample temperature of $T = 600$ mK.

4.2 Dynamic magnetization and chemical potential

In this section, we present an advancement of the MCM setup that allowed us to measure both the magnetization M and the chemical potential μ of a 2DES, which was based on a combined static operation and resonant excitation of the cantilever paddle. There are previous works which used resonant driven MCMs to determine M with enhanced sensitivity [Har+99; BSH08; Jan+11; JBM11]. The authors used a piezo-driven stage to mechanically excite the cantilevers, and measured the changes in resonance frequency or phase induced by the magnetization of the sample.

Here, we present a different approach which was first employed by Ruhe and Stracke [Ruh08; Str08] and further improved within the course of this thesis. Complementary to the techniques used in the works cited above, we excited the cantilever by a modulation of the sample magnetization M itself via an oscillating gate voltage. This allowed us to measure the derivative of M with respect to the number of electrons $\partial M/\partial N$ as a function of B. Via the Maxwell relation

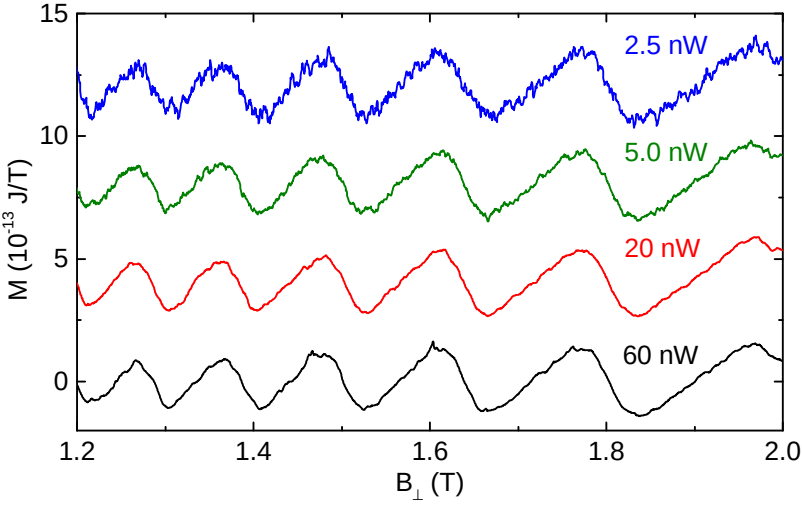

Figure 4.3: Magnetization $M(B_\perp)$ measured for an InGaAs/InP flip-chip sample (#4069-5C) using the improved interferometric setup with 200 kHz power modulation. Four curves were measured with different average laser power P to illustrate the power-dependent signal-to-noise ratio in M.

$(\partial M/\partial N)_{T,B_\perp} = (\partial \mu/\partial B_\perp)_{T,N}$, direct access to the chemical potential μ was obtained by evaluating

$$\mu = -\int \left(\frac{\partial M}{\partial N}\right)_{T,B_\perp} dB_\perp. \tag{4.1}$$

In the following, we describe the dynamic measurement technique in detail and outline the modifications to the calibration procedure needed to determine $\partial M/\partial N$. Subsequently, we discuss the impact of the active damping loop on the mechanical properties of the cantilever and implications for the dynamic calibration process.

4.2.1 Experimental setup

We modulated the gate voltage of the flip-chip sample $U_\mathrm{g} = \delta U_\mathrm{g} \sin \omega t$ with amplitude δU_g and frequency $f = \omega/(2\pi)$. This caused an in-

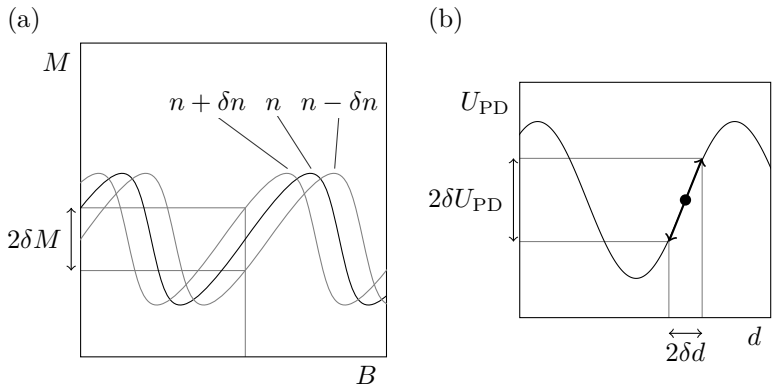

Figure 4.4: (a) Illustration of $M(B)$ for different $n_{2\mathrm{D}}$. If $n_{2\mathrm{D}}$ is modulated with amplitude $\delta n_{2\mathrm{D}}$ at constant B, this results in a modulation of M with amplitude proportional to $\partial M/\partial N$ and hence to a vibration of the cantilever paddle. (b) For small vibration amplitudes δd, the dynamic response δU_{PD} in the interference is linear. Here, the quasi-static feedback loop accounted for operation at the inflection point of the interference pattern.

stantaneous modulation of the electron density at the same frequency and with amplitude $\delta n_{2\mathrm{D}} = (\partial n_{2\mathrm{D}}/\partial U_{\mathrm{g}})\delta U_{\mathrm{g}}$. Here, the transfer function $\partial n_{2\mathrm{D}}/\partial U_{\mathrm{g}}$ was determined in a separate experiment. Further, the modulation of $n_{2\mathrm{D}}$ directly resulted in a modulation of the 2DES magnetization M with amplitude

$$\delta M = \frac{\partial M}{\partial N}\delta N = \frac{\partial M}{\partial N} A_{\mathrm{m}} \delta n_{2\mathrm{D}} \tag{4.2}$$

with the total number of electrons $N = n_{2\mathrm{D}} A_{\mathrm{m}}$ and the 2DES mesa area A_{m}. This is illustrated schematically in Fig. 4.4 (a). The change of $n_{2\mathrm{D}}$ altered the curve $M(B)$. At a fixed value of B, small changes of N thus provoked changes in M proportional to $\partial M/\partial N$. The modulation of M led to a modulation of the torque with amplitude $\delta\tau = \delta M/(B\sin\theta)$, which in turn caused a mechanical vibration of the cantilever paddle with amplitude δd. The modulation frequency f was chosen slightly smaller than the cantilever resonance frequency f_0 on the order of $\approx 100\,\mathrm{Hz}$

to account for an increased mechanical response. Larger values of f led to instabilities in the readout process. Low-pass filtering was used to decouple the quasi-static feedback loop from the fast vibration of the paddle and enabled the simultaneous detection of M. Thereby, the (quasi-static) operation point of the interferometer was held at the inflection point of the interference pattern. Consequently, small deviations in the cantilever deflection δd resulted in a linear response of the interference signal, as sketched in Fig. 4.4 (b). Using standard lock-in technique, we measured δd via the amplitude of the oscillating photo voltage δU_{PD}.

In order to account for small laser powers and low sample temperatures, we combined power modulation with 200 kHz and gate modulation with $\approx 100\,\mathrm{Hz}$ via a tandem demodulation of the APD signal using one-and-the-same lock-in amplifier. This was possible due to the different time scales defined by the two reference signals. Here, internal digital signal processing improved the signal-to-noise ratio as opposed to a measurement with two separate lock-in amplifiers. Therefore, in the dynamic readout, we effectively measured the amplitude of the demodulated APD signal, $\delta U_{\mathrm{APD,dem}}$.

Calibration of the dynamic setup was quite similar to quasi-static calibration. The linearity of the dynamic response connects the amplitudes

$$\delta\tau = K_{\mathrm{dyn}}(B)\delta U_{\mathrm{APD,dem}} \ . \tag{4.3}$$

Here, the dynamic calibration constant $K_{\mathrm{dyn}}(B)$ had to be determined as a function of B, because field-dependent forces provoked by active and passive damping or the sample's magnetization itself influenced the mechanical resonance curve of the cantilever. Knowing $K_{\mathrm{dyn}}(B)$, $\partial M/\partial N$ was obtained by evaluating

$$\frac{\partial M}{\partial N} \approx \frac{\delta M}{\delta n_{\mathrm{2D}} A_{\mathrm{m}}} = \frac{K_{\mathrm{dyn}}(B)}{B \sin\theta\, A_{\mathrm{m}}\, (\partial n_{\mathrm{2D}}/\partial U_{\mathrm{g}})} \cdot \frac{\delta U_{\mathrm{APD,dem}}}{\delta U_{\mathrm{g}}} \ . \tag{4.4}$$

For absolute calibration an AC current $I = \delta I \sin\omega t$ was passed through the thin-film coil, thereby recording $\delta U_{\mathrm{APD,dem}}(B)$. K_{dyn} was then obtained as

$$K_{\mathrm{dyn}}(B) = \frac{\delta\tau}{\delta U_{\mathrm{APD,dem}}} = \frac{\delta I_{\mathrm{coil}} A_{\mathrm{coil}} B \sin\theta}{\delta U_{\mathrm{APD,dem}}} \ . \tag{4.5}$$

We stress that the calibration was carried out under exactly the same conditions as the actual measurement, i.e., at equal parameters of static feedback and active damping loop, tilt angle θ and distance fiber - cantilever. Different from static calibration, K_{dyn} sensitively depended on each of those parameters. Figure 4.5 (a) and (b) exemplarily show $U_{\mathrm{APD,dem}}(B_\perp)$ and $K_{\mathrm{dyn}}(B_\perp)$, respectively, measured for sample #4069-5B at $\theta = 15°$ and using $\delta I_{\mathrm{coil}} = 4\,\mathrm{nA}$. We observed that $K_{\mathrm{dyn}}(B)$ was not a constant, but depended on the magnetic field B. Interestingly, the dHvA-oscillations of the sample at larger fields were reflected in $K_{\mathrm{dyn}}(B)$. We attributed this to a change in the mechanical resonance frequency f_0 evoked by the sample magnetization M.

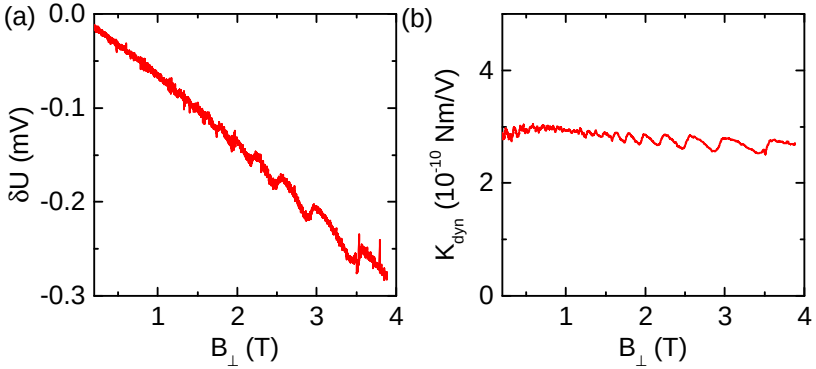

Figure 4.5: (a) Raw calibration data $\delta U_{\mathrm{APD,dem}}(B_\perp)$ of sensor #1236-1 with sample #4069-5B. Parameters were $\delta I = 4\,\mathrm{nA}$ and $\theta = 15°$. (b) Calculated calibration constant $K_{\mathrm{dyn}}(B_\perp)$.

4.2.2 Resonance curves and active damping

In this section, we discuss mechanical resonance curves of the cantilever. First, we review the model of a driven harmonic oscillator and show how active damping via a closed feedback loop can be integrated into the modeling, thereby virtually modifying the mechanical properties of the cantilever. Second, we present experimental resonance curves, demonstrate the validity of our modeling, discuss the impact on K_{dyn}

and extract quantitatively the enhanced mechanical response for the dynamic measurement.

In the regime of small deflections where Hooke's law holds true, the cantilever can be described as a damped harmonic oscillator with resonance frequency ω_0 and damping parameter γ. Let us define by u a dimensionless measure of the cantilever deflection. If the oscillator is driven by an external force at frequency $f = \omega/(2\pi)$, the equation of motion is

$$\ddot{u} + \gamma\dot{u} + \omega_0^2 u = \delta C \sin\omega t \ . \tag{4.6}$$

Here, δC is proportional to the amplitude of external excitation, and $\delta C/2\omega_0$ denotes the quasi-static deflection (at $\omega = 0$). The oscillation amplitude δu as a function of ω is derived as [GM03]

$$\delta u = \frac{\delta C}{\sqrt{(\omega_0^2 - \omega^2) + (\gamma\omega)^2}} \ . \tag{4.7}$$

Active damping of the cantilever was performed by taking the deflection signal of the interferometer ($\propto u$), passing it through an amplifier with adjustable gain p and a low-pass filter. Finally, the signal was fed into the thin-film coil, thereby provoking an additional torque acting on the cantilever. Here, the characteristics of the filter produced a phase shift $-\delta\phi$ of the input signal, i.e., the response signal of the damping loop was delayed with respect to the original deflection. This is illustrated in Fig. 4.6 (a). We note that $\delta\phi$ could be tuned by tuning the cut-off frequency of the filter. The response signal can be decomposed into a contribution proportional to the deflection u itself ($\propto \sin\omega t$) and a contribution $\propto \cos\omega t$, i.e., effectively proportional to $\dot{u}$ [see Fig. 4.7 (b)]. These contributions enter the equation of motion

$$\ddot{u} + \gamma\dot{u} + \omega_0^2 u \ = \ \underbrace{\delta C \sin\omega t}_{\text{excitation}} \ + \ \underbrace{(D\,p\,\cos\Delta\phi)\cdot u - (D\,p\,\sin\Delta\phi)\cdot\dot{u}}_{\text{active damping}} \ . \tag{4.8}$$

Here, D is a combined proportionality constant that contains the B- and θ-dependence of the torque induced by the thin film coil and the overall gain of the feedback loop. It is easy to see that the two introduced

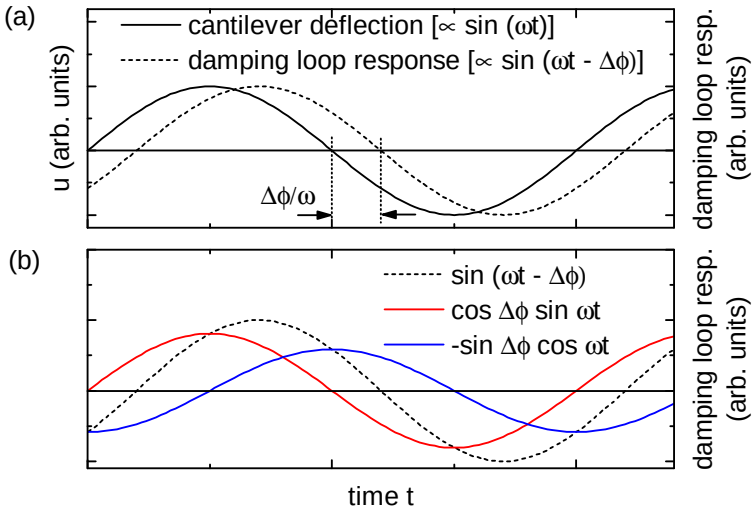

Figure 4.6: (a) Deflection $u(t)$ of excited cantilever at frequency ω (solid line, $\propto \sin \omega t$). The response of the active damping loop (dashed line) was delayed by a phase difference $\Delta\phi$ ($\propto \sin(\omega t - \Delta\phi)$). (b) Decomposition of the damping loop response into two signals $\propto \sin \omega t$ (in phase, red) and $\propto \cos \omega t$ (phase-shifted by $\pi/2$, blue). While the former is proportional to u, the latter is effectively proportional to $\dot{u}$.

terms lead to a virtual modification of the mechanical parameters ω_0 and γ of the form

$$\begin{aligned} \omega_0' &\to \sqrt{\omega_0^2 - Dp \cos \Delta\phi} \\ \gamma' &\to \gamma + Dp \sin \Delta\phi \ . \end{aligned} \tag{4.9}$$

We stress that both p and $\Delta\phi$ can be tuned, which enables a tuning of f_0 and γ and thus also an adjustment of the Q-factor of the cantilever.

Experimentally recorded resonance curves $\delta u(f)$ for three different values of p are plotted in Fig. 4.7. Here, we excited the cantilever with an AC current at frequency f through the coil and measured $\delta U_{\mathrm{APD,dem}}$ as a function of f. The active damping loop was operated simultaneously. The resonance curves were measured at constant B and θ. We observed a shift of f_0 to lower f and an increase of γ as

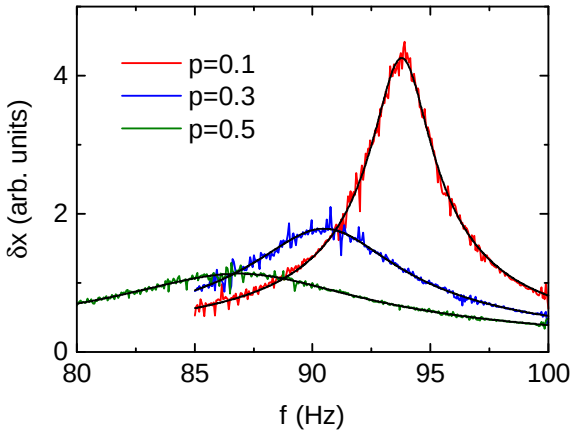

Figure 4.7: Experimental resonance curves $\delta u(f)$ measured for cantilever #1236-1 for different values of the proportional gain p of the active damping loop (colored curves). The data were recorded at $B = 4\,\mathrm{T}$ and $\theta = 15°$. The black curves show respective fits by the model of a driven and damped harmonic oscillator $\delta u = \delta C/\sqrt{(\omega_0^2 - \omega^2) + (\gamma\omega)^2}$. Extracted fit parameters $f_0 = 2\pi\omega_0$, γ and δC are summarized in Tab. 4.1.

p increased, which is in accordance with Eq. (4.9). Furthermore, we fitted the curves by Eq. (4.6) with free parameters f_0, γ and δC, which are summarized in Tab. 4.1. We found that the experimental curves were represented quantitatively by the modeling, which underlines that the system can indeed be described as a harmonic oscillator, also with activated damping loop. As a consequence, the linear relation $\delta\tau = K_{\mathrm{dyn}}\delta U_{\mathrm{APD,dem}}$ still holds and calibration of the setup based on this relation is justified. Furthermore, the extracted fit parameters f_0 and γ approximately follow the theoretical relations of Eq. (4.9) as a function of p. Similar dependencies were asserted as a function of B or θ (not shown). This demonstrates the validity of the above modeling and proves that the resonance curve, and thus the calibration constant K_{dyn}, sensitively depended on these parameters. For absolute calibration, it was therefore indispensable to record $K_{\mathrm{dyn}}(B)$ under exactly the same conditions as the actual measurement.

Independent on the parameters f_0 and γ, we extracted a static deflection $\delta u_{\mathrm{stat}} = \delta C/\omega_0^2 \approx 0.1$. If we compare this value to the amplitudes at resonance condition, we find that an enhancement of the mechanical response by more than a factor of 40 is possible with the used cantilevers. For measurements presented in this thesis, we used $p = 0.1$ and $f = 92\,\mathrm{Hz}$, giving an increase by a factor of ≈ 15, which was already large enough for a substantial sensitivity enhancement of the dynamic measurement.

Table 4.1: Parameters $f_0 = \omega_0/(2\pi)$, γ and $\delta C/\omega_0^2$ extracted from fits of Eq. (4.7) to experimental resonance curves plotted in Fig. 4.7 for different values of the proportional gain p of the active damping loop.

p (arb. units)	f_0 (Hz)	γ (**1/s**)	$\delta C/\omega_0^2$ (arb. units)
0.1	93.79	3.96	0.11
0.3	90.58	9.64	0.12
0.5	87.18	16.24	0.12

5 Magnetization and chemical potential of a 2DES with spin-orbit interaction

In this chapter we present measurements of the magnetization M and the chemical potential μ on gated InGaAs/InP 2DESs that are subject to spin-orbit interaction. As explained in detail in chapter 2, these thermodynamic functions of state provide access to the electronic ground state. In particular, the presence of SOI provokes a modification of the Landau level structure which is directly reflected in the magneto-oscillations of M and μ via beating patterns. The experimental traces of these quantities as a function of field can be directly simulated from theoretical energy spectra without further microscopic assumptions. Hence, M and μ are powerful to verify the validity of theoretical models describing the electronic structure of 2DESs.

Extensive investigations on magnetization M and chemical potential μ in the presence of SOI in a 2DES and related quantum structures can not be found in the literature. This is because investigations of SOI-related beating patterns in M are challenging due to the inherently small sensitivity of torque magnetometry at small B (c.f. section 3.2). Recent works include measurements on AlGaAs-based heterostructures, where it was possible to detect a single beat node only at high tilt angles θ [Wil+09]. Using the same InGaAs/InP heterostructure as investigated in the present work, Rupprecht *et. al.* observed a beat node in the quantum oscillatory M at low tilt angles [Rup+13], which was attributed to a dominant Rashba SOI. Furthermore, they found anomalies in frequency and shape of the dHvA-oscillations, which are still unexplained to date.

Although magneto-oscillations in the chemical potential μ have been reported in separate experiments, signatures of SOI have, to the best

of our knowledge, not been addressed so far. Most recent studies focused on the steep jumps in μ that occur in a quantum Hall state of 2DESs. These investigations reported on Wigner crystal formation in bilayered 2DES [Zha+14] and quantum Hall ferromagnetism in bilayer graphene [Kim+12; Lee+14]. However, the detection of μ required rather involved techniques, including nanostructured single electron transistors [Wei+97], magnetocapacitance measurements [Dol+97] or electrometry on dedicated heterostructures, where complicated field-dependent re-tuning of gate voltages was needed [EPW94; Ho+10].

Here, we show that M and μ can be measured simultaneously via the novel micromechanical approach introduced in chapter 4. Using dedicated micromechanical cantilevers, access to M and μ was gained via a decoupled quasi-static operation and resonant excitation in response to a modulation of a gate voltage. Thus, the presented technique is straightforward to address the thermodynamic ground state in the sense that any gateable 2D system can be investigated. For the present InGaAs 2DES, we observed only a single beat node in the quantum oscillations of M, while an enhancement of resolution in μ enabled the detection of a second beat node. In a subsequent modeling of the curves, we show that, in addition to a dominant Rashba contribution, a small Dresselhaus term is required to describe the experimental data convincingly. This analysis goes beyond previous experimental investigations of SOI-related beatings [Luo+88; Das+89; Nit+97; Eng+97; Rup+13; Wil+14], where only the Rashba SOI mechanism was considered.

5.1 Experimental methods

Two flip-chip samples with four contacts and a gate electrode, denoted with #4069-5B and #4069-5C, were prepared from the same wafer as described in detail in 3.1.1. They were mounted and contacted upside-down on the paddle of dedicated GaAs cantilevers featuring Au leads to match the respective sample contacts. The cantilevers were placed on a fixed stage of a ^{3}He-cryostat with an integrated optical fiber, allowing for a base temperature of $T = 280\,\mathrm{mK}$ at zero laser power. To address static and dynamic deflection of the cantilever paddle, we used the improved optical readout technique as introduced in 4.1, where we modulated the laser power with 200 kHz. The average

power that left the optical fiber was 20 nW, thereby slightly increasing the sample temperature to $T = 0.6\,\mathrm{K}$. Besides the small heating effect, the laser did not influence the basic properties of the 2DES, as verified by magnetotransport measurements. Furthermore, illumination with a blue or an infrared LED did not have any effect on the electron density, as it was usually observed for un-gated samples (see [Rup+13] and chapter 6). The magnetic field was applied using a 2-axis vector magnet system with radial field strength of 4.5 T, with the field plane oriented parallel to the cantilever beam (see Fig. 5.1). The field was tilted towards the $[1\bar{1}0]$ direction of the sample, corresponding to a fixed in-plane angle of $\varphi = 135°$.

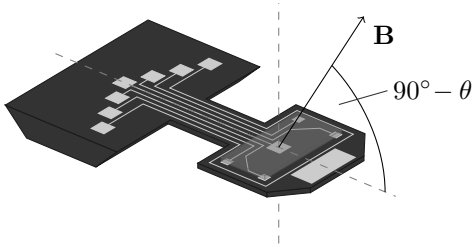

Figure 5.1: Sketch of the micromechanical cantilever magnetometer with the flip-chip sample placed on the cantilever paddle. The magnetic field **B** was applied with a 2-axis vector magnet system with the field plane parallel to the cantilever beam and the surface normal of the sample. The tilt angle θ was adjusted electronically.

The presented setup opens up the possibility to perform a variety of different experiments. These include measurements of magnetotransport, magnetization, magnetocapacitance and chemical potential, which can be recorded as a function of magnetic field, tilt angle and also electron density via the application of static gate voltages. In the following, we briefly summarize the experimental observations. First, we observed that in R_{xx}-measurements the SdH oscillations were superimposed by a strong background, i.e., in a quantum Hall state, the R_{xx} plateaus did not go to zero. Second, in simultaneous measurements of R_{xx} and M, we observed phase shifts of R_{xx} minima with respect to the steep dHvA flanks, which became more important for large filling factors and

increasing tilt angle. Nonetheless, we note that the $B_\perp$-positions of the dHvA flanks remained constant as a function of θ, while it was the R_{xx} minima that seemed to shift. The origin of this anomaly could not be clarified. We emphasize that the observed behavior differed from the findings of Rupprecht *et. al.*, where a slight jump of the frequency of the *magnetization* was asserted at the first beat node [Rup+13]. Third, experiments at high tilt angles revealed additional anomalies in the envelopes of both SdH and dHvA oscillations. Finally, we found that the application of static gate voltages produced drifts of the electron density on a relatively long timescale, therefore preventing measurements for different static gate voltages.

Considering these experimental findings, we will omit the discussion of the recorded R_{xx}-data and concentrate on measurements of M and μ which we performed at moderate tilt angles and at zero static gate voltage in the following. These were carried out with all four transport contacts connected to ground level, while the gate voltage was modulated with $\Delta U_\mathrm{g} = 5.6\,\mathrm{mV}$ at $f = 92\,\mathrm{Hz}$. The static and dynamic deflection of the cantilever were read out simultaneously as described in section 4.2. The experiments were performed with an activated damping loop to stabilize the cantilever motion in order to avoid a feedback loop lock-out. For each tilt angle θ, we averaged the data over four sweeps of B to effectively decrease statistical noise. Both samples #4069-5B and #4069-5C revealed consistent results. In the following, we present data of sample #4069-5B and report on extracted fitting parameters for both samples.

5.2 Experimental results

We divide the analysis of experimental data into four parts. First, we discuss the characteristics of the top gate and derive the transfer function $\partial n_\mathrm{2D}/\partial U_\mathrm{g}$ needed to calibrate the dynamic magnetization measurement. Second, we show and compare simultaneous measurements of M and $\partial M/\partial N$. Next, we derive the experimental chemical potential from the $\partial M/\partial N$ measurement and extract the SOI constants α_R and β_D from the experimental beat node positions. Finally, we calculate model curves for M and μ to fit the experimental data. For the theoretical analysis and simulation we use the model introduced in 2.4.

5.2.1 Gate characterization and transfer function

As explained in 4.2.1, the dynamic measurement of $\partial M/\partial N$ via a modulation of the top gate voltage U_g requires the knowledge of the transfer function $\partial n_{2D}/\partial U_g$ for absolute calibration. Using the transport contacts of the sample, we determined n_{2D} via a Hall measurement by evaluating $n_{2D} = B_\perp/(eR_{xy})$ as a function of U_g. Here, we applied a relatively small $B_\perp = 100\,\mathrm{mT}$ where $R_{xy}(B_\perp)$ did not exhibit plateaus. Figure 5.2 (a) shows $n_{2D}(U_g)$ for static gate voltages U_g. With the laser switched off, the electron system could successively be depleted by applying a negative U_g [black squares in Fig. 5.2 (a)]. A linear fit revealed $\partial n_{2D}/\partial U_g = 1.94 \times 10^{11}\,\mathrm{cm}^{-2}/\mathrm{V}$. In contrast, when the laser was switched on, n_{2D} started to drift to larger values. This drift, however, appeared on a relatively long time scale of several 10 minutes until a saturation of n_{2D} was asserted. The red circles in Fig. 5.2 (a) show saturated $n_{2D}(U_g)$ under these conditions. Apparently, the static n_{2D} could not be changed significantly with U_g under laser operation, which prevented measurements of M and μ as a function of n_{2D}.

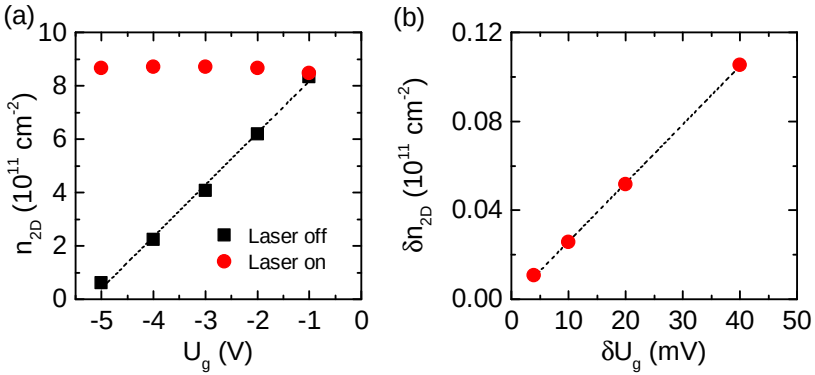

Figure 5.2: (a) (Saturated) electron density n_{2D} as a function of a static gate voltage U_g with the laser switched off (black squares) and with a laser power of 20 nW (red circles). The dashed line represents a linear fit of the data without laser operation, yielding a slope of $\partial n_{2D}/\partial U_g = 1.94 \times 10^{11}\,\mathrm{cm}^{-2}/\mathrm{V}$. (b) Amplitude δn_{2D} measured for a (fast) modulation of U_g with amplitude δU_g and frequency $f = 17.3\,\mathrm{Hz}$. A linear fit yielded the transfer function $\partial n_{2D}/\partial U_g = 2.60 \times 10^{11}\,\mathrm{cm}^{-2}/\mathrm{V}$.

Nonetheless, a modulation of n_{2D} on the order of several Hz was not affected by this drift. For a measurement of $\partial n_{2D}/\partial U_g$ under these conditions, we applied $U_g(t) = \delta U_g \sin(\omega t)$ and detected the dynamic modulation δR_{xy} with lock-in technique.[1] For small changes in n_{2D}, the modulation amplitude δn_{2D} is derived via

$$\delta n_{2D} \approx n_{2D} \frac{\delta R_{xy}}{R_{xy}} \ , \tag{5.1}$$

where n_{2D} is the static density and R_{xy} is the static Hall resistance. We found a linear increase of $\delta n_{2D}(\delta U_g)$ as depicted in Fig. 5.2 (b). A linear fit yielded $\partial n_{2D}/\partial U_g = 2.60 \times 10^{11}\,\mathrm{cm}^{-2}/\mathrm{V}$, which is comparable to the value found for static gate voltages without laser operation. Measurements at different excitation frequencies $f = \omega/(2\pi)$ ranging from 10 Hz to 100 Hz yielded identical values of $\partial n_{2D}/\partial U_g$, which substantiates the fact that the previously discovered drifts of n_{2D} do not play a role at this time scale. Following this analysis, we concluded that the value of the transfer function $\partial n_{2D}/\partial U_g$ as determined from the dynamic Hall measurement is suited best for calibration of $\partial M/\partial N$.

5.2.2 Static and dynamic magnetization

Figure 5.3 (a) and (b) shows experimental curves of the static magnetization M at low and intermediate fields $B_\perp$, respectively. The data were recorded at $\theta = 39.0°$. A background of interconnected splines, which varied slowly on the scale of the oscillation period, was subtracted from the raw M signal to extract its oscillatory part. We observed dHvA oscillations in M with strict $1/B_\perp$-periodicity. From the oscillation period in $1/B_\perp$, we extracted the electron density $n_{2D} = 8.57 \times 10^{11}\,\mathrm{cm}^{-2}$. In the intermediate field regime $1\,\mathrm{T} < B_\perp < 2\,\mathrm{T}$, asymmetric dHvA-oscillations were asserted, with the steep downward flanks corresponding to even integer filling factors. For small fields $B_\perp < 0.8\,\mathrm{T}$, the asymmetry smeared out and the oscillations approached a more sinusoidal shape. A beat node was identified at $B_\perp = 0.63\,\mathrm{T}$. We verified that the downward flanks of the dHvA oscillations at field values below the beat node position corresponded to odd integer filling factors. The maximum

[1] This measurement was performed with constant excitation current I and magnetic field $B_\perp$. The static R_{xy} was measured simultaneously.

visible filling factor was $\nu = 109$. For smaller field values $B_\perp < 0.33\,\mathrm{T}$, the magnetic signal of the 2DES was below the noise level.

Experimental curves of the dynamic magnetization $\partial M/\partial N$, which were recorded simultaneously, are shown in Fig. 5.3 (c) and (d). We observed $1/B_\perp$-periodic magneto-oscillations that were phase-shifted by a quarter of a period with respect to the dHvA oscillations in M. In the intermediate field regime, pronounced peaks were asserted in $\partial M/\partial N$ at field positions where the dHvA oscillations exhibited steep flanks. This behavior is expected because at even integer ν, changes in both $B_\perp$ and N will result in a strong variation of M, which explains the steep flanks in $M(B_\perp)$ and the sharp peaks in $\partial M/\partial N$ at these positions. The oscillatory signal in $\partial M/\partial N$ was detectable down to $B_\perp = 0.21\,\mathrm{T}$, corresponding to $\nu = 168$. This allowed us to identify a second beat node at $B_\perp = 0.3\,\mathrm{T}$, as illustrated in the inset of Fig. 5.3 (c). The observed improvement of resolution of the dynamic measurement can be explained by the enhanced mechanical response of the cantilever near its resonance frequency. Since this response is proportional to the gate modulation δU_g, the resolution in $\partial M/\partial N$ could be further increased by increasing δU_g. However, a modulation of U_g, and hence n_2D, changes the filling factor ν via

$$\delta\nu = \delta n_\mathrm{2D} \frac{h}{eB_\perp} \ . \tag{5.2}$$

Therefore, if $\delta\nu$ is too large, the modulation of n_2D would smear over neighboring ν, thereby reducing the amplitude of the observed magneto-oscillations. In the present experiment, we chose $\delta U_\mathrm{g} = 5.6\,\mathrm{mV}$, corresponding to $\delta n_\mathrm{2D} = 0.015 \times 10^{11}\,\mathrm{cm}^{-2}$. With this configuration, we found that $\delta\nu < 0.5$ at $B_\perp > 0.21$ T, i.e. the modulation of M via n_2D never exceeded a quarter of an oscillation period.[2] In addition to these considerations, we experimentally checked that an increase of δU_g from 5.6 mV to 14 mV did not account for a reduction of amplitude of the observed magneto-oscillations, which confirms that the chosen δU_g was small enough and did not smear the signal in $\partial M/\partial N$.

[2] Magneto-oscillations occurred only at every *second* integer ν in the respective field regime. Therefore, $\delta\nu = 0.5$ corresponded to a change of a *quarter* of an oscillation period in M.

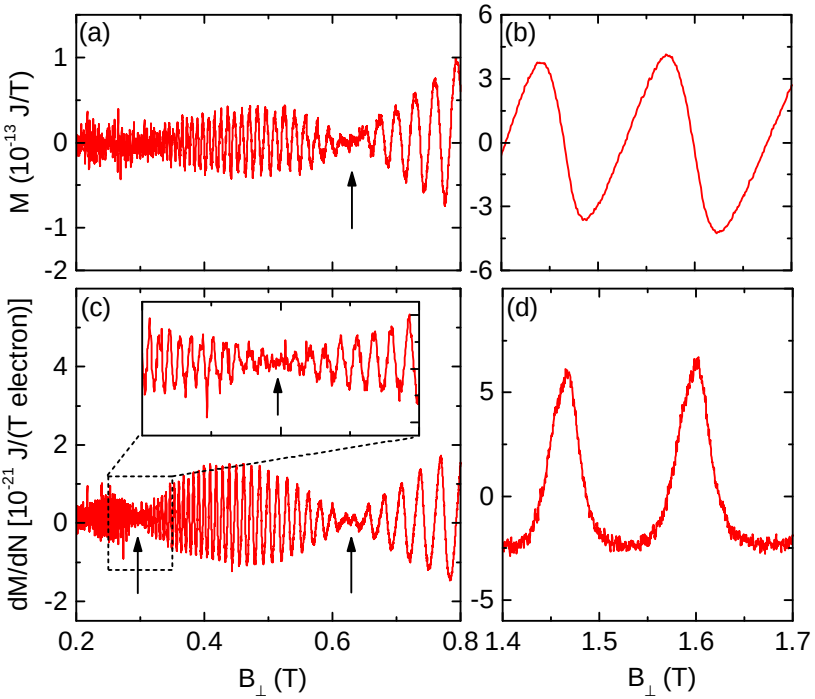

Figure 5.3: Simultaneously measured static magnetization M and dynamic magnetization $\partial M/\partial N$ as a function of $B_\perp$ at different field regimes. The presented data were recorded for sample #4069-5B at $\theta = 39.0°$. In (a) and (b) $M(B_\perp)$ is plotted for small and intermediate fields, respectively. Panels (c) and (d) show the corresponding curves of $\partial M/\partial N(B_\perp)$. In the low-field graphs (a) and (c), observed beat node positions are indicated by arrows. The inset in (c) shows a blow-up of the data in the vicinity of the second node. For the dynamic measurement, a modulation of the gate voltage with $\delta U_g = 5.6\,\mathrm{mV}$ was applied at $f = 92\,\mathrm{Hz}$. The sample temperature was $T = 0.6\,\mathrm{K}$.

5.2.3 Extraction of SOI constants

In the following, we deduce the experimental chemical potential μ and extract the SOI constants α_{R} and β_{D} from the node positions in μ. We calculated the oscillatory part of $\mu(B_\perp)$ from the dynamic measurement of $\partial M/\partial N$ using the Maxwell-relation [Eq. (2.17)] and applying

$$\mu(B_\perp) = -\int \left(\frac{\partial M}{\partial N}\right)_T \cdot dB_\perp \ . \tag{5.3}$$

From the resulting traces $\mu(B_\perp)$, we extracted the two beat node positions by fitting the envelopes of the magneto-oscillations in the vicinity of the nodes with low-order polynomials and finding their crossing points as illustrated in Fig. 5.4 (a) and (b) for the first and second node, respectively. The field positions of the nodes could thus be determined with high accuracy and exhibited error bars of 4 mT for the first and 3 mT for the second node. [3]

In the model calculations, we searched for beat node positions $B_\perp$ in the energy spectra $E_{n'}(B_\perp)$ at which subsequent energy gaps were equal in size, as introduced in section 2.4.1. This allowed us to theoretically predict the first and second beat node as a function of the SOI constants α_{R} and β_{D}. Using this routine, we adjusted α_{R} and β_{D} in order to match the node positions of theory and experiment by means of a least-squares fit. Fixed parameters within this routine were $m^* = 0.037 m_0$, $n_{2\mathrm{D}} = 8.57 \times 10^{11}\,\mathrm{cm}^{-2}$ and $g^* = -4.45$. Since such a fit does not yield unique results for α_{R} and β_{D}, we only considered sets of $(\alpha_{\mathrm{R}}, \beta_{\mathrm{D}})$ with a dominant Rashba parameter, as previously reported for the given InP/InGaAs heterostructure [Rup+13].

Experimental beat node positions as well as extracted SOI constants for different tilt angles θ are summarized in Tab. 5.1 for both samples, #4069-5B and #4069-5C. For the present range of $\theta < 40°$, no significant shifts in $B_\perp$ for both node positions were asserted. Besides the dominant R-parameter α_{R}, the analysis yielded a small, but significant D-contribution β_{D} of order $0.1\alpha_{\mathrm{R}}$, which was neglected in previous investigations of the same heterostructure. The given error bars for the

[3] To rule out possible systematic errors by comparing experiment and simulation, we performed a computer experiment of simulated $\mu(B)$ with different broadening parameters T and Γ. We verified that this method accurately revealed the theoretical node positions as predicted from the energy spectra (c.f. section 2.4.1).

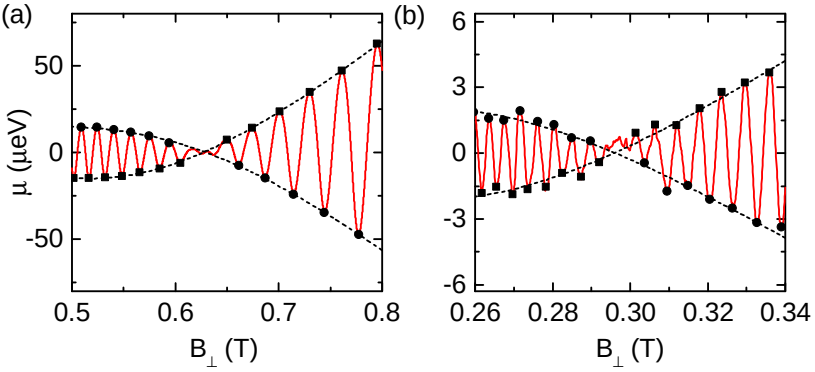

Figure 5.4: Illustration of the procedure to determine beat node positions from the experimental $\mu(B_\perp)$ for (a) first and (b) second node as measured for sample #4069-5B. The envelopes of the observed magneto-oscillations were fitted with low-order polynomials (dashed lines). The node positions were extracted from the crossing points of these fits.

extracted α_R and β_D reflect the uncertainties in the experimental node positions, implying that the R-parameter could be determined with very high accuracy of $\Delta\alpha_R/\alpha_R < 1$ %, while the uncertainty of β_D was on the order of 20 %. The data presented in Tab. 5.1 demonstrate that the obtained results were consistent for both samples #4069-5B and #4069-5C.

5.2.4 Fitting of theoretical model curves to the experiment

Employing the formalism introduced in chapter 2, we directly modeled the curves $M(B_\perp)$ and $\mu(B_\perp)$ using the parameters $g^* = -4.45$, $n_{2D} = 8.57 \times 10^{11}\,\mathrm{cm}^{-2}$, α_R and β_D as in Tab. 5.1 and $T = 0.6\,\mathrm{K}$. The only free parameter left was the level broadening Γ, which we adjusted to match the amplitudes of the magneto-oscillations. In order to check for possible deviations of the experimental M and μ from the single particle model, we simulated both M and μ using *one and the same* parameter set. Simulated and experimental curves of M and μ are presented in Fig. 5.5 (a) and (b) for the intermediate field regime. In

Table 5.1: Field positions of the first two beat nodes at different tilt angles θ measured for both samples #4069-5B, #4069-5C and extracted SOI-constants α_R, β_D. Uncertainties in the node positions are reflected in the error bars given for α_R, β_D. For the calculation, we used $g^* = -4.45$, $m^* = 0.037m_0$ and $n_{2D} = 8.57 \times 10^{11}\,\mathrm{cm}^{-2}$

sample	θ	node 1	node 2	α_R	β_D
	(°)	(T)		($\times 10^{-12}$ eVm)	
#4069-5B	14.0	0.629	0.296	4.42 ± 0.02	0.48 ± 0.10
	29.0	0.629	0.297	4.44 ± 0.02	0.43 ± 0.10
	39.0	0.629	0.297	4.44 ± 0.02	0.46 ± 0.10
#4069-5C	18.8	0.625	0.297	4.44 ± 0.02	0.49 ± 0.10
	28.8	0.625	0.298	4.45 ± 0.02	0.54 ± 0.10
	38.8	0.631	0.295	4.44 ± 0.02	0.38 ± 0.10

the background of Fig. 5.5 (b), the calculated DOS is illustrated via a gray-scale plot together with the discrete $E_{n'}(B_\perp)$ (dashed lines). Here, the experimental μ was offset by the theoretical zero-field Fermi energy $E_F = (\pi\hbar^2 n_{2D})/m^*$. For both quantities M and μ, we found that experiment and simulation were in very good agreement and no significant deviation of the experimental oscillation amplitudes ΔM and $\Delta\mu$ with respect to the the model curves was asserted. Therefore, our experiment confirms the relation $\Delta M/N = \Delta\mu/B_\perp$ [Wie+97] for the investigated 2DES.

We found $\Gamma = 0.83\,\mathrm{meV}/\sqrt{\mathrm{T}}$ for sample #4069-5B, which was larger than $\Gamma = 0.6\,\mathrm{meV}/\sqrt{\mathrm{T}}$ extracted for sample #4069-5C. We attribute this behavior to residual inhomogeneities across the wafer. Previously, a value of $\Gamma = 0.5\,\mathrm{meV}/\sqrt{\mathrm{T}}$ was reported for samples prepared from the same wafer [Rup+13]. From the gray-scale plot of the DOS it is clear that odd integer filling factors due to spin splitting could not be resolved within the present field regime, because the level broadening was too large.

The same comparison of experimental and simulated M and μ for the low-field regime is depicted in Fig. 5.6. The model parameters were identical to the results presented in Fig. 5.5. Also for this field

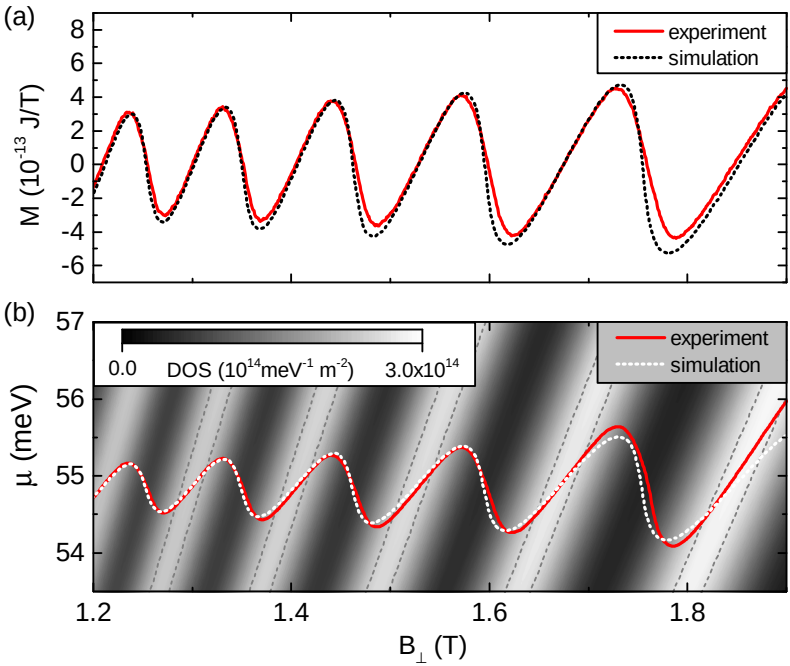

Figure 5.5: Comparison of experiment (sample #4069-5B, red curves) and simulation (dotted curves) of (a) magnetization $M(B_\perp)$ and (b) chemical potential $\mu(B_\perp)$ at intermediate fields. The experimental μ was vertically shifted by the zero-field Fermi energy $E_\mathrm{F} = (\pi\hbar^2 n_\mathrm{2D})/m^*$. In the bottom panel, the calculated density of states is illustrated as a gray-scale plot together with the discrete $E_{n'}(B_\perp)$ (thin dashed lines). The model curves in (a) and (b) were calculated using one and the same parameter set, being $m^* = 0.037m_0$, $g^* = -4.45$, $n_\mathrm{2D} = 8.57 \times 10^{11}\,\mathrm{cm}^{-2}$, $\alpha_\mathrm{R} = 4.42 \times 10^{-12}\,\mathrm{eVm}$, $\beta_\mathrm{D} = 0.48 \times 10^{-12}\,\mathrm{eVm}$ $T = 0.6\,\mathrm{K}$ and $\Gamma = 0.8\,\mathrm{meV}/\sqrt{\mathrm{T}}$.

regime, we found excellent agreement between experiment and simulation, including the predicted positions of the beat nodes. We observe a remaining discrepancy in that the experimental amplitude $\Delta\mu$ at small fields was larger than the theoretical prediction. This enhancement of the experimental $\Delta\mu$ with respect to the prediction by the model, however, was not observed for sample #4069-5C. The modeling of $M(B_\perp)$

demonstrates that the second beat node could not be resolved experimentally, because the noise level was much larger than the predicted dHvA amplitudes at small fields.

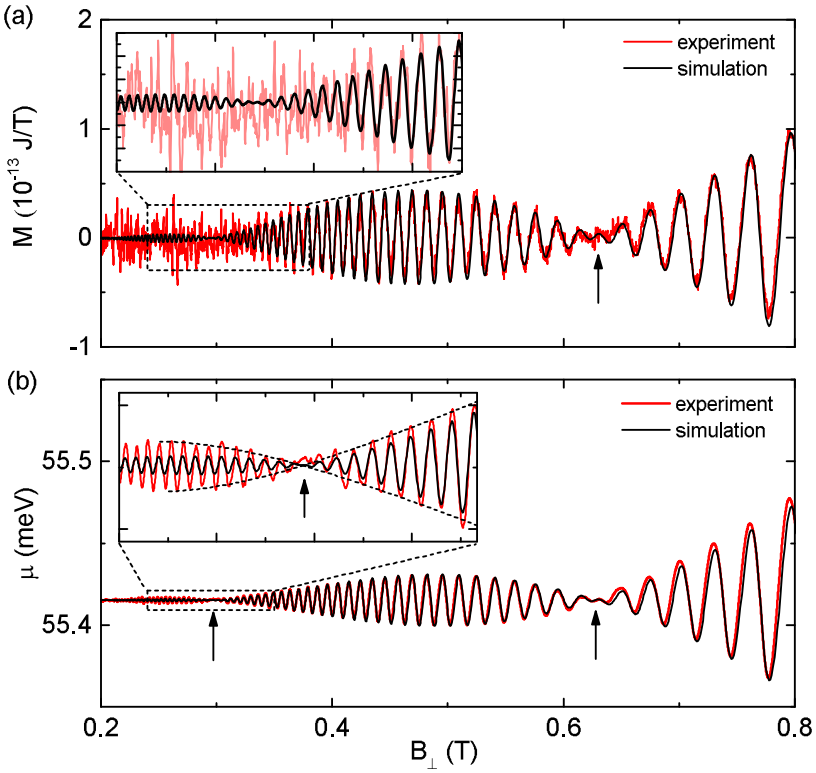

Figure 5.6: Comparison of experiment (sample #4069-5B, red curves) and modeling (black curves) for (a) $M(B_\perp)$ and (b) $\mu(B_\perp)$ at small magnetic fields. Beat node positions are marked by arrows. The insets show zooms of the second beat node. Simulation parameters were identical to those reported in Fig. 5.5.

5.3 Discussion

With the present experiment, we showed that the magnetization M as well as the chemical potential μ could be addressed in a simultaneous measurement. For the InP/InGaAs-based 2DES investigated here, both quantities exhibited $1/B_\perp$-periodic magneto-oscillations at low temperatures. The measurement of μ featured an enhanced sensitivity as compared to M in the sense that quantum oscillations were detectable down to much smaller fields. In quantitative terms, we state that the signal-to-noise ratio of the dynamic measurement was increased by a factor of ≈ 10 as opposed to the quasi-static operation. This significant enhancement in sensitivity was attributed to the increased mechanical response of the cantilever for the dynamic measurement with a modulation frequency close to the mechanical resonance frequency.

Both M and μ showed characteristic beating patterns which we attributed to SOI effects. To date, this is the first experimental observation of SOI-related beatings in the quantum oscillatory μ of a 2DES. The enhanced sensitivity of the dynamic measurement allowed to identify a second beat node in μ which was beyond experimental reach for the quasi-static measurement of M. By using the theoretical model introduced in section 2.4.3, we extracted both Rashba and Dresselhaus parameters α_R and β_D from the two experimental beat node positions in μ. Here, the improved procedure to extract these positions via fits of the oscillation envelopes allowed for a very precise measurement of α_R and β_D. As a result, we could show that, in addition to a dominant Rashba parameter, a small Dresselhaus contribution β_D on the order of $0.1\alpha_\mathrm{R}$ was required to accurately model the data. To substantiate this fact we note that model curves $\mu(B_\perp)$ deviated from the experimental data if only R-SOI was taken into account (not shown). To the best of our knowledge, this is the first experimental demonstration that both Rashba and Dresselhaus contributions are relevant to describe SOI-related beating patterns in 2DES-based magneto oscillations. Following the considerations in section 2.4.3, we note that for perpendicular field orientation, the beatings do not depend on the sign of $\alpha_\mathrm{R}/\beta_\mathrm{D}$. This holds also true for increasing tilt angle θ as long as the beat nodes do not shift to higher field values, as it is the case for the experimental node positions reported in Tab. 5.1. Following this, we report absolute values of α_R and β_D and also state that the exact in-plane angle φ is irrelevant

in the modeling of the present data. The determination of the relative sign of α_R/β_D requires high tilt angles, where the in-plane anisotropies in the beating pattern become relevant, as we will demonstrate via magnetotransport measurements in chapter 6.

In the following, we discuss further implications which underline the great potential of the presented measurement technique to investigate the electronic structure of 2DESs. We stress that the combined detection of M and μ provides complementary insights into the 2DES ground state properties. Here, the ability to measure both quantities on one-and-the-same 2DES during the same cool-down process is essential for a direct comparison of M and μ, because separate measurements might suffer from drifts of the 2DES density n_{2D} upon thermal cycling. While the magnetization $M = -\partial F/\partial B_\perp$ probes changes in the total free energy, the chemical potential $\mu = \partial F/\partial N$ monitors the highest occupied states, and is not sensitive to changes in the low-lying occupied states. Theory predicts that in a single particle picture the amplitudes of the magneto oscillations ΔM and $\Delta\mu$ are related via $\Delta M/N = \Delta\mu/B_\perp$ [Wie+97]. We confirmed this relation experimentally by showing that both M and μ were reproduced quantitatively using a single particle model with identical input parameters. However, a simultaneous measurement of M and μ would be of particular interest to investigate 2DESs that exhibit electron-electron interaction effects. Although the relation $\Delta M/N = \Delta\mu/B_\perp$ was shown to hold true also for interacting electrons in the Hartree-Fock approximation [MOL86], a modeling that includes dynamic screening effects predicts a strong enhancement of ΔM over $\Delta\mu$ [Mei+01]. The presented technique allows to explore this discrepancy experimentally. With the ability to tune the static 2DES density n_{2D} via the integrated gate electrode, possible interaction effects may even be tuned to significant strength *in situ* via reducing n_{2D} to very small values. Furthermore, the gate electrode is relevant if the interplay of the gate-tunable R-SOI and D-SOI is to be studied in the quantum oscillations of M and μ, which was not possible for the present samples due to long-term drifts of n_{2D}. In addition, the combined access to M and μ is suitable to study quantum Hall ferromagnetism of 2DESs. While signatures of this effect were addressed previously in $\mu(B)$ [Lee+14], a direct measurement of the expected magnetic hysteresis in $M(B)$ has not yet been reported. Finally, we state that the presented technique is also of great potential to investigate the

electronic properties and electron-electron interaction effects of novel 2D materials [MAH14].

6 Investigation of spin-orbit interaction by anisotropic magnetotransport

Access to the absolute values and relative sign of the SOI parameters α_{R} and β_{D} in 2DESs can be obtained in experiments which probe the in-plane anisotropy of measured quantities. As for the magneto-oscillations, we showed theoretically in chapter 2 that the SOI-related node positions will shift as a function of the in-plane angle φ in tilted field experiments, enabling to extract α_{R} and β_{D}. However, if an external magnetic field is applied, in general the anisotropy of the Landé $\overline{\overline{g}}^*$-tensor has to be considered in the modeling. While the out-of-plane anisotropy of $\overline{\overline{g}}^*$ is independent of SOI effects, the existence of an in-plane off-diagonal component g_{xy} is directly connected to the presence of both SIA and BIA [KK93]. The respective correlations are summarized in the following relations:

$$\begin{aligned} g_{xy} &= \frac{2\gamma e}{\hbar\mu_B}\left(\langle k_z^2\rangle\langle z\rangle - \langle k_z^2 z\rangle\right) \qquad \text{c.f. Ref. [KK93]} \\ \beta_{\mathrm{D}} &= \gamma\left(\langle k_z^2\rangle - \frac{1}{4}k_{\mathrm{F}}^2\right) \\ \alpha_{\mathrm{R}} &= \langle r_{41}^{6c6c}\mathcal{E}\rangle\,. \end{aligned} \tag{6.1}$$

For the parameter definitions see section 2.3. Like the Dresselhaus parameter β_{D}, g_{xy} is proportional to the bulk Dresselhaus parameter γ. Additionally the wave function needs to be asymmetric in the z-direction perpendicular to the QW to obtain a non-zero g_{xy}. A z-asymmetry of the wave function is also required to obtain a non-zero Rashba parameter α_{R}, because expectation values of z and p_z also enter r_{41}^{6c6c} [Win03]. However, details on the electron wave function $w(z)$ for the investigated heterostructure are not known and a numerical treatment to estimate

$w(z)$ is beyond the scope of this work. In that sense, α_R, β_D and the components of $\overline{\overline{g}}^*$ are to be treated as independent parameters and have to be determined experimentally.

So far, SOI-induced in-plane anisotropies were addressed, e.g., by Ganichev *et. al.*, who measured the anisotropy of φ-dependent spin-photocurrents on InAs/AlGaSb single quantum wells [Gan+04]. They were able to extract the ratio α_R/β_D from their measurements independent of $\overline{\overline{g}}^*$, but absolute values could not be obtained with the method. In a subsequent work, Meier *et. al.* [Mei+07] addressed the spin precession of electrons as a function of their φ-dependent in-plane momentum. Via time-resolved Faraday rotation they extracted spin-orbit magnetic fields B_{BIA} and B_{SIA} and were able to report both absolute values and relative sign of α_R and β_D. However, anisotropies in the $\overline{\overline{g}}^*$-tensor, although necessary in the analysis of the data, were not considered in their work. Larionov and Golub demonstrated the tunability of α_R/β_D via a gate voltage in angle-dependent, time-resolved Kerr rotation experiments on AlGaAs heterostructures [LG08]. Most recently, Saskai *et. al.* investigated the anisotropy of spin scattering rates in etched GaAs/AlGaAs nanowires as a function of an in-plane magnetic field via weak-localization dips in magnetoconductance measurements [Sas+14]. From their analysis, the ratio α_R/β_D could be determined directly with high accuracy and without fitting routines. Furthermore, they observed the persistent spin helix symmetry, i.e., $\alpha_R = \beta_D$, via a gate-controlled tuning of α_R. Absolute values of α_R and β_D were also reported, but were subject to sizable uncertainties.

One of the first attempts to address SOI-induced spin-splitting in semiconductor heterostructures was via magnetotransport measurements. Already in the late 1980s, the zero field spin splitting due to R-SOI was extracted from beating patterns in the Shubnikov-de Haas (SdH)-oscillations and the θ-dependence of the beating pattern was investigated [Luo+88; Das+89; Luo+90; DDR90]. Later experimental studies of SdH beating patterns also focused on samples with a dominant R parameter and neglected a possible D-contribution [Eng+97; Nit+97; Gru00; Fan+11]. Up to now, in-plane anisotropies of SOI-related beat node positions probed by tilted field experiments lack a detailed investigation.

The out-of-plane anisotropy of $\overline{\overline{g}}^*$ has been intensively studied in AlGaAs-based samples [Le +97; MH00; PZ06], where no substantial

deviation between $g_\perp$ and $g_\parallel$ was asserted. Only little experimental data on $g_\perp$, $g_\parallel$ was published for InGaAs/InP-based heterostructures. Kowalski *et. al.* measured $g_\perp$ and $g_\parallel$ on $In_xGa_{1-x}As$ QWs for $0.4 < x < 0.6$ via optically detected magnetic resonance and reported a significant out-of-plane anisotropy with a constant $g_\perp/g_\parallel \approx 0.6$ independent of the In-content x. They also found that the anisotropy increased for smaller QW width.

Measurements of the in-plane anisotropy of $\overline{\overline{g}}^*$ were first demonstrated by Oestreich *et. al.* on symmetric AlGaAs-based QWs subjected to a perpendicular electric field, using spin quantum beat spectroscopy [OHR96]. This technique was also applied in a recent work, where g_{xy} and the spin-relaxation rate were measured simultaneously, which allowed to extract absolute values of α_R and β_D [Eld+11]. The authors showed that, despite a significant in-plane anisotropy of $\overline{\overline{g}}^*$, the R-SOI parameter can be small in isomorphous QW structures, i.e. where the asymmetry is achieved via a variation of alloy concentration. So far, the in-plane anisotropy of $\overline{\overline{g}}^*$ in asymmetric InGaAs/InP-based heterostructures is unexplored.

In this chapter, we present magnetotransport experiments in external magnetic fields, where we varied both tilt angles θ and φ. We show that SdH-oscillations exhibit beat nodes, with the first node exhibiting a substantial in-plane anisotropy. From the measured node positions we extract both absolute values and relative sign of α_R and β_D via a fit of the theoretical model to the data. Furthermore, we report all three components of the $\overline{\overline{g}}^*$-tensor and discuss the relevance of anisotropies in $\overline{\overline{g}}^*$ for a correct modeling of the experimental data. Therefore, the in-plane anisotropy of g_{xy} is measured directly via the coincidence technique, while the out-of-plane anisotropy is taken as a fit parameter in the model. We note here that torque cantilever magnetometry experiments are inappropriate for these measurements, because the beam of the cantilever defines a specific in-plane direction for $\mathbf{B}$ and experiments are limited *in situ* to a fixed φ. However, beat nodes in R_{xx} can be extracted from the evolution of amplitudes ΔR_{xx} at even and odd filling factors. A direct simulation of $R_{xx}(B_\perp)$ which would require to include additional effects in the simulations such as scattering mechanisms is not necessary.

The chapter is organized as follows. In section 6.1, we present the coincidence measurements to address the in-plane anisotropy of $\overline{\overline{g}}^*$.

Experimental R_{xx}-data in doubly tilted fields addressing the evolution of node positions are shown in section 6.2. We introduce the fitting procedure to extract the SOI and $\overline{\overline{g}}^*$ parameters in section 6.3.1. We discuss our findings in section 6.4.

6.1 Measurement of the in-plane $\overline{\overline{g}}^*$-tensor anisotropy

In this section we experimentally address the in-plane anisotropy of $\overline{\overline{g}}^*$ for the investigated heterostructure using the coincidence technique. Here, we will extract the components g_{xy} and g_{80}. The latter describes a superposition of $g_\perp$ and $g_\parallel$ at the measured coincidence angle of $\theta \approx 80°$.

6.1.1 Experimental methods

The main idea to extract parameters of $\overline{\overline{g}}^*$ from magnetotransport measurements is to analyze the spin splitting Δ_s at large $B_\perp$, where the Zeeman interaction dominates and the contribution of SOI-terms is almost negligible. In this special case, Δ_s can be expressed via a scalar, but angle dependent g^*-factor $g^*(\theta, \varphi)$ as in Eq. (2.33). We now use the coincidence method to determine $g^*(\theta, \varphi)$ at particular values of θ and φ. In order to achieve large field values needed for this experiment, a single-axis 15 T-magnet was used. A ^{3}He cryostat featuring a rotatable stage allowed for continuous variation of the polar angle θ. The Hall-bar sample was mounted in two different in-plane orientations, namely $\varphi = 45°$ ($\parallel$ [110]) and $\varphi = 135°$ ($\parallel$ [1$\bar{1}$0]) as depicted in Fig. 6.1 (a) and (b), respectively. These in-plane orientations matched the expected extremal values of $g^*(\theta, \varphi)$ predicted by our theoretical model. The measurements for the two in-plane directions were accomplished in different cool-down cycles, because the in-plane rotation of the sample stage had to be performed *ex situ*. Magnetotransport data was recorded via the application of an AC current $I = 100\,\mathrm{nA}$ (rms) at $f = 17.3\,\mathrm{Hz}$ between contacts 1 and 5 and simultaneously measuring $R_{xx} = V_{2-4}/I$ and $R_{xy} = V_{3-7}/I$ with two separate lock-in amplifiers (c.f. Fig. 3.9).

To determine $g^*(\theta, \varphi)$, we chose the angle of half coincidence $\theta_c^{1/2}$. From previous experiments [Rup+13] we expected $\theta_c^{1/2}$ on the order of

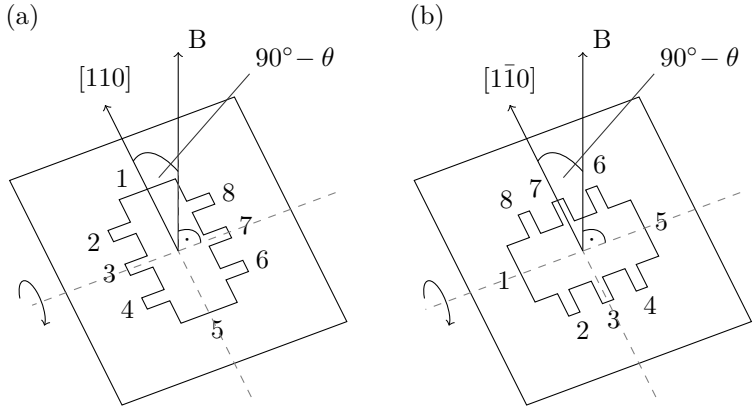

Figure 6.1: Sketch of experimental setup to determine the in-plane $\overline{\overline{g}}^*$-tensor anisotropy. The Hall-bar sample was mounted on a rotatable stage in two different in-plane configurations with (a) $\varphi = 45°$ and (b) $\varphi = 135°$, corresponding to $B_\parallel \parallel [110]$ and $B_\parallel \parallel [1\bar{1}0]$, respectively. The polar angle θ could be varied *in situ*.

$\approx 80.5°$. This allowed for a maximum perpendicular field component of $B_\perp \approx 2.5\,\mathrm{T}$. Larger coincidence angles were not considered in the experiments, since they led to smaller $B_\perp$ and thus to a greater influence of SOI-terms.

Now, for each of both in-plane orientations φ, we recorded $R_{xx}(B)$ and $R_{xy}(B)$ simultaneously for different values of θ in the vicinity of the expected $\theta_c^{1/2}$. In order to improve the accuracy, we determined the exact values of θ and $B_\perp$ by matching the respective R_{xy} slopes with R_{xy} recorded at $\theta = 0°$. The condition of half coincidence implied that all energy levels $E_{n'}$ were equally spaced, i.e., even and odd filling factors were expected to contribute equally to the oscillations in R_{xx}. Therefore, we compared the amplitudes of the R_{xx}-peaks of neighboring filling factors to determine $\theta_c^{1/2}$. Comparing the distances $\Delta(1/B_\perp)_\nu$ between two subsequent maxima for neighboring filling factors (c.f. [Sav+96; Gui+00; Des+04]) led to larger uncertainties in $\theta_c^{1/2}$.

6.1.2 Experimental results

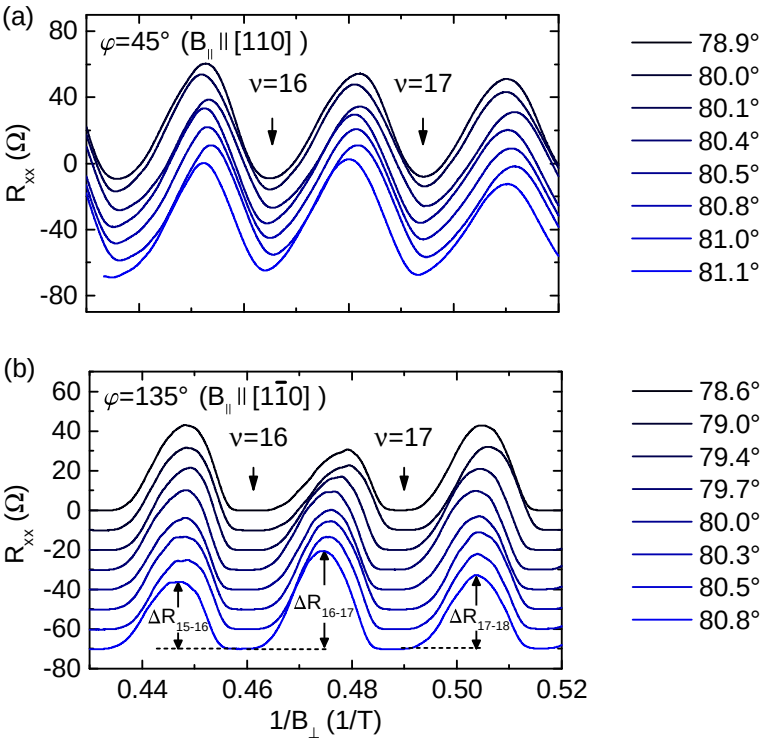

Figure 6.2: R_{xx} data as a function of $1/B_\perp$ for different tilt angles θ with (a) $\varphi = 45°$ and (b) $\varphi = 135°$. The curves were offset for clarity. R_{xx}-minima for $\nu = 16$ and $\nu = 17$ are indicated by arrows. The sample temperature was (a) $T \approx 0.8\,\mathrm{K}$ and (b) $T \approx 0.3\,\mathrm{K}$. Amplitudes of the maxima denoted as ΔR_{15-16}, ΔR_{16-17} and ΔR_{17-18} are illustrated for the bottom curve in (b).

We now present results of the coincidence measurements for sample #4069-7. R_{xx} data as a function of $1/B_\perp$ for different values of θ and for in-plane directions $\varphi = 45°$ and $\varphi = 135°$ are plotted in Fig. 6.2 (a) and (b), respectively. After illumination with a blue LED, electron densities were $n_{2D} = 8.43 \times 10^{11}\,\mathrm{cm}^{-2}$ for $\varphi = 45°$ and $n_{2D} = 8.49 \times 10^{11}\,\mathrm{cm}^{-2}$ for $\varphi = 135°$. For the measurements at $\varphi = 45°$, the temperature

was $T = 0.8\,\mathrm{K}$, possibly because of a thermal link to the ^{4}He-reservoir. The R_{xx}-oscillations did not show broad minima as opposed to the measurements at $\varphi = 135°$, where a base temperature of $T = 0.3\,\mathrm{K}$ was achieved.

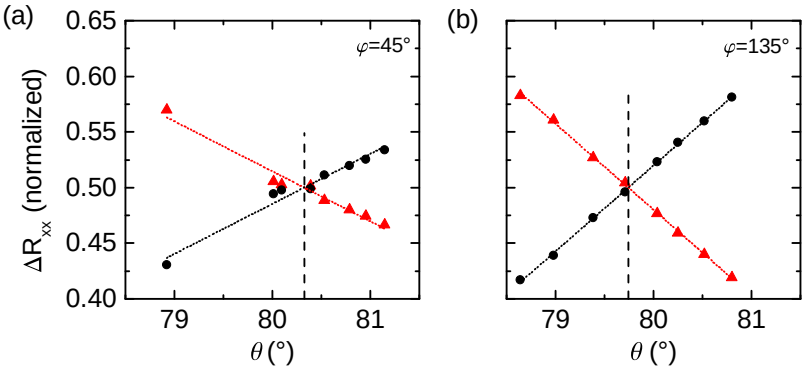

Figure 6.3: R_{xx} peak amplitudes Δ_{16-17} (red triangles) and $^1/_2(\Delta_{15-16} + \Delta_{17-18})$ (black circles) as a function of the tilt angle θ for (a) $\varphi = 45°$ and (b) $\varphi = 135°$. Each pair of amplitudes was normalized such that their sum was equal to one. Linear fits of the data are indicated by dotted lines. The vertical dashed lines mark the extracted coincidence angle $\theta_c^{1/2}$ as the crossing point of the fits.

We used the amplitudes of the R_{xx}-peaks next to filling factors $\nu = 16$ and $\nu = 17$ to determine the coincidence angle $\theta_c^{1/2}$. Those were labeled with, e.g., Δ_{16-17}, highlighting that the respective peak was located between filling factors 16 and 17. In order to compensate the effect of an overall amplitude decrease towards smaller $B_\perp$, we calculated the average $^1/_2(\Delta_{15-16} + \Delta_{17-18})$ and compared it with Δ_{16-17}. Furthermore, the amplitudes were normalized such that the sum of each pair equaled one. This was done to compensate for possible temperature variations between different R_{xx} sweeps. The extracted amplitudes are summarized in Fig. 6.3. To interpolate between the measured data, we performed linear fits of the different datasets and determined $\theta_c^{1/2}$ via their crossing points. The extracted $\theta_c^{1/2}$, as well as calculated scalar g^* are summarized in Tab. 6.1. Note that the effective

Table 6.1: Extracted coincidence angles $\theta_c^{1/2}$ and calculated g^* for sample #4069-7.

φ (°)	$\theta_c^{1/2}$ (°)	g^*
45	80.33 ± 0.1	-4.54 ± 0.05
135	79.74 ± 0.1	-4.81 ± 0.05

g^*-factors are negative, which is commonly accepted for InP/InGaAs QWs [Kow+94].

We assert a significant difference of g^* for the two in-plane directions, which we attribute to the in-plane anisotropy of g^*. However, the deviations from an isotropic g^* are obviously small, which implies $g_{xy} \ll (g_\parallel, g_\perp)$. Thus, we can simplify Eq. (2.33) to

$$g^*(\theta,\varphi) \approx g_\parallel \sqrt{q^2\cos^2\theta + \sin^2\theta} + \frac{\sin^2\theta}{\sqrt{q^2\cos^2\theta + \sin^2\theta}} \sin 2\varphi \; g_{xy} \; . \tag{6.2}$$

Here, we substituted $g_\perp = q \; g_\parallel$, because we cannot determine the out-of-plane anisotropy of g^* with the experimental data at hand. For the polar angle $\theta \approx 80°$, we find that the θ-dependent factor of the second summand is ≈ 1 even for relatively large variations of the parameter q. If we further substitute $g_{80} = g_\parallel \sqrt{q^2\cos^2 80° + \sin^2 80°}$, we arrive at the simple form

$$g^*(\theta,\varphi) \approx g_{80} + g_{xy} \; \sin 2\varphi \; . \tag{6.3}$$

Using this equation, we extracted the values for g_{80} and g_{xy} from the R_{xx}-amplitude analysis as follows:

$$\boxed{\begin{aligned} g_{80} &= -4.68 \pm 0.04 \\ g_{xy} &= 0.14 \pm 0.04 \; . \end{aligned}} \tag{6.4}$$

6.2 Measurement of the in-plane anisotropy of node positions

In this section, we present experiments addressing the in-plane anisotropy of SOI-induced node positions in strongly tilted fields. First, we describe in detail the procedure of recording magnetotransport data in doubly tilted fields using a 2D vector magnet. Next, we demonstrate how to extract node positions from the R_{xx} quantum oscillations and show that a significant anisotroy is present in the data.

6.2.1 Experimental methods

In order to experimentally investigate the theoretically predicted in-plane anisotropy of beat nodes introduced in 2.4, it is necessary to perform radial field sweeps at a constant polar angle θ for different values of the in-plane angle φ. For this, both angles must be adjustable *in situ* with high accuracy. This is in particular challenging since the anisotropy can only be addressed if θ is close to the coincidence angle $\theta_c^{1/2}$, where the node positions depend strongly on θ itself. Consequently, uncertainties in θ could obscure the in-plane anisotropy.

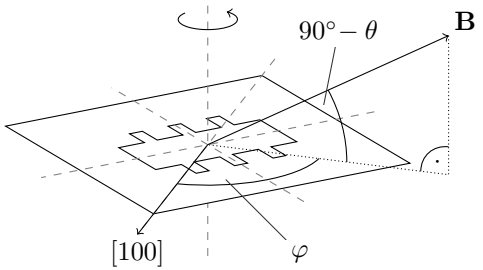

Figure 6.4: Sketch of the experimental setup used for magnetotransport experiments in doubly tilted fields. The Hall-bar sample was mounted on a horizontal stage and could be rotated mechanically in the 2DES plane. The magnetic field **B** was applied using a 2D vector magnet system, allowing for electronic adjustment of the tilt angle θ.

To account for these specific challenges, we mounted the sample on a horizontal stage inside a ^{3}He-system, which could be rotated mechanically about its vertical axis (Fig. 6.4), corresponding to the adjustment of the in-plane angle φ. The magnetic field was applied using a 2-axis vector magnet with radial field strength of 4.5 T and with its field plane perpendicular to the sample surface. The advantage of this setup lies in the fact that the polar angle θ could be adjusted electronically with a resolution of 0.01°.

Experimental magnetotransport data were recorded for two different Hall bars prepared from the same wafer, named #4069-6 and #4069-7. Both samples led to consistent results. After cool-down, the samples were briefly illuminated with a blue LED to increase n_{2D} via the persistent photoeffect. R_{xx} and R_{xy} were measured simultaneously using an excitation current of $I = 100\,\mathrm{nA}$ (rms) at $f = 17.3\,\mathrm{Hz}$ and phase-sensitive voltage detection, similar to the measurements presented in 6.1. The sample temperature was $T = 0.3\,\mathrm{K}$. The experiments were now carried out as follows. After setting a particular in-plane angle φ, we first determined the residual offset angle θ_0 stemming from a possible misalignment of the sample stage normal. This was done by performing a tangential sweep of the magnetic field in the vicinity of $\theta = 90°$, while recording the Hall-resistance R_{xy} of the sample. We obtained the offset angle θ_0 by the zero-crossing of $R_{xy}(\theta)$, including subtraction of an offset in R_{xy} present at $B = 0$. Next, we performed radial field sweeps for three different values $\theta = \{77°, 78°, 79°\}$. To account for possible systematic errors, the values of θ were then re-determined from the R_{xy}-slopes by comparing to a measurement at $\theta = 0°$. We found that these measured values of θ showed a systematic offset of $-0.5°$ compared to the preset values of the vector magnet system. However, the relative spread for a preset θ at different values of φ was as small as $\Delta\theta \approx 0.07°$, accurate enough for the analysis of node positions as discussed later.

6.2.2 Experimental results

Figure 6.5 presents R_{xx}-data of sample #4069-7 at $\theta = 77.5°$ for three different in-plane orientations $\varphi = \{45°, 90°, 135°\}$. At the position of the first beat node, both even and odd ν were resolved in the SdH-oscillations. The node position was therefore located at fields where

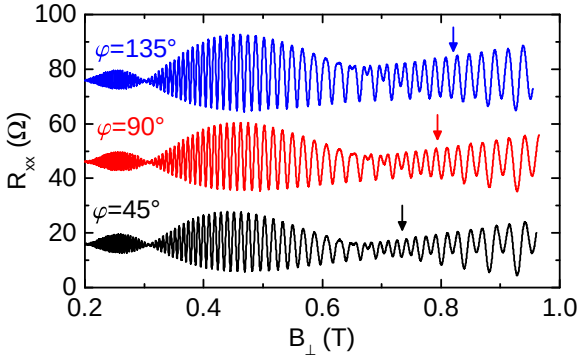

Figure 6.5: R_{xx}-data as a function of $B_\perp$ of sample #4069-7 for $\theta = 77.5°$ and in-plane orientations φ of 45°, 90° and 135°. The position of the first node is indicated by an arrow for each curve. Sample temperature was $T = 0.3\,\mathrm{K}$.

both oscillation types featured equal amplitudes. The position of the first node significantly shifted with φ (indicated by arrows), while the second node at $\approx 0.31\,\mathrm{T}$ node hardly moved for different values of φ.

In order to extract the node positions systematically with high accuracy, we performed the following analysis. For the first node, we determined the R_{xx}-amplitude at each filling factor, ΔR_ν, as the average of the peak heights right and left to the respective ν-minimum, $\Delta R_{\nu,+}$ and $\Delta R_{\nu,-}$, as illustrated in Fig. 6.6 (a). Next, we fitted the amplitudes ΔR_ν for even and odd ν by a second order polynomial in $1/B_\perp$ in the vicinity of the node. The extracted node position was the crossing point of the two fits [see Fig. 6.6 (b)]. In the vicinity of the second node, only one type of oscillations, i.e., even or odd ν, were present. Here, we used the envelopes of the oscillation extrema to determine the node position. We estimated the uncertainty in $1/B_\perp$ of the node positions to $\approx 0.02\,\mathrm{T}^{-1}$. The uncertainty of the positions due to variations of the tilt angle θ can be estimated by the experimental θ-dependence of the node positions. In anticipation of results presented further down, we state that the first node moved with $\approx 0.05\,\mathrm{T}^{-1}/\theta(°)$ in the range of $76.5° - 78.5°$. With $\Delta\theta \approx 0.07°$, this yields an uncertainty of $0.004\,\mathrm{T}^{-1}$, which is negligible.

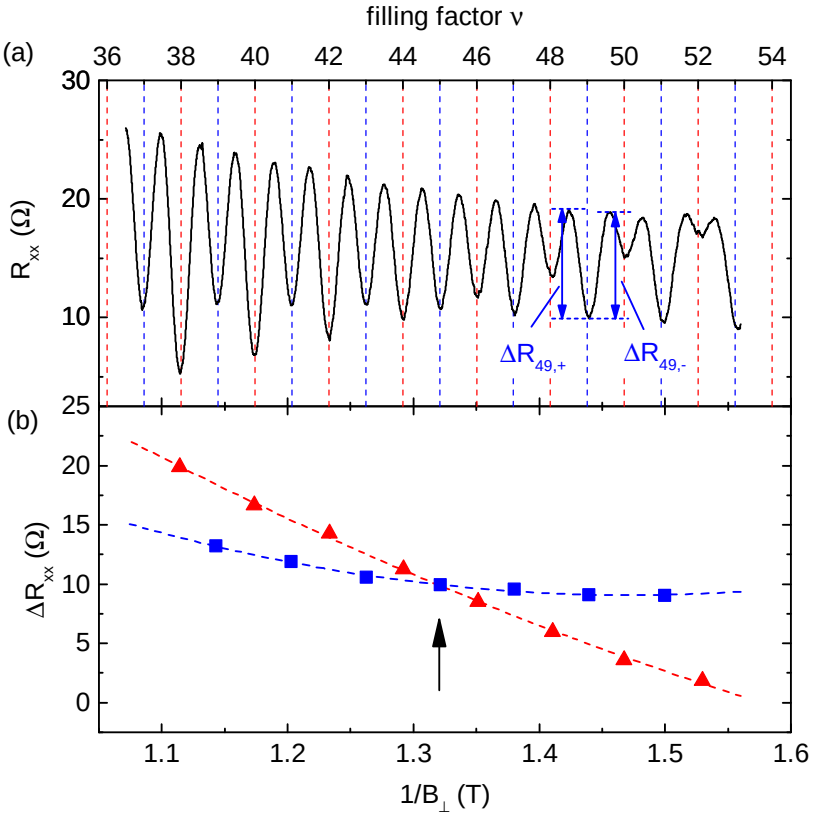

Figure 6.6: Illustration of the method to extract the first node position from experimental R_{xx}-data. (a) R_{xx}-trace of sample #4069-7 as a function of $1/B_\perp$ at $\theta = 77.5^\circ$ and $\varphi = 90^\circ$. Even and odd filling factor positions are indicated by red and blue vertical dashed lines, respectively. Relevant amplitudes $\Delta R_{\nu,+}$ and $\Delta R_{\nu,-}$ are indicated exemplarily for $\nu = 49$. (b) Extracted amplitudes $1/2(\Delta R_{\nu,+} + \Delta R_{\nu,-})$ for even (red triangles) and odd filling factors (blue squares) from the curve shown in (a). Dashed lines represent second-order polynomial fits of the data. The node position is given by the crossing point of the fits.

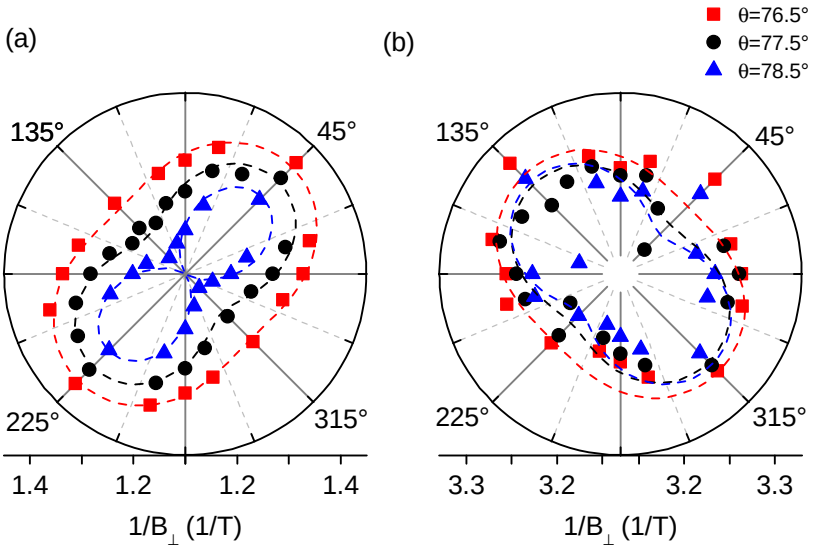

Figure 6.7: Experimental field positions of (a) first and (b) second node as a function of the in-plane angle φ for different tilt angles θ. The dashed lines represent fits of the theoretical model to the data. Fixed model parameters were $n_{2D} = 8.51 \times 10^{11}\,\mathrm{cm}^{-2}$, $g_\perp = g_\parallel = -4.68$ and $g_{xy} = 0$.

Extracted node positions of sample #4069-7 for the three different addressed tilt angles θ for the first and second node are summarized in φ-polar plots in Fig. 6.7 (a) and (b), respectively. We found a significant in-plane anisotropy with in-plane axes along [110] and [1$\bar{1}$0] for the position of the first node. The maximum variation in the node position versus φ was on the order of $0.15\,\mathrm{T}^{-1}$ and thus much larger than the estimated uncertainty. As θ was increased, the node moved to higher field values (i.e. smaller values of $1/B_\perp$) and the degree of anisotropy increased. Furthermore, the positions of the second node also exhibited a small anisotropic behavior, which was rotated with respect to the one observed for the first node.

6.3 Fitting of the data with theoretical model

We used the experimental node positions to determine the SOI parameters α_R and β_D with the help of the theoretical model introduced in 2.4. In a first approach, we assumed an isotropic g^*-factor in the modeling. A treatment including the full anisotropic $\overline{\overline{g}}^*$-tensor will be addressed further down.

6.3.1 Fitting with isotropic g^*-factor

For each position set recorded at a specific value of θ, we performed a least-squares fitting routine with variable parameters α_R and β_D, such that the theoretically predicted node positions fitted best with the experimental ones. Fixed parameters were $n_{2D} = 8.51 \times 10^{11}\,\mathrm{cm}^{-2}$ as determined from the periodicity of the SdH-oscillations, $m^* = 0.037 m_0$ as reported in [Rup+13] and $g^* = g_{80}$ obtained from coincidence measurements presented in 6.1.

Resulting fit curves for both nodes and different θ are plotted as dashed lines in Fig. 6.7. We find that experiment and model are in very good agreement for both nodes. In particular, both anisotropies and θ- dependencies found experimentally are accurately modeled by the simulation. The corresponding fit parameters α_R and β_D are summarized in Tab. 6.2. Following these results, we are able to confirm a strong R-SOI and a non-zero, but small D-SOI parameter. Secondly, from the in-plane orientation of the anisotropy pattern, we find that the relative sign of α_R with respect to β_D is positive. These conclusions are possible because the present fit routine reveals a *unique* set (α_R, β_D) (except for the absolute sign), i.e., there is no second set that fits the data comparably well. We find that both values of α_R and β_D in Tab. 6.2 vary only slightly for the fits at different θ, which supports the validity of the model. Only a slight increase of β_D with θ is asserted. Absolute values of α_R and β_D are very close to the ones found in the measurements of the chemical potential μ (section 5), with β_D on the order of 0.1 α_R. Average values measured for sample #4069-6 were $\alpha_R = 4.32 \times 10^{-12}\,\mathrm{eVm}$ and $\beta_D = 0.72 \times 10^{-12}\,\mathrm{eVm}$.

Furthermore, in order to compare to the coincidence experiments made in 6.1, we calculated the expected coincidence angles $\theta_c^{1/2}$ at $B_\perp = 2.5\,\mathrm{T}$ for $\varphi = 45°$ and $\varphi = 135°$ (last two columns in Tab. 6.2).

Table 6.2: Extracted SOI parameters α_R and β_D of sample #4069-7 after fitting the theoretical model to the experimental node positions for the three addressed polar angles θ. Fixed simulation parameters were $g^* = -4.68$, $n_{2D} = 8.51 \times 10^{11}\,\mathrm{cm}^{-2}$ and $m^* = 0.037 m_0$. Furthermore, θ_{45} and θ_{135} are predicted coincidence angles $\theta_c^{1/2}$ at $B_\perp = 2.5\,\mathrm{T}$ for the calculated parameter set and for $\varphi = 45°$ and $\varphi = 135°$, respectively.

θ	α_R	β_D	θ_{45}	θ_{135}
(°)	($\times 10^{-12}$ eVm)		(°)	
76.5	4.50	0.67	80.20	80.00
77.5	4.50	0.72	80.21	80.00
78.5	4.48	0.78	80.23	80.00

These can be directly compared to experimental values listed in Tab. 6.1. Even without assuming any anisotropy of g^*, the calculation predicts an in-plane anisotropic behavior of $\theta_c^{1/2}$ with $\Delta\theta_c^{1/2} \approx 0.2°$ stemming from the presence of both SOI terms. However, the calculated anisotropy is smaller than the experimental value of $\Delta\theta_c^{1/2} \approx 0.6°$. We therefore conclude that a more realistic model to describe the data should include anisotropies of the $\overline{\overline{g}}^*$-tensor.

6.3.2 Fitting procedure including $\overline{\overline{g}}^*$-tensor anisotropy

The $\overline{\overline{g}}^*$-tensor of a (001)-oriented QW has three independent components $g_\perp$, $g_\parallel$ and g_{xy} (c.f. section 2.3.1), and all three of them influence the calculated beat node positions as a function of θ and ϕ.

The coincidence measurements presented in section 6.1 provided the two parameters g_{80} and g_{xy}, which allowed to address the in-plane anisotropy only. Here, the previous analysis assuming $g_{xy} = 0$ revealed a significant contribution of the SOI terms to the anisotropy of $\theta_c^{1/2}$ at $B_\perp = 2.5$ T. This contribution had the same sense of direction as a positive g_{xy}, i.e., $\theta_{45} > \theta_{135}$. Therefore, the value of $g_{xy} = 0.14$ as determined in section 6.1 can be understood as an upper limit, because the residual influence of the SOI contributions was neglected. The true g_{xy} should lie in between 0 and 0.14. A possible out-of-plane anisotropy

of $\overline{\overline{g}}^*$ is embedded in the parameter $q = g_\perp/g_\parallel$, which is not known from the experiment. The out-of-plane components of $\overline{\overline{g}}^*$ as a function of q and g_{80} are derived via

$$\begin{aligned} g_\parallel &= \frac{g_{80}}{\sqrt{q^2\cos^2 80° + \sin^2 80°}} \quad \text{and} \\ g_\perp &= q g_\parallel \ . \end{aligned} \tag{6.5}$$

In order to get access to this out-of-plane anisotropy, we included q into our fitting procedure as a third fitting parameter. Furthermore, we extended the experimental dataset that entered the fitting to contain all node positions measured at different φ and different θ. By this means, the fitting also accounted for the experimental θ-evolution, which should reflect possible effects of the out-of-plane anisotropy of $\overline{\overline{g}}^*$. As fixed parameters, we used $m^* = 0.037m_0$, $n_{2\mathrm{D}} = 8.51 \times 10^{11}$ cm^{-2} and $g_{80} = -4.68$ as measured in section 6.1. We performed the fit for different $g_{xy} \in \{0, ..., 0.14\}$ to iteratively find the value of g_{xy} predicting the correct anisotropy of $\theta_c^{1/2}$.

Table 6.3: Extracted fit parameters $q = g_\perp/g_\parallel$, α_R and β_D for the modified fitting routine including experimental node positions at different θ and φ. Fixed parameters were $m^* = 0.037m_0$, $n_{2\mathrm{D}} = 8.51 \times 10^{11}\,\mathrm{cm}^{-2}$, $g_{80} = -4.68$ and g_{xy} as specified in the first column. θ_{45} and θ_{135} are predicted coincidence angles at $B_\perp = 2.5\,\mathrm{T}$ and $\Delta\theta_c^{1/2} = \theta_{45} - \theta_{135}$. The dataset with $g_{xy} = 0.11$ (marked in gray color) fitted best with the experiment in terms of $\Delta\theta_c^{1/2}$.

g_{xy}	q	α_R	β_D	θ_{45}	θ_{135}	$\Delta\theta_c^{1/2}$
		($\times 10^{-12}$ eVm)			(°)	
0	0.80	4.56	0.61	80.23	80.05	0.18
0.05	0.71	4.59	0.54	80.34	79.97	0.37
0.08	0.66	4.60	0.50	80.40	79.92	0.48
0.10	0.63	4.61	0.47	80.45	79.89	0.56
0.11	0.62	4.62	0.46	80.47	79.88	0.59
0.12	0.60	4.62	0.44	80.48	79.86	0.62
0.14	0.58	4.63	0.41	80.52	79.83	0.69

Table 6.3 presents the extracted parameters q, α_{R} and β_{D} as results of the modified fitting procedure for different values of g_{xy}. The fits reveal a significant out-of-plane anisotropy with $q = g_{\perp}/g_{\parallel} < 1$. Regarding the absolute values of the fit parameters, we find that q systematically decreases as g_{xy} increases. Furthermore, the extracted β_D is getting smaller at an increase of g_{xy} and a decrease of q. Apart from that, we find that α_{R} is relatively unaffected by the invoked anisotropy of $\overline{\overline{g}}^*$ with an overall variation of only 2 %. At this point, we note that in absence of D-SOI, i.e. $\beta_{\mathrm{D}} = 0$, the in-plane anisotropy of $\overline{\overline{g}}^*$ alone cannot explain the experimental data. Although the presence of g_{xy} itself provokes a φ-anisotropy of the first node even if $\beta_{\mathrm{D}} = 0$, the latter is predicted to be too small if we assume the largest $g_{xy} = 0.14$ consistent with the previous coincidence experiment (not shown). This confirms the result of a finite, but small β_{D}.

By comparing predicted anisotropy of the coincidence angle $\Delta\theta_c^{1/2}$ to the measurements made in section 6.1, we find that the value of $g_{xy} = 0.11$ predicts $\Delta\theta_c^{1/2} = 0.59°$, consistent with the experiment. We therefore conclude that the respective parameter set fits the experimental data best. Because of the relatively strong variation of β_{D} as a function of the input parameters and the choice of the fitting routine, we estimate its uncertainty to ≈ 20 %. Likewise, the uncertainty in q is on the same order of magnitude. The best fit values of the extracted SOI-constants and $\overline{\overline{g}}^*$-components including their errors are summarized as follows:

$$\begin{aligned} \alpha_{\mathrm{R}} &= (4.62 \pm 0.09) \times 10^{-12}\,\mathrm{eVm} \\ \beta_{\mathrm{D}} &= (0.46 \pm 0.14) \times 10^{-12}\,\mathrm{eVm} \\ g_{\perp} &= -2.91 \pm 0.60 \\ g_{\parallel} &= -4.72 \pm 0.05 \\ g_{xy} &= 0.11 \pm 0.02\ . \end{aligned} \tag{6.6}$$

Resulting fit curves for the first node are plotted in Fig. 6.8 together with the experimental data. Again, the predicted node positions agree well with the experiment. Only the experimental values measured at $\theta = 78.5°$ are located at slightly smaller field values as in the modeling.

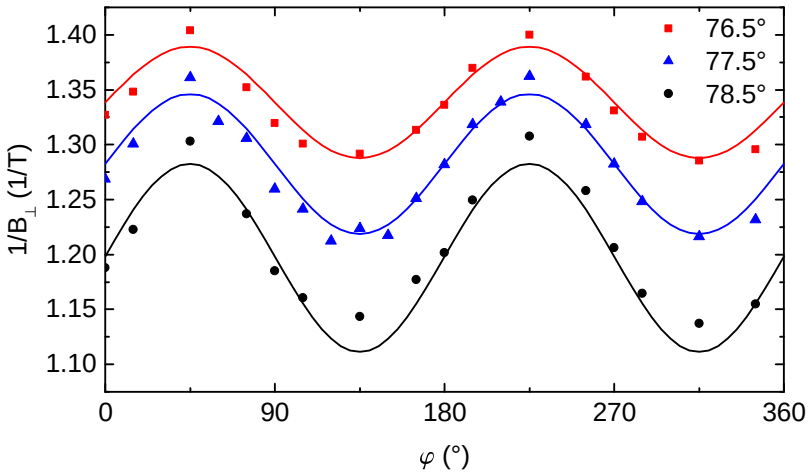

Figure 6.8: Experimental data (symbols) and respective fit curves (solid lines) of the first node position as a function of φ using the modified fitting procedure including the full g^* anisotropy. Fixed parameters were $n_{2D} = 8.51 \times 10^{11}\,\mathrm{cm}^{-2}$, $m^* = 0.037 m_0$, $g_{s0} = -4.68$ and $g_{xy} = 0.11$. Extracted fit parameters were $\alpha_R = 4.62 \times 10^{-12}\,\mathrm{eVm}$, $\beta_D = 0.46 \times 10^{-12}\,\mathrm{eVm}$ and $q = g_\perp / g_\parallel = 0.62$.

6.4 Discussion

With the present experiment, it was possible to address SOI-induced in-plane anisotropies in magneto-oscillations for the first time. Via the systematic analysis of node positions and coincidence angles at different θ and φ, we could extract the relevant SOI-parameters α_R and β_D and the full $\overline{\overline{g}}^*$-anisotropy. To the best of our knowledge, this is the first experiment that reports all of these parameters at the same time and thus provides a more comprehensive picture of spin-related phenomena in semiconductor heterostructures. In particular, the combined detection of α_R, β_D and $\overline{\overline{g}}^*$ should enable to validate theoretical predictions on their interplay based on $\mathbf{k} \cdot \mathbf{p}$-theory [Kow+94; Win03; PZ06].

For the investigated samples, the outcome of a dominant α_R is consistent with published results on the same kind of samples [Sch+98; Rup+13], which, however, neglected a possible D-contribution β_D. Our

experiment showed that the samples were subject also to a finite, but small β_D on the order of $0.1\,\alpha_R$, which confirms the results of chapter 5. In addition, we extracted the relative sign of α_R/β_D to be positive, which was ambiguous in the previous analysis of $\mu(B)$ at moderate tilt angles. Furthermore, a strong R-SOI had to be assumed *a priori* in those measurements, while it came out as a definitive result in the present analysis. In a comparison with previous in-plane experiments to address α_R and β_D [Gan+04; Mei+07; Eld+11], we emphasize that the method presented here is especially suited to study 2DESs where one of the two components is small. If one of the terms is zero, the node positions are isotropic in φ. The breaking of this symmetry is very sensitive to a small contribution of the term that was formerly absent. On the other hand, the case $\alpha_R/\beta_D \approx 1$ is difficult to address with the present technique, because the nodes vanish for most in-plane angles φ [c.f. Fig. 2.12 (b)].

The analysis of the data revealed that the φ-evolution of node positions as measured at tilt angles close to the coincidence angle $\theta_c^{1/2}$ was very sensitive to the effective g^*-factor. In particular, a complete and consistent description was only possible if an anisotropic $\overline{\overline{g}}^*$-tensor was assumed and if all three components of $\overline{\overline{g}}^*$ were considered in the modeling. However, independent measurements of $g_\perp$, $g_\parallel$ and g_{xy} from magneto-oscillations are complicated because of the interplay between SOI and Zeeman interaction.

The determination of g_{xy} via φ-dependent coincidence measurements led to systematic deviations of g_{xy}, because at the applied $B_\perp$ of only 2.5 T, SOI still influenced the respective coincidence angles. Nonetheless, the size of this effect was clarified in the modeling of the node positions, while simultaneously accounting for the correct degree of anisotropy in $\theta_c^{1/2}$. In our particular case, only ≈ 70 % of the measured anisotropy in $\theta_c^{1/2}$ could be attributed to the presence of g_{xy}. Addressing the pure components of $\overline{\overline{g}}^*$ in a coincidence measurement requires larger values of $B_\perp$. Our modeling predicts that at $B_\perp \approx 10\,\mathrm{T}$, the SOI contribution on $\theta_c^{1/2}$ should be negligible. However, at $\theta \approx 80°$, this amounts to $B \approx 58\,\mathrm{T}$, which can only be reached in pulsed magnets at large scale facilities.

The out-of-plane anisotropy of $\overline{\overline{g}}^*$, represented by the tensor components $g_\perp$ and $g_\parallel$, was not addressed directly in the experiment, but

was extracted in terms of a third fit parameter $q = g_\perp/g_\parallel$ from the θ-evolution of the nodes. The obtained $g_\perp = -2.98$ and $g_\parallel = -4.72$ suggest a remarkable out-of plane anisotropy of $\overline{\overline{g}}^*$ and are consistent with measurements of $g_\perp$ and $g_\parallel$ by Kowalski *et. al.* [Kow+94]. A substantial out-of-plane anisotropy of $\overline{\overline{g}}^*$ in InGaAs is also predicted by $\mathbf{k}\cdot\mathbf{p}$-theory, but in an opposite way as was reported experimentally, i.e., $|g_\perp| > |g_\parallel|$ [Win03]. However, the correct model to derive $g_\perp$ and $g_\parallel$ is debated [PZ06], and further experimental investigations on different heterostructures should help to gain a more detailed understanding of the $\overline{\overline{g}}^*$-anisotropy. Considering the present results, we found that the value of $q = g_\perp/g_\parallel$ obtained by our fit routine was subject to a relatively large uncertainty, which we also identified as the main source of error for the extracted SOI parameters α_R and β_D. Consequently, an accurate measurement of all components of $\overline{\overline{g}}^*$ could further increase the accuracy of α_R and β_D as determined via the presented technique. Using magnetotransport, such measurements could be realized by analyzing the T-dependent R_{xx}-amplitudes of odd ν at large $B_\perp$, which allows to extract the respective Zeeman gaps [Kri+15]. However, as demonstrated in Ref. [Kri+15], even in InGaAs/InP-based 2DES the measured components of $\overline{\overline{g}}^*$ are subject to an exchange enhancement at large $B_\perp$, while the values relevant for the node positions at moderate $B_\perp$ are not influenced by electron-electron interactions and, correspondingly, smaller.

7 Magnetization of nanopatterned InP/InGaAs quantum dots

Experiments presented in chapters 5 and 6 were dedicated to SOI effects in 2DESs, which we addressed by beating patterns in the magneto-oscillations. Anticipated applications of SOI, e.g. in high-speed logical spintronics devices, will require a miniaturization of the relevant structures. A straightforward way to investigate effects of such miniaturization is to fabricate nanopatterned 2DES mesas. In particular, as these structures become small, the interplay between lateral confinement and SOI may alter the underlying physics significantly. Therefore, a more profound understanding of SOI mechanisms in laterally confined electron systems is indispensable for future device applications.

Up to now, SOI effects in confined geometries have only rarely been studied experimentally. In Ref. [SKG04], the authors observed beating patters in the magnetotransport of etched quantum wires, which were processed from the same type of heterostructure as studied in this work. They found that the beat nodes were shifted to higher fields for narrow wires, which was attributed to the confinement. In a subsequent theoretical treatment [KS05], the authors modeled the beat node positions as a function of wire width. Their model predicted a shift of the nodes to smaller fields for narrow wires, which was inconsistent with their experiment. However, they invoked that also the Rashba parameter itself could be modified because of a change of the built-in electric field or a change in penetration of the wave function into the barriers upon confinement.

A further reduction of dimensionality is achieved in quantum dots. SOI effects in the energy spectra of dots were addressed theoretically in numerous works [TLG04; CP05; PC06; CAC07]. However, these studies

focused on dots with only a few electrons. So far, SOI contributions on the energy spectra of dots containing several hundreds of electrons are unexplored, both in theory and experiment.

Even without considering possible SOI effects, the electron systems in etched dots provide intriguing physics as demonstrated in various experimental studies based on optical and electrical techniques [Cha92]. Theoretical works suggest that magnetization measurements should address the relevant energy spectra in a complementary way [SI88; KLS90; FLS94]. As already introduced in 2.5, theory predicts that the magneto-oscillations of a 2DES are significantly altered if lateral confinement is present. Torque magnetometry is especially suited to study these oscillations in quantum dots because magnetotransport experiments are, in contrast to quantum wires, difficult to perform on 0D structures. Furthermore, magnetometry is a non-invasive technique, i.e., the sample is measured in its equilibrium state and there is no need for applying electrical currents or for optical excitation.

Experimental data on quantum dot magnetization is scarce. In 2002, Schwarz *et. al.* observed dHvA-oscillations of an ensemble of quantum dots prepared from AlGaAs-based heterostructures [Sch+02b]. However, the data could not be modeled with a single-particle ansatz using a parabolic confinement potential. Furthermore, a significant temperature dependence of the oscillation amplitudes with respect to those of a reference 2DES was reported. The authors attributed this behavior to electron-electron interactions, which was further corroborated in a subsequent theoretical treatment [DLS04].

In comparison to the AlGaAs dots of Schwarz *et. al.*, the InGaAs/InP material system used in this work provides particular advantages to study quantum dot magnetization. Due to its small effective mass of $0.037\,m_0$, the dHvA-amplitudes are expected to be larger. Second, interaction effects should play a less prominent role, as suggested by the smaller interaction parameter

$$r_\mathrm{S} = \frac{1}{a_\mathrm{B}^* \sqrt{\pi n_\mathrm{2D}}} \,, \tag{7.1}$$

which yields $r_\mathrm{S} \approx 0.3$ for the InGaAs/InP system as opposed to $r_\mathrm{S} \approx 1.2$ for GaAs [$a_\mathrm{B}^* = (4\pi\epsilon_0\epsilon_\mathrm{r}\hbar^2)/(e^2 m^*)$ is the effective Bohr radius]. This

supports the use of a single particle ansatz to describe the electron system inside InGaAs/InP dots.

The correct shape of the lateral confinement potential in nanopatterned 2DESs depends on various sample parameters. It is known that AlGaAs-based structures are subject to surface charges, which pin the Fermi level several 100 meV below the conduction band [CTA87]. The confinement near the center of these structures can be well approximated by a parabolic potential [Rie+97]. However, if populated by many electrons, screening effects lead to a flattening of the effective potential near the center [LFS88; KLS90]. The resulting potential is hard-wall like, but a significant edge depletion is present [CTA87] due to the surface charges in nanopatterned AlGaAs structures. A profound treatment of similar confinement effects in InGaAs/InP-based nanostructures is lacking. It is known that the Fermi level of InGaAs is pinned near the conduction band edge [KMS73], suggesting a flat confinement potential with hard walls at the physical border of the dots. Furthermore, effective screening evoked by the small r_S parameter supports the hypothesis of HW confinement. Still, previous works modeled these structures with a parabolic confinement ansatz [Ker+90; KS05].

In this chapter, we present magnetization experiments on ensembles of quantum dots which were nanopatterned from InGaAs/InP heterostructures. We measured $1/B_\perp$-periodic dHvA-type oscillations down to field values as small as $B_\perp = 2.0\,\mathrm{T}$. From the amplitude, shape and periodicity of the oscillations we analyze the lateral shape of the confinement potential. Via a quantitative analysis of the experimental data and a fitting of model curves to the experiment we extracted relevant sample parameters such as electron number N and depletion width w_D. Furthermore, we include the effect of ensemble broadening into the modeling and show that the prepared QD array features a high degree of homogeneity. Signatures of SOI-related beat nodes were not observed. Still, with the experimental data at hand, we draw conclusions on the relevance of SOI in the observed dot structures and outline what future experiments would allow one to address SOI in the magnetization of quantum dots.

7.1 Experimental methods

Two samples denoted with #4069-1A and #3556-1 were prepared from two different wafers #4069 and #3556, respectively. The preparation process is described in detail in 3.1.3. The dot mesa on each sample consisted of $8 \times 4 = 32$ write fields of the electron beam lithography system of $(200 \times 200)\,\mu\text{m}^2$ in size, giving a total number of 2.5×10^6 dots. From SEM images, we determined the physical diameter of the dots to $d = 460 \pm 10\,\text{nm}$, giving a statistical spread $\Delta d/d = 2\,\%$ across the ensemble.

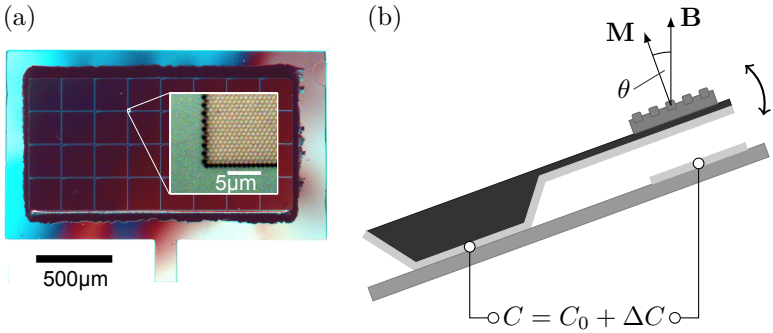

Figure 7.1: (a) Optical microscope image of sample #4069-1A placed on the paddle of a micromechanical cantilever. The sample featured a mesa structure consisting of (8×4) write fields containing etched nanoscopic dots. The inset shows a magnification of the dot mesa. (b) Schematic side-view of the cantilever illustrating the direction of the applied magnetic field **B** and the capacitive readout scheme.

Samples were placed on micromechanical GaAs cantilevers featuring metallized electrodes for capacitive readout [c.f. section 3.2.2]. A microscope image of sample #4069-1A on the cantilever paddle is depicted in Fig. 7.1 (a). Experimental calibration constants yielded $3.14 \times 10^{-8}\,\frac{\text{Nm}}{\text{pF}}$ (sample #4069-1A) and $1.78 \times 10^{-8}\,\frac{\text{Nm}}{\text{pF}}$ (sample #3556-1). Measurements were carried out in a ^{3}He insert with a fixed stage, allowing for a base temperature of $T = 0.28\,\text{K}$. The sample temperature was measured via a calibrated Cernox thermometer mounted next to

the sample. The tilt angle θ was set to 52° prior to cool down. Magnetic field sweeps were performed using the 9 T / 4.5 T vector magnet system for sample #4069-1A and a single axis 15 T magnet for sample #3556-1. Experimental traces $M(B)$ were obtained as follows. First, we recorded the capacitance change $\Delta C(B)$ and averaged the data over four sweeps (2×up and 2×down) to effectively reduce the amount of statistical noise. A mixing of the sweep directions in the averaging was possible because no significant hysteresis between up- and down-sweep was present within the field range of interest. Second, a polynomial background was subtracted from the raw capacitance data. Finally, we evaluated $M = (K_{\mathrm{C}}\Delta C)/(B\sin\theta)$. For the investigated 2DES, it is known that illumination after cool down increases $n_{2\mathrm{D}}$ in the QW via the persistent photoeffect. We recorded magnetization data before illumination as well as after illumination for 10 s with a blue light emitting diode. We compare the magnetization of the dot mesa with measurements on reference 2DESs prepared from the same wafers, which were carried out under similar conditions. In comparison with the 2DES reference data, we found $M(B)$ to be consistent for both wafers, though absolute values varied as discussed later.

7.2 Experimental results

Experimental M as a function of $1/B_\perp$ of wafer #4069 is plotted in Fig. 7.2. Figure 7.2 (a) shows M of the reference 2DES, while the magnetization of the dot ensemble before and after illumination is plotted in Fig. 7.2 (b) and (c), respectively. For a direct comparison of the signal amplitudes, we normalized M to the total physical mesa area, first by neglecting possible depletion effects. The 2DES reference measurement exhibited sawtooth-shaped $1/B_\perp$-periodic dHvA oscillations with steep upward flanks. Also for the dot mesa, dHvA-type oscillations with $1/B_\perp$-periodicity were identified. However, they had a smoother shape, faded out towards smaller $B_\perp$ and vanished for $B_\perp < 2\,\mathrm{T}$. The upward flanks corresponding to effective filling factor $\nu^* = 8$ are marked for all curves in Fig. 7.2. We note that only even ν^* were observed and signatures of spin splitting were absent in the data. Using the vector magnet system, we also performed field sweeps at different tilt angles θ for sample #4069-1A (not shown). We found a slight decrease of

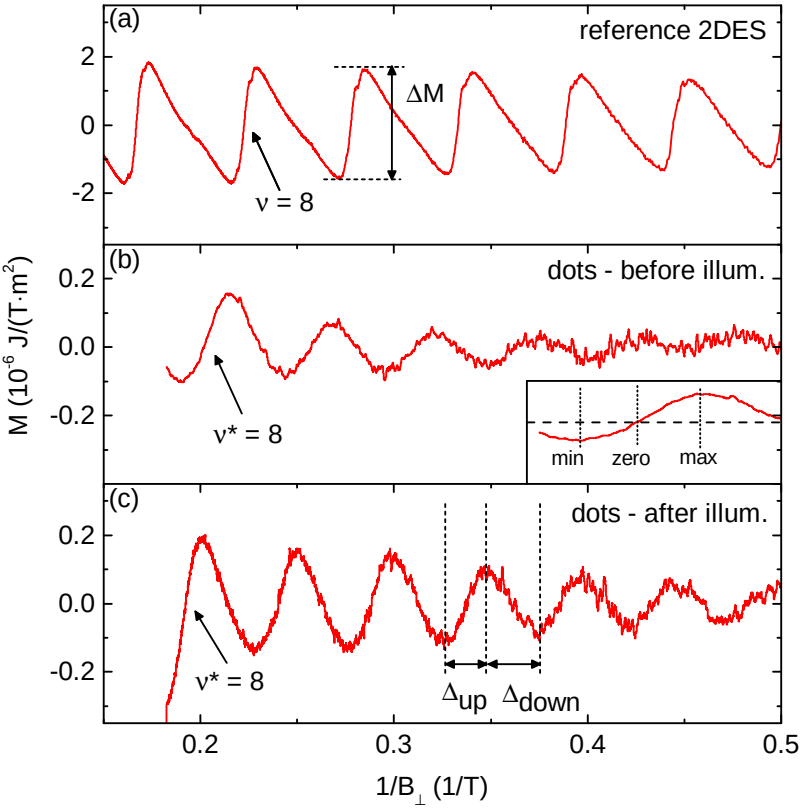

Figure 7.2: Magnetization M as a function of $1/B_\perp$ (wafer #4069) of (a) reference 2DES, (b) dot ensemble before and (c) after illumination. All data were normalized to the total physical mesa area neglecting edge depletion. The sample temperature was $T = 0.28\,\mathrm{K}$. Upward flanks corresponding to $\nu^* = 8$ are marked by arrows. The amplitude ΔM of $\nu = 10$ is indicated in (a). The inset in (b) illustrates relevant field positions of minimum, zero-crossing and maximum used for data analysis.

the dHvA amplitudes of order ≈ 10 % for increasing tilt angles, while maintaining the positions of the oscillations in $1/B_\perp$.

For a quantitative analysis of oscillation shape and periodicity of the dHvA-oscillations, we extracted characteristic field positions $1/B_\perp$ of minima, zero crossings and maxima for each visible ν^* as depicted in the inset of Fig. 7.2 (b). First, we considered the peak-to-peak amplitudes

$$\Delta M = (M_{\max} - M_{\min})_{\nu^*} \tag{7.2}$$

which are summarized for 2DES and dot mesa of both wafers in Tab. 7.1. Remarkably, the normalized dHvA amplitude of the dot ensemble was reduced by at least one order of magnitude as compared to the 2DES reference. Illumination increased ΔM of the dots by a factor of ≈ 2 and more filling factors were identified in the data. A direct comparison of ΔM for both wafers showed that the dHvA amplitudes of wafer #3556 were smaller by a factor of ≈ 2 as compared to those of wafer #4069.

Second, we analyzed the asymmetry of the oscillations quantitatively. For this, we defined the ratio $\Delta_{\mathrm{up}}/\Delta_{\mathrm{down}}$ of the relative $1/B_\perp$-positions of subsequent maxima and minima, as illustrated in Fig. 7.2 (c). Prior to illumination, the dHvA oscillations of the dots were nearly symmetric with $\Delta_{\mathrm{up}}/\Delta_{\mathrm{down}} \approx 1$ for all visible ν^*. After illumination, the oscillations at small ν^* were slightly asymmetric with $\Delta_{\mathrm{up}}/\Delta_{\mathrm{down}} \approx 0.8$, and became symmetric for higher ν^*. The 2DES mesa exhibited sawtooth-like dHvA oscillations with $\Delta_{\mathrm{up}}/\Delta_{\mathrm{down}}$ of order $0.2 \ldots 0.5$.

Finally, we examined the periodicity of the oscillations in detail. We extracted the period

$$p_{\nu^*} = (1/B_\perp)_{\max,\nu^*+1} - (1/B_\perp)_{\max,\nu^*+1} \tag{7.3}$$

for each ν^* and found all measured curves to be periodic in $1/B_\perp$ within $\Delta p/p < 5$ %. The dHvA frequency measured for the dot ensemble $f_{1/B_\perp} = 1/p$ increased by $\approx 8 - 12$ % upon illumination, which was consistent with the relative increase of $f_{1/B_\perp}$ after illumination observed for the 2DES reference samples (not shown). However, we found that $f_{1/B_\perp}$ of the dots was generally by $\approx 10 - 20$ % larger than $f_{1/B_\perp}$ of the reference 2DES. Furthermore, we plotted the assigned ν^* as a function of the previously defined characteristic field positions in fan charts, as

Table 7.1: Comparison of the extracted amplitudes ΔM of reference 2DES and dot mesa structures for wafers #3556 and #4069. Abbreviations: (d): dark and (i): after illumination.

wafer	$\nu^{(*)}$	ΔM $\left[10^{-6}\mathrm{J/(T\,m^2)}\right]$		
		2DES (i)	dots (d)	dots (i)
#3556	6	1.70	0.12	0.24
	8	1.45	0.08	0.15
	10	1.21	0.04	0.10
	12	1.12	0.02	0.07
	14	0.89	-	0.05
	16	-	-	-
#4069	6	3.55	-	-
	8	3.38	0.26	-
	10	3.17	0.15	0.29
	12	2.99	0.11	0.27
	14	2.81	0.08	0.20
	16	2.64	0.06	0.16

done in Fig. 7.3 for sample #3556-1. We performed linear fits to each dataset, following the equation

$$\nu^* = f_{1/B_\perp} \times (1/B_\perp) + \Delta\nu^* \ . \tag{7.4}$$

These regressions allow to extract the frequency $f_{1/B_\perp}$ and the offset $\Delta\nu^*$ of each position set. Here, $\Delta\nu^*$ can be understood as a phase shift of the characteristic positions (e.g. the maxima) with respect to the filling factor positions assigned with the steep dHvA flanks of an ideal 2DES with the same dHvA frequency $f_{1/B_\perp}$. If the measured curves were a result of symmetric broadening of the ideal dHvA oscillations, the zero-crossings of the upward flanks should exhibit $\Delta\nu^* = 0$. However, for the oscillations measured before illumination, we found $\Delta\nu^* > 0$, and therefore a significant shift of the oscillations to higher magnetic fields.

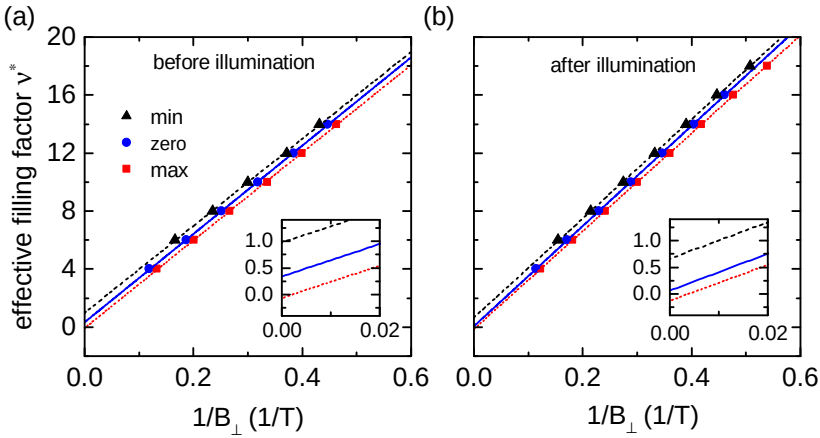

Figure 7.3: Fan charts of minima, zero-crossings and maxima positions of the observed oscillations for sample #3556-1. The plots show data taken before (a) and after illumination (b). A linear regression was applied to each dataset. Insets in both plots show a blow-up of the $1/B_\perp$ axis around $(1/B_\perp) = 0$ in order to illustrate the positive phase shift $\Delta\nu^*$ of the oscillations before illumination.

In particular, the *maxima* coincided with the respective ν positions of an ideal 2DES rather than the zero crossings [see inset in Fig. 7.3 (a)]. Once the sample had been illuminated, the observed phase shift vanished. We found these results to be consistent for both samples #4069-1A and #3556-1, as summarized in Tab. 7.2.

In a further series of measurements, we addressed the temperature dependence of the dHvA oscillations for both samples. This was done by recording magnetization traces for different temperatures, ranging from $T = 0.28\,\mathrm{K}$ to $T = 15\,\mathrm{K}$, as depicted for sample #3556-1 in Fig. 7.4 (a). These measurements were only performed after illuminating the dot ensemble. In order to fit the Lifshitz-Kosevich model [c.f. Eq. (2.23)] to the data, we extracted the amplitudes ΔM for each visible ν^* and each value of T. From the curves shown in Fig. 7.4 (a), we found that the $M(B)$ were nearly identical for $T = 0.28\,\mathrm{K}$ and $T = 1.5\,\mathrm{K}$. It is therefore safe to identify $\Delta M(0.28\,\mathrm{K}) \approx \Delta M_0$, i.e., the amplitudes at base temperature were basically identical to the amplitudes ΔM_0 which

Table 7.2: Offset $\Delta\nu^*$ extracted from linear fits of $(1/B)$ maxima- and zero-crossing positions for the two investigated samples.

wafer		$\Delta\nu^*_{\mathrm{zero}}$	$\Delta\nu^*_{\mathrm{max}}$
#3556	dark	0.34 ± 0.06	-0.06 ± 0.07
	illuminated	0.06 ± 0.06	-0.13 ± 0.04
#4069	dark	0.27 ± 0.10	-0.16 ± 0.05
	illuminated	0.05 ± 0.03	-0.29 ± 0.04

would be observed at zero temperature. Following this, we plotted all extracted $\Delta M/\Delta M_0$ as a function of $x = (2\pi^2 m_0 k_{\mathrm{B}} T)/(\hbar e B_\perp)$ in Fig. 7.4 (b) and performed a least squares fit of the data by

$$\frac{\Delta M}{\Delta M_0} = \frac{\sinh(x\, m_{\mathrm{eff}})}{x\, m_{\mathrm{eff}}} \ . \tag{7.5}$$

Here, the reduced effective mass $m_{\mathrm{eff}} = m^*/m_0$ was used as a fit parameter. For sample #3556-1, we obtained a value of $m_{\mathrm{eff}} = 0.037 \pm 0.002$, which agrees perfectly with the value found for the reference 2DES. The identical analysis on sample #4069-1A revealed an increase of m_{eff} to 0.049 ± 0.003. However, the measured temperature dependencies are still comparable to the 2DES case; a significant change of $\Delta M(T)$ as reported for GaAs dots [Sch+02b] was not observed for the present InGaAs/InP dot mesa.

7.3 Comparison of simulation with experiment

In the following, we compare the experimental outcomes with predictions of the theoretical models introduced in 2.5. Here, we stress again that the simulations were made using a single particle picture, although our dots are populated by hundreds of electrons. Many-particle effects are phenomenologically included via a screening of the lateral confinement potential of an empty dot, thereby defining the shape of the *effective* potential that a single electron feels in the mean field of the remaining electrons. In the following, we use the term "confinement potential" to

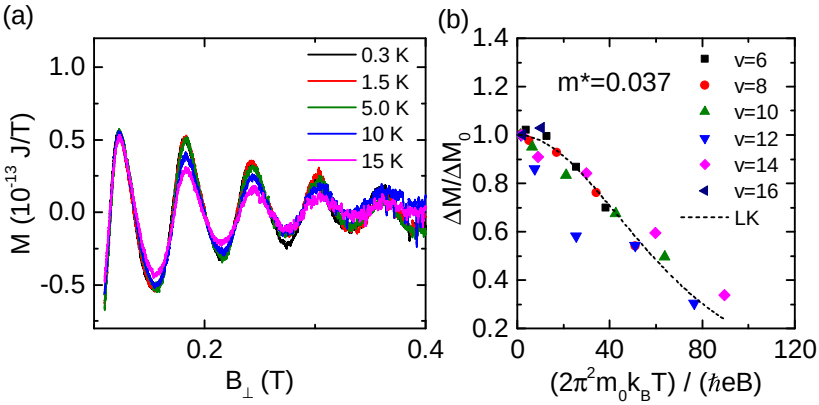

Figure 7.4: (a) Temperature dependence of $M(1/B_\perp)$ measured after illumination for sample #3556-1. (b) Normalized amplitudes of all visible filling factors as a function of $x = (2\pi^2 m_0 k_B T)/(\hbar e B_\perp)$. The dashed line represents a fit of the Lifshitz-Kosevich model to the data. The extracted effective mass yielded $m^* = 0.037 m_0$.

address this effective confinement potential. Moreover, for a realistic description of the experimental data, we discuss the effect of ensemble related broadening effects and include these into the modeling. From a detailed analysis of shape and periodicity of the dHvA-type oscillations predicted by the modeling, we argue that a hard wall confinement potential describes the data best and that the assumption of pure parabolic confinement is unrealistic for our dots with many electrons. Following these considerations, we use the HW model to fit the data quantitatively, thereby extracting relevant model parameters.

7.3.1 Ensemble broadening

The recorded magnetization traces can be understood as the sum signal of the magnetization produced by each individual dot. However, the dots are not completely identical. Across the ensemble, variations in the processing of the dots caused a systematic spread of the dot diameter of order $\Delta d/d \approx 2\%$, as confirmed by the analysis of SEM images. Furthermore a statistical donor distribution may induce changes of the

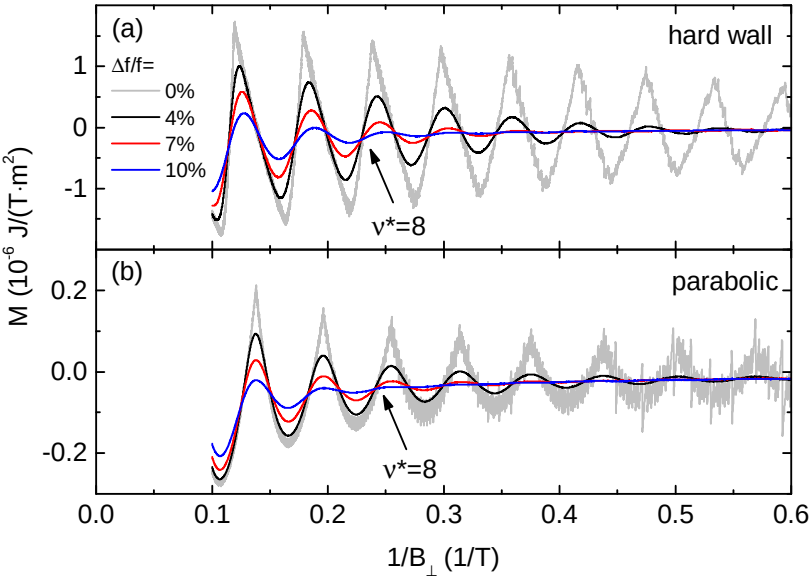

Figure 7.5: Simulated magnetization curves in case of (a) HW and (b) parabolic confinement. For each model, four curves were modeled with different broadening parameter $\Delta f/f$ of 0 %, 4 % 7 % and 10 %. The magnetization was normalized to the physical dot area of πR_0^2. A polynomial background was subtracted from the curves shown in (b). Simulation parameters were $N = 1350$, $R_0 = 230\,\mathrm{nm}$ and $\hbar\omega_0 = 1.52\,\mathrm{meV}$. The upward flanks corresponding to $\nu^* = 8$ are marked by arrows. Note the different magnetization scales in (a) and (b).

electron number N from dot to dot. These effects provoke a broadening of measured dHvA oscillations. Here, diameter variations translate directly into a variation of the parameters defining the respective model potential, i.e., ω_0 for parabolic and R_0 for HW confinement. Following the discussion in section 2.5, changes in R_0, ω_0 and N effectively change the *frequency* of the dHvA-type oscillations. Contributions that alter the *shape* of the potential such as randomly distributed impurities or donors that are unique for each dot were not included into our the

modeling. Following Eqs. (2.59) and (2.64) and assuming small changes ΔR_0, $\Delta\omega_0$, ΔN, we derive

$$\begin{aligned} \frac{\Delta f}{f} &\approx 2\frac{\Delta R_0}{R_0} \approx \frac{\Delta N}{N} \quad \text{(HW)} \qquad \text{and} \\ \frac{\Delta f}{f} &\approx \frac{\Delta\omega_0}{\omega_0} \approx \frac{1}{2}\frac{\Delta N}{N} \quad \text{(FD)}. \end{aligned} \tag{7.6}$$

Therefore, we included the combined effect of the statistical spread in (R_0, ω_0) and N into our modeling via a Gaussian distribution of dHvA frequencies f with standard deviation Δf around the average frequency $\bar{f}$:

$$\Phi(f, \bar{f}, \Delta f) = \frac{1}{\sqrt{2\pi}\Delta f} \exp\left[-\frac{(f-\bar{f})^2}{2\Delta f^2}\right] \tag{7.7}$$

where $\Phi(f, \bar{f}, \Delta f)$ denotes the relative amount of dots with frequency f.

In the following, we will compare simulated magnetization curves of HW and FD model for different values of the broadening parameter $\Delta f/f$. Simulations including the effect of ensemble broadening were performed by averaging over 1000 curves with Gaussian distributed parameters (R_0, ω_0) to reproduce the respective $\Delta f/f$, while keeping the number of electrons N fix. In a first approach, we neglected possible effects of edge depletion and estimated $N = n_{2D}\pi R_0^2 \approx 1350$. Here, we used the physical dot radius $R_0 = 230\,\text{nm}$ and the electron density $n_{2D} = 8.12 \times 10^{11}\,\text{cm}^{-2}$ as measured for the reference 2DES. The confinement energy in the FD model was set to $\hbar\omega_c = 1.52\,\text{meV}$ in order to reproduce a similar dHvA frequency as obtained for the HW model.

Figure 7.5 depicts ideal and broadened magnetization curves for (a) HW and (b) FD model. The curves were normalized to the total physical mesa area as it was done for the experimental traces in Fig. 7.2. The dHvA-type oscillations of the broadened curves are smoothed and reduced in amplitude. Furthermore, fast AB-type oscillations present at $\Delta f/f = 0$ are completely smeared out once broadening is included. This confirms the predictions of Sivan and Imry, who argued that the AB-type oscillations are randomly shifted and likely to be suppressed in large ensembles of dots [SI88]. We observe that the amplitudes ΔM of the dHvA-type oscillations fade out towards small fields. Moreover,

we identify that high filling factors are suppressed significantly upon increasing $\Delta f/f$. This behavior is expected because the envelope of the broadened curves is approximately given by the Fourier transform of the distribution $\Phi(f, 0, \Delta f)$, which is also a Gaussian function that gets narrower as $\Delta f/f$ increases. For our particular case, we find that for $\Delta f/f = 7$ %, oscillations for $\nu^* > 10$ are completely suppressed. However, in the experiment, we observe filling factors up to $\nu^* \approx 22$, which implies that the actual broadening in the experiment is small. As a consequence, the overall reduction of signal amplitude in the experiment cannot be explained broadening effects alone. Therefore, we conclude that the observed amplitude reduction is mainly due to the lateral confinement.

7.3.2 Analysis of FD and HW model curves

For a detailed analysis of amplitude, shape and periodicity of the dHvA-type oscillations predicted by HW and FD model, we extracted maxima, zero-crossing and minima positions for the relevant effective filling factors ν^*, as it was done for the experimental data. Therefore, we concentrated on the curves in Fig. 7.5 including a broadening of $\Delta f/f = 4$ %. The fading of the oscillation envelopes towards small $B_\perp$ for this particular broadening parameter agrees reasonably well with the experimental behavior and is consistent with the experimentally determined variation of the dot diameter.

We first consider the oscillation amplitudes ΔM. We find that the amplitudes predicted by the HW model are much larger than in the experiment. Quite in contrast, the dHvA amplitudes are highly suppressed for the FD model, which suits the experimental observation much better. However, if compared to the experimental curves after illumination, the predicted amplitudes by the FD model are too small. Second, we investigated the asymmetry and oscillation period in detail. Table 7.3 reports the asymmetry parameter $\Delta_{\mathrm{up}}/\Delta_{\mathrm{down}}$ as well as the period p_{ν^*} of the maxima positions for both models as a function of the effective filling factor ν^*. Evidently, the HW model predicts a significant asymmetry for small ν^*, approaching symmetric oscillations for larger ν^*, similar to the experimental observations after illumination. The FD model does not reveal any signatures of asymmetry, and $\Delta_{\mathrm{up}}/\Delta_{\mathrm{down}} \approx 1$ for all visible oscillations. Considering the oscillation period, we find

that the HW model predicts a constant p_{ν^*} for all ν^*, while a significant increase of p_{ν^*} on the order of ≈ 15 % is asserted for increasing ν^* for the FD model. This variation contradicts the experiment, where no deviation in p_{ν^*} was observed.

Table 7.3: Asymmetry parameter $\Delta_{\mathrm{up}}/\Delta_{\mathrm{down}}$ and period p_{ν^*} of the maxima positions extracted from the simulated HW and FD curves with 4 % broadening presented in Fig. 7.5.

ν^*	$\Delta_{\mathrm{up}}/\Delta_{\mathrm{down}}$		p_{ν^*} (1/T)	
	HW	FD	HW	FD
4	0.57	1.11	-	-
6	0.81	1.03	0.060	0.058
8	0.90	0.97	0.058	0.058
10	1.00	1.00	0.059	0.060
12	0.97	1.00	0.058	0.061
14	0.97	1.07	0.059	0.063
16	0.97	1.09	0.059	0.065

In order to account for possible phase shifts, we performed a fan chart analysis of minima, zero-crossing and maxima positions of the oscillations predicted by the HW model. This was done for the unbroadened curve [Fig. 7.6 (a)] as well as the broadened curve with $\Delta f/f = 4$ % [Fig. 7.6 (b)]. For the ideal HW model, the fitting reveals slightly different frequencies for the three position sets. This is because the shape of the oscillations changes from nearly sawtooth-like to a more symmetric shape for decreasing $B_\perp$. Regarding the phase offset $\Delta\nu^*$, we notice that both zero-crossing positions and maxima exhibit $\Delta\nu^*$ close to zero. Broadening produces a negative phase shift for the maxima [c.f. inset of Fig. 7.6 (b)]. The $\Delta\nu^*$ predicted by the broadened curve are in very good agreement with the experimental observations after illumination. A positive phase-shift for the zero-crossings and a negligible phase-shift for the maxima as observed experimentally before illumination, however, is not reproduced by the model.

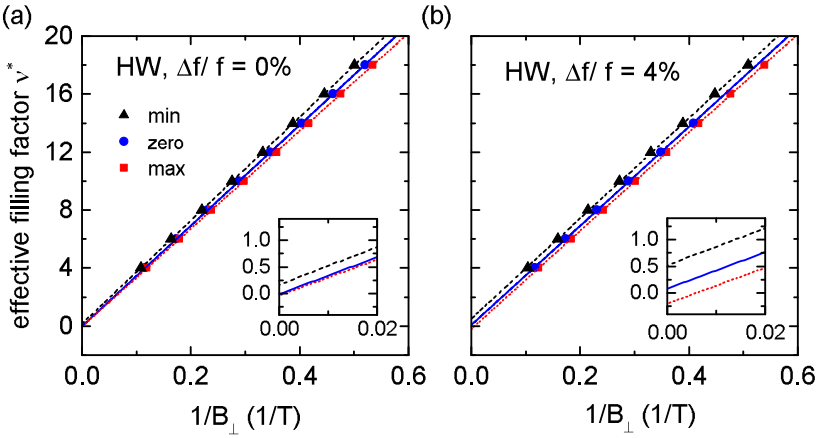

Figure 7.6: Fan charts of minima, zero-crossings and maxima field positions extracted from the HW model curves shown in Fig. 7.5 (a) without broadening (a) and with a broadening of 4 % (b). The insets show a blow-up of the diagrams around the origin to illustrate the phase-shifts $\Delta\nu^*$.

Performing the same fan-chart analysis for the FD model is not reasonable, because the field-dependent change in periodicity does not allow for a linear fit. Due to this fact, attempts to adjust the FD model parameters such that the model curve agreed quantitatively with the experimental data failed, because the positions of the oscillations never matched for all visible ν^* (not shown). Using Fogler's ansatz of LL bending (see 2.5.1), we investigated this further by calculating $M(B)$ assuming a potential with a concave or a convex parabola at the center and hard walls at the borders of the dot. None of these attempts could reproduce the phase shifts observed in the experiment before illumination. Hence, we state that any kind of curvature added to $V(r)$ does not account for the measured $\Delta\nu^*$ if treated in a single particle picture.

In summary at this point, we find that a HW model describes the experimental data convincingly in terms of asymmetry, periodicity and phase shifts of the dHvA-type oscillations. The FD model is not suited

to describe the experiment. In the following, we thus use the HW model to refine the simulations.

7.3.3 Fitting of HW model with experiment

Following the above analysis, the predicted oscillation amplitude of the HW model neglecting any depletion effect is far too large to match the experimental observations. A quantitative modeling of the data is only possible by assuming a reduced effective dot radius R_0. This strategy should preserve the basic shape of the oscillations while ΔM should decrease due to the reduced number of electrons per dot. For this, we adjusted the parameters R_0, N and $\Delta f/f$ such that the modeled curves agreed quantitatively with the experimental data. In detail, we paid attention that the model curves matched the measured amplitudes ΔM, their field dependence and the oscillation period. We performed the modeling for all experimental curves [i.e., $M(1/B_\perp)$ before and after illumination for both samples]. The resulting curves are shown in Fig. 7.7. We find that the shape and the amplitude of the simulated oscillations fit quite well to the experiment, especially for the illuminated curves. In general, the oscillations of the simulation fade out more quickly than the experimental ones. Slight deviations in the maxima positions stemming from the phase shift $\Delta\nu^*$ were most clearly observed for sample #3556-1 before illumination. Extracted fitting parameters are summarized in Tab. 7.4. The evaluated dot radius is on the order of $\approx 100\,\mathrm{nm}$. Considering the physical radius of the etched dots of 230 nm, a depletion length of $\approx 130\,\mathrm{nm}$ is extracted. After illumination, R_0 and N are found to increase and the broadening $\Delta f/f$ to be decreased.

7.4 Discussion

The presented analysis of experiment and simulation reveals that a parabolic potential is not suited to describe the data. Although this ansatz seems to explain the observed amplitude decrease of the dHvA-type oscillations in the first place, a closer look shows that the predicted amplitudes are too small. This is further underlined by the fact that the number of electrons $N = 1350$ used in the initial modeling can be understood as an upper limit, which assumes that all the donors

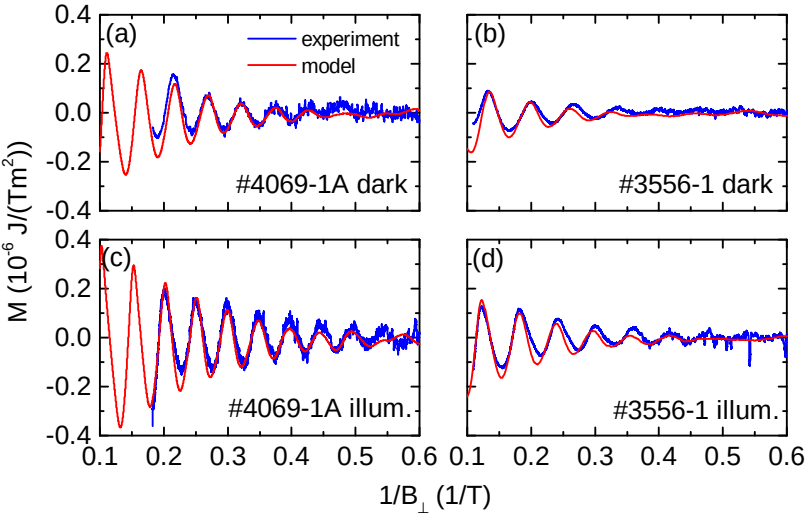

Figure 7.7: Simulated magnetization curves using the HW model (red) compared to the experimental $M(1/B_\perp)$ (blue) for both samples in both dark and illuminated states. The fit parameters R_0, N and $\Delta f/f$ are summarized in Tab. 7.4.

Table 7.4: Simulation parameters used to fit the HW model to the experimental data of both samples #3556-1 and #4069-1A before and after illumination. Parameters are N: number of electrons per dot, R_0: mean dot radius, $\Delta f/f$: ensemble broadening.

sample		N	R_0 (nm)	$\Delta f/f$ (%)
#3556-1	dark	180	90	4.4
	illuminated	250	100	3.6
#4069-1A	dark	330	110	2.8
	illuminated	430	120	1.6

within the physical borders of the dot are ionized. This assumption certainly overestimates N if the confinement potential is parabolic, because donors near the borders are likely to remain in a non-ionized state. A smaller N, however, would further reduce the dHvA amplitudes predicted by the parabolic model. Second, the asymmetry and strict periodicity of the observed oscillations is not in accordance with the parabolic model.

On the contrary, the asymmetry of the oscillations indicates that the effective confinement potential must be flat at least within a certain radius from the center of the dot. We argue that this is a result of effective screening of the initial confinement potential present for an empty dot. This is further substantiated by the observation of increasing asymmetry upon illuminating the sample. Screening becomes even more effective due to the increased N, thereby enhancing the flatness of the potential. These findings agree with earlier magnetization measurements in AlGaAs/GaAs etched quantum wires, where it was shown that the slopes of the negative flanks of dHvA oscillations, and consequently their asymmetry, reflected the amount of screening [Wil+04]. Self-consistent Schrödinger-Poisson calculations of 1D and 0D laterally confined 2DESs in AlGaAs/GaAs heterostructures revealed, that the potential flattened out at the center of the structures if populated by many electrons [LFS88; KLS90]. These findings suggest that a HW potential is a realistic ansatz to describe the underlying structure for dots if populated by many electrons and small interaction parameter r_S. The positive phase shift of the oscillations as observed before illumination is not reproduced in the modeling based on a single particle picture, independent on the flatness of the model potential. Due to the reduced N prior to illumination, electron-electron interaction effects might play a more important role. They would require an involved theoretical treatment which is beyond the scope of this work.

The effect of inhomogeneous broadening across the ensemble was included into the modeling via a Gaussian distribution of the dot radius R_0 (and thus the dHvA frequency $f_{1/B_\perp}$). The extracted broadening parameter $\Delta f/f$ decreases after illumination. This can be explained by a reduced statistical spread of N from dot to dot, thereby leading to a more homogeneous distribution of the effective radius R_0 across the ensemble. Still, the modeling of ensemble effects via a distribution of f is subject to some limitations. Each individual dot is treated as providing

an ideal HW magnetization signal. However, the reference 2DESs did not show ideal sawtooth-shaped dHvA oscillations but were also subject to lifetime broadening, as discussed in detail in 2.2.2. We attribute the different overall amplitude ΔM of wafers #4069 and #3556 to such effects. Since this difference in amplitude was also observed for the dots, we conclude that there are mechanisms accounting for an amplitude decrease for each individual dot which are not considered in the modeling. Such effects could include a variation of the potential shape from dot to dot, while having less influence on the dHvA frequency itself. Following this reasoning, the extracted $\Delta f/f$ are over-estimated, which in turn would explain that the fading of the dHvA oscillations towards small $B_\perp$ in the experiment is less pronounced than in the modeling. The smallest extracted broadening parameter amounts to $\Delta f/f = 1.6$ %. Following the previous discussion, this evidences that large arrays of dots were fabricated with high homogeneity in the course of this work.

From the analysis of the data, we concluded that the dots were subject to a substantial edge depletion of order $\approx 130\,\mathrm{nm}$. The key aspect for this finding was the overall decrease in dHvA amplitude ΔM per mesa area by a factor of ≈ 10 with respect to the 2DES reference. In particular, we argued that inhomogeneous broadening effects as discussed above could not explain this strong reduction alone, and a smaller effective radius of the confinement potential R_0 was crucial to describe the data convincingly. Although we found differences in the dHvA amplitudes for the two observed wafers, we stress that the *relative* change in ΔM from 2DES to dot ensemble was quite the same. Moreover, we found comparable effective R_0 for both dot samples, even though we used the *absolute* amplitudes in the analysis and did not account for these relative differences. These considerations support our conclusion that the reduction in ΔM is explained with edge depletion effects. Furthermore, and given that ensemble broadening effects are small, the finding of a maximum R_0 is substantiated by the observed fading of the oscillations towards small $B_\perp$. To explain this, we compare R_0 with the semiclassical cyclotron radius r_c at the Fermi level. For a given $B_\perp$, r_c is derived as [AM76]

$$r_c = \frac{\hbar k_\mathrm{F}}{eB_\perp} = \frac{\hbar\sqrt{2\pi n_\mathrm{2D}}}{eB_\perp} \,. \tag{7.8}$$

The observed dHvA oscillations vanished at $B_\perp \approx 2\,\mathrm{T}$. At this particular field, one obtains $r_c \approx 80\,\mathrm{nm}$ (with $n_{2\mathrm{D}} = 8.5 \times 10^{11}\,\mathrm{cm}^{-2}$). This agrees well with the simulated $R_0 \approx 100\,\mathrm{nm}$. In a semiclassical picture, dHvA oscillations at smaller $B_\perp$ are not expected because $r_c > R_0$ and electrons do not perform full cyclotron orbits. We fortify the hypothesis of edge depletion by further measurements that were performed on mesoscopic dot ensembles with dot diameters of $\approx 3\,\mu\mathrm{m}$ prepared from wafer #4069 (not shown). From the decrease in ΔM, we extracted an edge depletion width on the order of 200 nm for these samples.

The existence of a rather large edge depletion is in contrast to previous works, which claimed that for InGaAs-based lateral nanostructures, effective and geometrical widths were almost the same [Ker+90; Tem+87]. Kajiyama *et. al.* investigated the Schottky barrier height of $\mathrm{In}_x\mathrm{Ga}_{1-x}\mathrm{As}$ as a function of the In content x. They reported that for pure InAs, the barrier height was negative and the Fermi level was pinned *inside* the conduction band at a free surface [KMS73]. For the QW in our dots, the In content was $x = 0.77$, which still gives a positive barrier height on the order of 20 meV. However, since the Fermi level in our structures was of order 50 meV and the confinement potential was, as discussed above, effectively screened, the small theoretical barrier height cannot explain the relatively large edge depletion which we observed. Possible reasons for a depletion at the edges could be based on the fabrication processes via electron beam lithography and reactive ion etching. High-energetic electrons or ions may generate defects at the edges, which pin the Fermi level below the conduction band and counteract the formation of a surface accumulation layer. Moreover, the QW barrier layers are subject to an increased Schottky barrier height as compared to the QW itself. Notably, this applies to the InP spacer layer below the QW, exhibiting a barrier height on the order of 400 meV [WMR82]. Positive net charges at the lateral InP borders might push electrons away from the edges, thereby depleting the borders of the dots.

Finally, we discuss possible signatures of spin orbit coupling in the magnetization of the dot ensemble. As evident from measurements presented in chapter 5, the dHvA oscillations of the reference 2DES exhibited characteristic beating patterns due to a dominant Rashba term. These beatings were also reported in magnetotransport measurements on etched wire structures prepared from the same type of heterostructures. However, signatures of a beating or spin-splitting were not observed

in the dHvA oscillations of the present dot ensembles. Assuming that large dots with a HW potential would exhibit similar beating patterns, we discuss their observability in the following. First, we stress that the dHvA oscillations of the dot samples were suppressed for $\nu^* < 20$, whereas the beat node is expected near $\nu = 58$ for tilt angles θ in the range of 0° to 60°. Tilting the magnetic field towards the angle of half coincidence $\theta_c^{1/2}$ will shift the first beat node to higher magnetic fields (see 2.4.2). Nonetheless, a notable shift of the node beyond $\nu = 20$ requires θ to be *very* close to the $\theta_c^{1/2}$. Under these conditions, the envelopes of even and odd ν are almost constant as a function of $1/B_\perp$, which makes it practically impossible to identify an exact node position in the data.

We conclude that addressing possible beating patterns in $M(B)$ of quantum dots requires that the oscillations remain visible towards smaller $B_\perp$. Following the previous discussion, the fading of the oscillations is governed mainly by the effective dot radius R_0. Therefore, an enlargement of the dots might facilitate the detection of beat nodes in $M(B)$. Still, with increasing R_0, the effect of confinement might be weaker. Alternatively, the strength of SOI could be measured at high magnetic fields and very small filling factors due to avoided crossings of Landau- and Zeeman gaps at the full coincidence tilt angle θ_c^1 [WG13]. SOI in the energy spectra and the magnetization of small quantum dots with only few electrons have been discussed in numerous theoretical treatments [TLG04; CP05; PC06; CAC07; APC12]. Here, observation of magnetization steps related to single particle level crossings are crucial to reveal information about these energy spectra and the influence of SOI. Until now, no direct magnetization data of such dots with few electrons was published due to experimental challenges, originating from the small signal strength of a single quantum dot.[1]

[1] Direct access to energy states at the Fermi level can be gained via single electron tunneling. Oosterkamp et al. showed that the magnetization can be deduced indirectly from such tunneling data in few electron dots [Oos+98].

8 Summary and outlook

In this thesis, spin-orbit interaction (SOI) effects in InP/InGaAs-based two-dimensional electron systems (2DES) were investigated via beating patterns in the magneto-oscillations of magnetization M, chemical potential μ and magnetoresistance ρ_{xx}. Furthermore, magnetization measurements were employed to study confinement effects in laterally etched quantum dot ensembles prepared from the same InP/InGaAs heterostructures.

Experiments were performed at cryogenic temperatures and high magnetic fields B with adjustable tilt angles. Here, the thermodynamic quantities M and μ were experimentally addressed by means of torque cantilever magnetometry using both capacitive and interferometric readout schemes. The interferometric setup could be improved to substantially reduce the required laser power and sample temperature. Moreover, a novel technique was developed to address the chemical potential μ of gated 2DESs via a resonant excitation of the cantilevers, thereby featuring an enhanced resolution as opposed to the quasi-static measurement of M. For a detailed interpretation of the experimental results, all the recorded data were compared to theoretical simulations performed within the framework of this thesis. A modeling of 2DES energy spectra including both Rashba (R) and Dresselhaus (D) SOI mechanisms allowed to predict SOI-related beat node positions and enabled to extract relevant SOI parameters from the experiments. Furthermore, simulations of magnetization traces of quantum dots enabled to draw conclusions on confinement effects in the investigated samples.

In the following, the results obtained on gated 2DES flip-chip samples, 2DES Hall bar samples and quantum dot mesa are summarized an short outlook suggesting future investigations is given.

Magnetization and chemical potential of a 2DES with spin-orbit interaction

Simultaneous measurements of $M(B)$ and $\mu(B)$ were performed on contacted and gated 2DES flip-chip samples by means of cantilever magnetometry via a combined quasi-static operation and resonant excitation. Both M and μ exhibited beating patterns in $1/B$-periodic quantum oscillations which were attributed to SOI. While a single beat node was detected in $M(B)$, the enhancement of resolution in $\mu(B)$ due to resonant excitation enabled the detection of a second beat node. Model calculations of $M(B)$ and $\mu(B)$ showed that an accurate representation of the data was only possible by considering *both* R- and D-SOI. A fitting routine allowed to extract absolute values of the SOI constants α_R and β_D from the two beat node positions in $\mu(B)$. In addition to a dominant R-term, a small D-contribution $\beta_\mathrm{D} \approx 0.1\,\alpha_\mathrm{R}$ was asserted.

This analysis exceeded previous investigations of SOI-related beating patterns in similar samples, where only the R-contribution was considered in the modeling [Eng+97; Rup+13]. While the application of static gate voltages was not possible due to time drifts of the electron density n_2D, future experiments should aim to study the gate-controlled interplay between R and D effects in both M and μ. In combination with the persistent photo effect, the variation of the effective electric field $\mathcal{E}$ in the quantum well at constant n_2D should be feasible, enabling to investigate changes in α_R and possibly also β_D as a function of $\mathcal{E}$.

Furthermore, the simultaneous detection of M and μ allowed us to confirm the relation $\Delta M/N = \Delta\mu/B$ of the oscillation amplitudes for the present samples, as predicted for non-interacting electrons [Wie+97]. On the other hand, a field-dependent enhancement of ΔM over $\Delta\mu$ is expected in 2DESs with strong electron-electron interactions [Mei+01], but a direct experimental confirmation is lacking. The combined detection of M and μ as developed here is key to address these anomalies directly, enabling to study novel interaction and correlation effects in future experiments. Going beyond that, the technique enables the investigation of thermodynamic ground state properties of any 2DES that is gateable and is thus of potential to explore new phenomena in 2D materials, such as Dirac fermions in graphene.

Investigation of spin-orbit interaction by anisotropic magnetotransport

Magnetotransport measurements were performed on InP/InGaAs sample Hall bars as a function of an external magnetic field, where both polar and azimuthal tilt angles, θ and φ, were tuned separately. From Shubnikov-de Haas (SdH) oscillations at constant θ, anisotropies in the SOI-related beat node positions as a function of φ were asserted, which were attributed to the presence of both R and D-SOI mechanisms. Furthermore, experiments at large magnetic fields revealed an in-plane anisotropy in the coincidence tilt angle $\theta_c^{1/2}$, which was associated with an in-plane anisotropy of the effective $\overline{\overline{g}}^*$-tensor. With the help of model calculations including both SOI and $\overline{\overline{g}}^*$-tensor anisotropy in doubly tilted fields, an elaborate fitting procedure was performed to match experimental beat node positions as well as coincidence angles with theoretical predictions. This allowed to unambiguously extract both absolute values and the relative sign of SOI-constants α_R and β_D as well as the full in- and out-of-plane anisotropy of $\overline{\overline{g}}^*$ from the experimental data.

The method is straightforward in the sense that only well established magnetotransport measurements on standard Hall bars are employed in order to determine the SOI-constants. Complementary methods that are able to determine both SOI constants simultaneously mostly relied on rather involved pump-probe experiments [Mei+07], required nanopatterning [Sas+14] or provided only the ratio [Gan+04] or absolute values [Mil+03] of α_R and β_D. Furthermore, asymmetries in the effective $\overline{\overline{g}}^*$-tensor were often neglected, although they are relevant in experiments where external magnetic fields are involved to probe SOI effects. The analysis presented in this work revealed α_R, β_D *and* all components of $\overline{\overline{g}}^*$, therefore providing a more comprehensive picture of spin-related physics in semiconductors. Starting from these results, band structure calculations providing the subband wave function of the 2DES should enable to investigate the predicted interplay of R and D-SOI with the in-plane anisotropy of $\overline{\overline{g}}^*$ [KK93]. Moreover, a tuning of the out-of-plane electric field $\mathcal{E}$ via a gate electrode should not only change α_R (as demonstrated in Refs. [Eng+97; Nit+97; Gru00]), but also influence the components of $\overline{\overline{g}}^*$. Performing anisotropic magnetotransport experiments at different gate voltages should confirm this assumption and

allow to validate the respective predictions of $\mathbf{k}\cdot\mathbf{p}$-theory [KK93; Win03].

Magnetization of nanopatterned InGaAs/InP quantum dots

Torque magnetometry was performed on nanopatterned InP/InGaAs quantum dot ensembles with lateral diameter of $\approx 460\,\mathrm{nm}$. The experiments yielded $1/B$-periodic magneto-oscillations, which were substantially reduced in amplitude and faded out quickly towards small magnetic fields. The oscillations were modeled theoretically by a single-particle ansatz assuming lateral confinement potentials of parabolic as well as hard-wall (HW) shape and including ensemble broadening effects. A careful analysis of amplitude, periodicity, and shape of the oscillations revealed that a hard-wall confinement potential was suited best to describe the experimental data. The flatness of this potential at the center of the dots was explained with effective screening. Furthermore, it was found that ensemble broadening effects played a minor role in explaining the fading of the oscillations. The main effect was attributed to lateral confinement. Different from complementary investigations on InP/InGaAs-based nanotructures [Tem+87; Ker+90], our modeling revealed that the present dots were subject to a substantial edge depletion of $\approx 100\,\mathrm{nm}$. This finding was attributed to the processing of the dots. A detailed analysis of surface charges and self-consistent modeling could further clarify this aspect, thereby providing a more realistic shape of the confinement potential. The method presented here is thus suitable to study the electronic structure of quantum dots with many electrons in their equilibrium state and paves the way to investigate lateral confinement and electron-electron interaction effects such as screening.

Signatures of spin splitting were not observed in the experiments and it was argued that large magnetic fields and high tilt angles would be required to address these effects. However, SOI-related beating patterns would hardly be observable for the present dots, because the oscillations faded out too quickly. Future experiments aiming to address SOI should be performed on dots with enlarged diameter. To analyze the results of these experiments, numerical calculations including SOI should be performed for such large dots with many electrons. Intriguing physics is also expected from measurements of M on single dots with only few

electrons, where numerous theoretical predictions on the impact SOI of exist. Here, transitions between single particle states should be observable in $M(B)$, enabling direct access the underlying energy spectra and their modifications by SOI. However, addressing relevant magnetization signals on the order of 10^{-22} J/T still remains an experimental challenge.

In conclusion, spin-orbit interaction and confinement effects in semiconductor hetero- and nanostructures are subject of intensive research due to the rich physics and potential spintronics applications. In this thesis it was shown experimentally that beating patterns in magneto-oscillations of magnetization, chemical potential and magnetotransport of 2DESs, if performed in tilted fields, provide simultaneous access to Rashba and also Dresselhaus SOI-constants and the full anisotropy of the effective $\overline{\overline{g}}^*$-tensor. This technique provides a more comprehensive picture of the interplay of these mechanisms, which is key to design future spintronics devices. Furthermore, magnetization measurements on quantum dots that were prepared from the above heterostructures showed that the lateral confinement potential is effectively screened and allowed to quantify the amount of edge depletion. This enabled a more profound understanding of the electronic properties of quantum dots containing many electrons.

A Abbreviations & Symbols

Abbreviations

AB	Aharonov-Bohm
AlGaAs	aluminum gallium arsenide
AOM	acusto-optical modulator
APD	avalanche photo diode
BIA	bulk inversion asymmetry
2DES	two-dimensional electron system
dHvA	de Haas-van Alphen
D	Dresselhaus
DOS	density of states
FD	Fock-Darwin
GaAs	gallium arsenide
HW	hard-wall
InGaAs	indium gallium arsenide
InP	indium phosphide
LK	Lifshitz-Kosevich
LL	Landau level
LPF	low pass filter
MCM	micromechanical cantilever magnetometer
QW	quantum well
R	Rashba
SdH	Shubnikov-de Haas
SEM	scanning electron microscopy
SIA	structural inversion asymmetry
SOI	spin-orbit interaction

Symbols

$a, a^\dagger$	annihilation and creation operators
$\mathbf{A}$	vector potential
A_m	2DES mesa area
$\mathbf{B}$	external magnetic field
$\mathbf{B}_{\text{eff}}$	effective magnetic field
C	capacitance
$D(E)$	density of states
e	positive elementary charge
$\mathcal{E}$	electric field
E	energy
E_{F}	Fermi energy
E_n	energy of the n-th Landau level
$E_{n'}$	energy of SOI spin-split Landau levels
E_{nl}	single particle energies of a quantum dot
f	frequency
F	free energy
g^*	effective electron Landé factor (scalar)
$\overline{\overline{g}}^*$	effective electron Landé tensor (including angular anisotropies)
$\hbar$	$= h/(2\pi)$, reduced Planck constant
I	current
$\mathbf{k}$	electron wave vector
k_{B}	Boltzmann constant
k_{F}	Fermi wave vector
K_C, K_I, K_{dyn}	calibration constants of the cantilever magnetometer for capacitive, optical and dynamic readout schemes
l_B	magnetic length
m_0	free electron mass
m^*	effective electron mass

M	magnetization
ΔM	peak-to-peak de Haas-van Alphen amplitude
$n_{2\mathrm{D}}$	2D electron density
N	total number of electrons
N_L	degeneracy per unit area of spin-split Landau levels
p_{ν^*}	period of dHvA oscillations at filling factor ν^*
P	laser power
r	in-plane radial coordinate
r_{S}	interaction parameter
R	resistance
R_0	effective dot radius
T	temperature
U	voltage
V	confinement potential
$w(z)$	subband wave function
α_{R}	Rashba parameter
β_{D}	$k_\parallel$-linear Dresselhaus parameter
γ	bulk Dresselhaus parameter
Γ	level broadening
Δ_0	zero field spin splitting
Δ_s	spin splitting
$\Delta_{s,\mathrm{Z}}$	Zeeman splitting
$\Delta_{\mathrm{up}}/\Delta_{\mathrm{down}}$	asymmetry parameter of de Haas-van Alphen oscillations
ϵ_0	dielectric constant
θ	polar angle of the external magnetic field
θ_c^i	i-th coincidence angle
μ	chemical potential
$\Delta\mu$	peak-to-peak amplitude of the quantum oscillations of μ
$\mu_{\mathrm{B}}^{(*)}$	(effective) Bohr magneton
$\nu^{(*)}$	(effective) filling factor

$\boldsymbol{\pi}$	kinetic momentum operator
ρ	resistivity
$\boldsymbol{\sigma}$	spin operator
τ	torque
φ	in-plane angle of the external magnetic field
Φ_0	magnetic flux quantum
ω_c	cyclotron frequency
ω_0	eigenfrequency
$\square_{\parallel}$, $\square_{\perp}$	parallel or perpendicular components (with respect to the 2DES plane)

B Matrix elements and angle-dependent g^*-factor

In this appendix, a derivation of the matrix elements of the Hamiltonian H of a 2DES including Landau quantization, anisotropic Zeeman splitting as well as Rashba- and Dresselhaus-SOI contributions in tilted fields is given. First, we include the $k_\parallel$-linear SOI terms only. Supplemental contributions due to $k_\parallel$-cubic Dresselhaus term are discussed later on. Finally, we derive the angle-dependent scalar g^*-factor in the case where only the anisotropic Zeeman splitting is considered and SOI contributions are neglected.

B.1 Matrix elements including Zeeman splitting and k-linear SOI-terms

The problem is formulated as follows (c.f. chapter 2):

$$\begin{aligned} H &= H_0 + H_\mathrm{s} = H_0 + H_\mathrm{Z} + H_\mathrm{R} + H_\mathrm{D} \\ H_0 &= \frac{\boldsymbol{\pi}^2}{2m^*} \\ H_\mathrm{Z} &= \frac{1}{2}\mu_B \left[g_\perp \sigma_z B_\perp + g_\parallel (\sigma_x B_x + \sigma_y B_y) + g_{xy} (\sigma_x B_y + \sigma_y B_x) \right] \\ H_R &= \frac{\alpha_\mathrm{R}}{\hbar} (\sigma_x \pi_y - \sigma_y \pi_x) \\ H_D &= \frac{\beta_\mathrm{D}}{\hbar} (\sigma_x \pi_x - \sigma_y \pi_y) \end{aligned} \tag{B.1}$$

Here, H_0 is the orbital Hamiltonian of an ideal 2DES and H_Z, H_R, H_D are the Zeeman, Rashba and Dresselhaus contributions to H, respectively. We now search for non-zero matrix elements of H in terms of the eigenstates $|n, s_z\rangle$ of H_0, i.e., we derive $\langle m, s_z | H | n, s_z' \rangle$ ($n = 0, 1, 2, ...$,

$s_z = \pm$). Two quantum mechanical operators are present. The spin operator $\boldsymbol{\sigma} = (\sigma_x, \sigma_y, \sigma_z)$ acts on the two-componental spinor states $|\pm\rangle$ in the following way [Sch02]:

$$\begin{aligned} \sigma_x|+\rangle &= |-\rangle & \sigma_y|+\rangle &= \ \ \mathrm{i}|-\rangle & \sigma_z|+\rangle &= \ \ |+\rangle \\ \sigma_x|-\rangle &= |+\rangle & \sigma_y|-\rangle &= -\mathrm{i}|+\rangle & \sigma_z|-\rangle &= -|-\rangle \ . \end{aligned} \tag{B.2}$$

On the other hand, the kinetic momentum operator $\boldsymbol{\pi} = (\pi_x, \pi_y)$ acts on the orbital states $|n\rangle$. In order to determine the effect of $\boldsymbol{\pi}$ on these states, it is instructive to rewrite π_x and π_y in terms of annihilation and creation operators a and $a^\dagger$ (defined in 2.2.1)

$$\pi_x = \mathrm{i}\frac{\hbar}{\sqrt{2}l_B}(a^\dagger - a) \quad \text{and} \quad \pi_y = \frac{\hbar}{\sqrt{2}l_B}(a^\dagger + a) \ , \tag{B.3}$$

where $l_B = \sqrt{\hbar/(eB_\perp)}$ is the magnetic length. This enables to use the following relations

$$a|n\rangle = \sqrt{n}|n-1\rangle \quad \text{and} \quad a^\dagger|n\rangle = \sqrt{n+1}|n+1\rangle \ . \tag{B.4}$$

With Eqs. (B.2), (B.3) and (B.4), we now have all ingredients at hand to calculate the respective matrix elements.

We start with the Zeeman contribution H_Z. This Hamiltonian contains only the components of the spin operator and does not act on orbital states. Therefore, only states with identical orbital quantum number n are coupled ($\langle m|n\rangle = \delta_{mn}$). Furthermore, it is clear from Eq. (B.2) that σ_z couples spinor states with $s_z = s_z'$ while σ_x, σ_z couple states with anti-parallel spin orientation ($s_z = -s_z'$). We find that the only non-zero matrix elements due to H_Z are:

$$\begin{aligned} \langle n, \pm|H_\mathrm{Z}|n, \pm\rangle &= \pm\frac{1}{2}\mu_B g_\perp B_\perp \\ \langle n, -|H_\mathrm{Z}|n, +\rangle &= \frac{1}{2}\mu_B\left[B_x(g_\parallel + \mathrm{i}g_{xy}) + B_y(g_{xy} + \mathrm{i}g_\parallel)\right] \end{aligned} \tag{B.5}$$

Here, we did not list the third element $\langle n, +|H_\mathrm{Z}|n, -\rangle$ which is simply given by the Hermitian conjugate of $\langle n, -|H_\mathrm{Z}|n, +\rangle$.

Using Eq. (B.3), the Rashba contribution H_R is rewritten as

$$H_\mathrm{R} = \frac{\alpha_\mathrm{R}}{\sqrt{2}l_B}\left[\sigma_x(a^\dagger + a) - \mathrm{i}\sigma_y(a^\dagger - a)\right] . \tag{B.6}$$

Likewise, the Dresselhaus term H_D is expressed as:

$$H_\mathrm{D} = \frac{\beta_\mathrm{D}}{\sqrt{2}l_B}\left[\mathrm{i}\sigma_x(a^\dagger - a) - \sigma_y(a^\dagger + a)\right] . \tag{B.7}$$

We notice that both terms contain products of a or $a^\dagger$ with one of the in-plane spin operators σ_x or σ_y. Consequently, these Hamiltonians couple only states with neighboring orbital quantum numbers $m = n \pm 1$ and with anti-parallel spin orientation $s_z = -s'_z$. Using Eqs. (B.2) and (B.4), we find that the only non-zero matrix elements (plus their Hermitian conjugates) yield

$$\begin{aligned}\langle n, +|H_\mathrm{R}|n+1, -\rangle &= \frac{\sqrt{2}\alpha_\mathrm{R}}{l_B}\sqrt{(n+1)} \\ &= \alpha_\mathrm{R}\sqrt{\frac{2eB_\perp(n+1)}{\hbar}} \end{aligned} \tag{B.8}$$

$$\begin{aligned}\langle n, -|H_\mathrm{D}|n+1, +\rangle &= -\mathrm{i}\frac{\sqrt{2}\beta_\mathrm{D}}{l_B}\sqrt{(n+1)} \\ &= -\mathrm{i}\beta_\mathrm{D}\sqrt{\frac{2eB_\perp(n+1)}{\hbar}} . \end{aligned} \tag{B.9}$$

If we are interested only in the energy states near the Fermi level E_F, we can use the approximation $E_\mathrm{F} \approx n\hbar\omega_c$ and $n+1 \approx n$ if n is sufficiently large [DDR90]. This allows us to simplify

$$\sqrt{\frac{2eB_\perp(n+1)}{\hbar}} \approx \sqrt{\frac{2m^*E_\mathrm{F}}{\hbar^2}} = k_\mathrm{F} \tag{B.10}$$

with the Fermi wave vector k_F. Therefore, the matrix elements (B.8) and (B.9) yield $\alpha_\mathrm{R}k_\mathrm{F}$ and $-\mathrm{i}\beta_\mathrm{D}k_\mathrm{F}$, respectively.

B.2 Matrix elements due to k-cubic Dresselhaus terms

From Eq. (2.37) it is clear that in a 2DES the Dresselhaus-SOI actually contributes two distinct terms to H_{D}, namely

$$\begin{aligned} H_{\mathrm{D}} &= H_{\mathrm{D},1} + H_{\mathrm{D},2} \\ H_{\mathrm{D},1} &= -\frac{\gamma}{\hbar^3}\langle\pi_z^2\rangle(\sigma_x\pi_x - \sigma_y\pi_y) \\ H_{\mathrm{D},2} &= \frac{\gamma}{\hbar^3}(\sigma_x\pi_y\pi_x\pi_y - \sigma_y\pi_x\pi_y\pi_x)\,. \end{aligned} \tag{B.11}$$

Here, γ is the bulk Dresselhaus parameter and $\langle\pi_z^2\rangle$ is the expectation value of the z-component of $\boldsymbol{\pi}$ as determined by the (fixed) subband wave function $w(z)$. Different from Eq. (2.45), we already replaced the components of the wave vector operator by those of the kinetic momentum operator $k_i = \pi_i\hbar$. The $k_\parallel$-linear contribution $H_{\mathrm{D},1}$ was included in (B.1) (using $\beta_{\mathrm{D}} = -\gamma\langle k_z^2\rangle$), while $H_{\mathrm{D},2}$, which is cubic in $k_\parallel$, was omitted previously. In order to derive the matrix elements due to $H_{\mathrm{D},2}$, we again replace π_x, π_y by their notations in terms of a and $a^\dagger$:

$$\begin{aligned} H_{\mathrm{D},2} = \frac{\gamma}{(\sqrt{2}\,l_B)^3}\big[&\mathrm{i}\sigma_x(a^\dagger + a)(a^\dagger - a)(a^\dagger + a) \\ &+\sigma_y(a^\dagger - a)(a^\dagger + a)(a^\dagger - a)\big] \end{aligned} \tag{B.12}$$

Using the commutator relation $[a, a^\dagger] = 1$, Eq. (B.12) can be rewritten:

$$\begin{aligned} H_{\mathrm{D},2} = \frac{\gamma}{(\sqrt{2}\,l_B)^3}\Big[&\mathrm{i}\sigma_x\Big((a^\dagger)^3 + a^\dagger(1+\hat{N}) + a(1-\hat{N}^*) - a^3\Big) \\ &+\sigma_y\Big((a^\dagger)^3 - a^\dagger(1+\hat{N}) + a(1-\hat{N}^*) + a^3\Big)\Big] \end{aligned} \tag{B.13}$$

Here, we introduced the number operators $\hat{N} = a^\dagger a$ and $\hat{N}^* = aa^\dagger$, which do not change the orbital states $|n\rangle$ and return the angular quantum numbers as $\hat{N}|n\rangle = n|n\rangle$ and $\hat{N}^*|n\rangle = (n+1)|n\rangle$. Apparently, $H_{\mathrm{D},2}$ contains products of σ_x or σ_y with either a, $a^\dagger$ or a^3, $(a^\dagger)^3$. Hence, only states with anti-parallel spin orientation and with orbital quantum

numbers $m = n + 1$ or $m = n + 3$ are coupled. Using Eqs. (B.2) and (B.4), we find that the non-vanishing matrix elements due to $H_{\mathrm{D},2}$ are

$$\begin{aligned}\langle n,-|H_{\mathrm{D},2}|n+1,+\rangle &= -\mathrm{i}\frac{\gamma}{\sqrt{2}l_B^3}(n+1)^{3/2} \\ &\approx -\mathrm{i}\frac{\gamma}{4}k_{\mathrm{F}}^3 \\ \langle n,+|H_{\mathrm{D},2}|n+3,-\rangle &= -\mathrm{i}\frac{\gamma}{\sqrt{2}l_B^3}\sqrt{(n+1)(n+2)(n+3)} \\ &\approx -\mathrm{i}\frac{\gamma}{4}k_{\mathrm{F}}^3\end{aligned} \tag{B.14}$$

plus their Hermitian conjugates. Here, the final approximations are based on (B.10). In summary, the matrix elements due to H_{D} including both $k_\parallel$-linear and $k_\parallel$-cubic terms read

$$\begin{aligned}\langle n,-|H_{\mathrm{D}}|n+1,+\rangle &\approx \mathrm{i}\gamma\langle k_z^2\rangle k_{\mathrm{F}} - \mathrm{i}\frac{\gamma}{4}k_{\mathrm{F}}^3 := -\mathrm{i}\beta_{\mathrm{D}}' k_{\mathrm{F}} \\ \langle n,+|H_{\mathrm{D}}|n+3,-\rangle &\approx -\mathrm{i}\frac{\gamma}{4}k_{\mathrm{F}}^3\ ,\end{aligned} \tag{B.15}$$

where a corrected linear Dresselhaus constant was defined as $\beta_{\mathrm{D}}' := -\gamma\big(\langle k_z^2\rangle - {}^1\!/_4 k_{\mathrm{F}}^2\big)$.

B.3 Diagonalization of H with anisotropic Zeeman splitting

We consider the Hamiltonian H [Eq. (B.1)] without SOI terms and including only the anisotropic Zeeman terms. The aim is to derive the angle-dependent scalar g^*-factor by determining the spin-splitting from the respective energy eigenvalues. Neglecting SOI contributions, H decomposes into a 2×2 block-diagonal form, which allows for a straightforward diagonalization:

$$H_{2\times 2} = \begin{bmatrix} E_n - Z_\perp & Z_\parallel \\ Z_\parallel^* & E_n + Z_\perp \end{bmatrix}. \tag{B.16}$$

Here, $E_n = (n + 1/2)\hbar\omega_c$, $Z_\parallel = 1/2\mu_B\left[B_x(g_\parallel + \mathrm{i}g_{xy}) + B_y(g_{xy} + \mathrm{i}g_\parallel)\right]$ and $Z_\perp = \frac{1}{2}\mu_B g_\perp B_\perp$ were replaced for the sake of readability. Due to the Zeeman terms $Z_\perp$ and $Z_\parallel$, the formerly spin-degenerate Landau level with energy E_n splits up into two levels $E_{n,\pm}$, given by the eigenvalues of $H_{2\times2}$:

$$\begin{aligned} E_{n,\pm} &= E_n \pm \sqrt{Z_\perp^2 + |Z_\parallel|^2} \\ &= E_n \pm \frac{1}{2}\mu_B \sqrt{g_\perp^2 B_\perp^2 + (B_x^2 + B_y^2)(g_\parallel^2 + g_{xy}^2) + 4B_x B_y g_\parallel g_{xy}} \end{aligned} \tag{B.17}$$

Using polar coordinates to represent the external magnetic field $\mathbf{B}$

$$\begin{aligned} B_x &= B\sin\theta\cos\varphi \\ B_y &= B\sin\theta\sin\varphi \\ B_z &= B\cos\theta\ , \end{aligned} \tag{B.18}$$

the $E_{n,\pm}$ can be written in terms of θ and φ:

$$E_{n,\pm} = E_n \pm \frac{1}{2}\mu_B B\sqrt{g_\perp^2\cos^2\theta + (g_\parallel^2 + g_{xy}^2)\sin^2\theta + 2g_\parallel g_{xy}\sin^2\theta\sin 2\varphi} \tag{B.19}$$

$$E_{n,\pm} = E_n \pm \frac{1}{2}\mu_B B\, g^*(\theta,\varphi)\ . \tag{B.20}$$

Therefore, the Zeeman splitting $\Delta_{s,\mathrm{Z}} = E_{n,+} - E_{n,-}$ at constant B depends on the direction of $\mathbf{B}$ and a scalar, but angle-dependent $g^*(\theta,\phi)$ can be introduced.

List of Tables

Bibliography

[AF07] D. D. Awschalom and M. E. Flatte, "Challenges for semiconductor spintronics", Nat. Phys. **3**, 153–159 (2007).

[AM76] N. W. Ashcroft and N. D. Mermin, *Solid state physics*, Science: Physics (Saunders College, 1976).

[And92] E. A. de Andrada e Silva, "Conduction-subband anisotropic spin splitting in III-V semiconductor heterojunctions", Phys. Rev. B **46**, 1921–1924 (1992).

[APC12] S. Avetisyan, P. Pietiläinen, and T. Chakraborty, "Strong enhancement of Rashba spin-orbit coupling with increasing anisotropy in the Fock-Darwin states of a quantum dot", Phys. Rev. B **85**, 153301 (2012).

[AU74] T. Ando and Y. Uemura, "Theory of Quantum Transport in a Two-Dimensional Electron System under Magnetic Fields. I. Characteristics of Level Broadening and Transport under Strong Fields", J. Phys. Soc. Jpn. **36**, 959–967 (1974).

[Bai+88] M. N. Baibich, J. M. Broto, A. Fert, F. Nguyen Van Dau, F. Petroff, P. Etienne, G. Creuzet, A. Friederich, and J. Chazelas, "Giant Magnetoresistance of (001)Fe/(001)Cr Magnetic Superlattices", Phys. Rev. Lett. **61**, 2472–2475 (1988).

[Bal+11] A. Balocchi, Q. H. Duong, P. Renucci, B. L. Liu, C. Fontaine, T. Amand, D. Lagarde, and X. Marie, "Full Electrical Control of the Electron Spin Relaxation in GaAs Quantum Wells", Phys. Rev. Lett. **107**, 136604 (2011).

[Bin+89] G. Binasch, P. Grünberg, F. Saurenbach, and W. Zinn, "Enhanced magnetoresistance in layered magnetic structures with antiferromagnetic interlayer exchange", Phys. Rev. B **39**, 4828–4830 (1989).

[BR84a] Y. A. Bychkov and E. I. Rashba, "Oscillatory effects and the magnetic susceptibility of carriers in inversion layers", J. Phys. C Solid State **17**, 6039 (1984).

[BR84b] Y. A. Bychkov and E. I. Rashba, "Properties of a 2D electron gas with lifted spectral degeneracy", JETP Letters **39**, 78 (1984).

[Bru+10] C. Brune, A. Roth, E. G. Novik, M. Konig, H. Buhmann, E. M. Hankiewicz, W. Hanke, J. Sinova, and L. W. Molenkamp, "Evidence for the ballistic intrinsic spin Hall effect in HgTe nanostructures", Nat. Phys. **6**, 448–454 (2010).

[BSH08] A. C. Bleszynski-Jayich, W. E. Shanks, and J. G. E. Harris, "Noise thermometry and electron thermometry of a sample-on-cantilever system below 1Kelvin", Appl. Phys. Lett. **92**, 013123, 013123 (2008).

[CAC07] H.-Y. Chen, V. Apalkov, and T. Chakraborty, "Spin-orbit coupling and tunneling current in a parabolic quantum dot", Phys. Rev. B **75**, 193303 (2007).

[CCN92] M. Chaparala, O. H. Chung, and M. J. Naughton, "Capacitance platform magnetometer for thin film and small crystal superconductor studies", AIP Conf. Proc. **273**, 407–413 (1992).

[Cha12] S.-H. Chalkidis, "Anomalous magnetic oscillations observed on epitaxial graphene on silicon carbide", Diplomarbeit (Technische Universität München, 2012).

[Cha92] T. Chakraborty, "Physics of Artificial Atoms: Quantum Dots in a Magnetic Field", Comments on Condensed Matter Physics **16**, 35–68 (1992).

[CP05] T. Chakraborty and P. Pietiläinen, "Optical Signatures of Spin-Orbit Interaction Effects in a Parabolic Quantum Dot", Phys. Rev. Lett. **95**, 136603 (2005).

[CTA87] K. K. Choi, D. C. Tsui, and K. Alavi, "Experimental determination of the edge depletion width of the two-dimensional electron gas in GaAs/Al_xGa_{1-x}", Appl. Phys. Lett. **50**, 110–112 (1987).

[Dar31] C. G. Darwin, "The Diamagnetism of the Free Electron", Math. Proc. Cambridge **27**, 86–90 (1931).

[Das+89] B. Das, D. C. Miller, S. Datta, R. Reifenberger, W. P. Hong, P. K. Bhattacharya, J. Singh, and M. Jaffe, "Evidence for spin splitting in $In_xGa_{1-x}As/In_{0.52}Al_{0.48}As$ heterostructures as $B \to 0$", Phys. Rev. B **39**, 1411–1414 (1989).

[DD90] S. Datta and B. Das, "Electronic analog of the electro-optic modulator", Appl. Phys. Lett. **56**, 665–667 (1990).

[DDR90] B. Das, S. Datta, and R. Reifenberger, "Zero-field spin splitting in a two-dimensional electron gas", Phys. Rev. B **41**, 8278–8287 (1990).

[Des+04] W. Desrat, F. Giazotto, V. Pellegrini, F. Beltram, F. Capotondi, G. Biasiol, L. Sorba, and D. K. Maude, "Magnetotransport in high-g-factor low-density two-dimensional electron systems confined in $In_{0.75}Ga_{0.25}As/In_{0.75}Al_{0.25}As$ quantum wells", Phys. Rev. B **69**, 245324 (2004).

[Dir28] P. A. M. Dirac, "The Quantum Theory of the Electron", P. Roy. Soc. Lond. A Mat. **117**, 610–624 (1928).

[DLS04] L. G. G. V. Dias da Silva, C. H. Lewenkopf, and N. Studart, "Orbital magnetic properties of quantum dots: The role of electron-electron interactions", Phys. Rev. B **69**, 075311 (2004).

[Dol+97] V. T. Dolgopolov, A. A. Shashkin, A. V. Aristov, D. Schmerek, W. Hansen, J. P. Kotthaus, and M. Holland, "Direct Measurements of the Spin Gap in the Two-Dimensional Electron Gas of AlGaAs-GaAs Heterojunctions", Phys. Rev. Lett. **79**, 729–732 (1997).

[DP72] M. I. Dyakonov and V. I. Perel, "Spin relaxation of conduction electrons in noncentrosymmetric semiconductors", Sov. Phys. Solid State **13**, 3023–3026 (1972).

[Dre55] G. Dresselhaus, "Spin-Orbit Coupling Effects in Zinc Blende Structures", Phys. Rev. **100**, 580–586 (1955).

[Eis85] J. P. Eisenstein, "High-precision torsional magnetometer: Application to two-dimensional electron systems", Applied Physics Letters **46**, 695–696 (1985).

[Eld+11] P. S. Eldridge, J. Hübner, S. Oertel, R. T. Harley, M. Henini, and M. Oestreich, "Spin-orbit fields in asymmetric (001)-oriented GaAs/$Al_xGa_{1-x}As$ quantum wells", Phys. Rev. B **83**, 041301 (2011).

[Eli+04] P. Eliáš, I. Kostič, J. Šoltýs, and S. Hasenöhrl, "Wet-etch bulk micromachining of (100) InP substrates", Journal of Micromechanics and Microengineering **14**, 1205 (2004).

[Eli+99] P. Eliáš, V. Cambel, S. Hasenöhrl, P. Hudek, and J. Novák, "SEM and AFM characterisation of high-mesa patterned InP substrates prepared by wet etching", Materials Science and Engineering: B **66**, 15–20 (1999).

[Eng+82] T. Englert, D. C. Tsui, A. C. Gossard, and C. Uihlein, "g-Factor enhancement in the 2D electron gas in GaAs/AlGaAs heterojunctions", Surf. Sci. **113**, 295–300 (1982).

[Eng+97] G. Engels, J. Lange, T. Schäpers, and H. Lüth, "Experimental and theoretical approach to spin splitting in modulation-doped $In_xGa_{1-x}As/InP$ quantum wells for B→0", Phys. Rev. B **55**, R1958–R1961 (1997).

[EPW94] J. P. Eisenstein, L. N. Pfeiffer, and K. W. West, "Compressibility of the two-dimensional electron gas: Measurements of the zero-field exchange energy and fractional quantum Hall gap", Phys. Rev. B **50**, 1760–1778 (1994).

[Fan+11] S. Faniel, T. Matsuura, S. Mineshige, Y. Sekine, and T. Koga, "Determination of spin-orbit coefficients in semiconductor quantum wells", Phys. Rev. B **83**, 115309 (2011).

[FLS94] M. M. Fogler, E. I. Levin, and B. I. Shklovskii, "Chemical potential and magnetization of a Coulomb island", Phys. Rev. B **49**, 13767–13775 (1994).

[Foc28] V. Fock, "Bemerkung zur Quantelung des harmonischen Oszillators im Magnetfeld", Z. Phys. **47**, 446–448 (1928).

[Gan+04] S. D. Ganichev, V. V. Bel'kov, L. E. Golub, E. L. Ivchenko, P. Schneider, S. Giglberger, J. Eroms, J. De Boeck, G. Borghs, W. Wegscheider, D. Weiss, and W. Prettl, "Experimental Separation of Rashba and Dresselhaus Spin Splittings in Semiconductor Quantum Wells", Phys. Rev. Lett. **92**, 256601 (2004).

[GFR85] S. Gopalan, J. K. Furdyna, and S. Rodriguez, "Inversion asymmetry and magneto-optical selection rules in *n*-type zinc-blende semiconductors", Phys. Rev. B **32**, 903–913 (1985).

[GM03] C. Gerthsen and D. Meschede, *Gerthsen Physik*, Springer-Lehrbuch (Springer, 2003).

[GPD90] F. Geerinckx, F. M. Peeters, and J. T. Devreese, "Effect of the confining potential on the magneto-optical spectrum of a quantum dot", J. Appl. Phys. **68**, 3435–3438 (1990).

[Gru00] D. Grundler, "Large Rashba Splitting in InAs Quantum Wells due to Electron Wave Function Penetration into the Barrier Layers", Phys. Rev. Lett. **84**, 6074–6077 (2000).

[Gru02] D. Grundler, "Spintronics", Physics World **15**, 39 (2002).

[GS22] W. Gerlach and O. Stern, "Der experimentelle Nachweis der Richtungsquantelung im Magnetfeld", Z. Phys. **9**, 349–352 (1922).

[Gui+00] Y. S. Gui, C. M. Hu, Z. H. Chen, G. Z. Zheng, S. L. Guo, J. H. Chu, J. X. Chen, and A. Z. Li, "Spin splitting in pseudomorphic $In_xGa_{1-x}As/In_yAl_{1-y}As$ graded heterostructures", Phys. Rev. B **61**, 7237–7240 (2000).

[HA30] W. de Haas and P. van Alphen, "The dependence of the susceptibility of diamagnetic metals upon the field", Proc. Netherlands Roy. Adad. Sci. **33**, 1106 (1930).

[Hal79] E. H. Hall, "On a New Action of the Magnet on Electric Currents", American Journal of Mathematics **2**, 287–292 (1879).

[Har+93] H. Hardtdegen, R. Meyer, M. Hollfelder, T. Schäpers, J. Appenzeller, H. Løken-Larsen, T. Klocke, C. Dieker, B. Lengeler, H. Lüth, and W. Jäger, "Optimization of modulation-doped $Ga_{1-x}In_xAs/InP$ heterostructures towards extremely high mobilities", J. Appl. Phys. **73**, 4489–4493 (1993).

[Har+99] J. G. E. Harris, D. D. Awschalom, F. Matsukura, H. Ohno, K. D. Maranowski, and A. C. Gossard, "Integrated micromechanical cantilever magnetometry of $Ga_{1-x}Mn_xAs$", Appl. Phys. Lett. **75**, 1140–1142 (1999).

[Ho+10] L. H. Ho, L. J. Taskinen, A. P. Micolich, A. R. Hamilton, P. Atkinson, and D. A. Ritchie, "Electrometry using the quantum Hall effect in a bilayer two-dimensional electron system", Appl. Phys. Lett. **96**, 212102 (2010).

[Hol+06] A. W. Holleitner, V. Sih, R. C. Myers, A. C. Gossard, and D. D. Awschalom, "Suppression of Spin Relaxation in Submicron InGaAs Wires", Phys. Rev. Lett. **97**, 036805 (2006).

[Hol11] A. W. Holleitner, "Spin Relaxation: From 2D to 1D", in *Cfn lectures on functional nanostructures - volume 2*, Vol. 820, edited by M. Vojta, C. Röthig, and G. Schön, Lecture Notes in Physics (Springer Berlin Heidelberg, 2011), pp. 145–153.

[Ibr13] A. Ibrahim, "Simultaneously measured Shubnikov-de Haas and de Haas-van Alphen effect in a two-dimensional electron system with strong spin-orbit coupling", Master's thesis (Technische Universität München, 2013).

[IK92] E. L. Ivchenko and A. A. Kiselev, "Electron g factor of quantum wells and superlattices", Sov. Phys. Semicond. **26**, 827 (1992).

[Jan+11] J. Jang, D. G. Ferguson, V. Vakaryuk, R. Budakian, S. B. Chung, P. M. Goldbart, and Y. Maeno, "Observation of Half-Height Magnetization Steps in Sr_2RuO_4", Science **331**, 186–188 (2011).

[JBM11] J. Jang, R. Budakian, and Y. Maeno, "Phase-locked cantilever magnetometry", Appl. Phys. Lett. **98**, 132510, 132510 (2011).

[KDP80] K. v. Klitzing, G. Dorda, and M. Pepper, "New method for high-accuracy determination of the fine-structure constant based on quantized hall resistance", Phys. Rev. Lett. **45**, 494–497 (1980).

[Ker+90] K. Kern, T. Demel, D. Heitmann, P. Grambow, K. Ploog, and M. Razeghi, "One-dimensional electronic systems in ultra-fine mesa etched InGaAs-InAlAs-InP quantum wires", Surf. Sci. **229**, 256–259 (1990).

[Kim+12] S. Kim, I. Jo, D. C. Dillen, D. A. Ferrer, B. Fallahazad, Z. Yao, S. K. Banerjee, and E. Tutuc, "Direct Measurement of the Fermi Energy in Graphene Using a Double-Layer Heterostructure", Phys. Rev. Lett. **108**, 116404 (2012).

[KK93] V. K. Kalevich and V. L. Korenev, "Electron g-factor anisotropy in asymmetric GaAs/AlGaAs quantum well", JETP Lett. **57**, 571 (1993).

[KLS90] A. Kumar, S. E. Laux, and F. Stern, "Electron states in a GaAs quantum dot in a magnetic field", Phys. Rev. B **42**, 5166–5175 (1990).

[KMS73] K. Kajiyama, Y. Mizushima, and S. Sakata, "Schottky barrier height of n-$In_xGa_{1-x}As$ diodes", Appl. Phys. Lett. **23**, 458–459 (1973).

[KN00] A. V. Khaetskii and Y. V. Nazarov, "Spin relaxation in semiconductor quantum dots", Phys. Rev. B **61**, 12639–12642 (2000).

[Kno04] J. Knobbe, "Rashba-Effekt in niedrigdimensionalen InGaAs/InP Strukturen", Dissertation (RWTH Aachen, 2004).

[Koh+12] M. Kohda, S. Nakamura, Y. Nishihara, K. Kobayashi, T. Ono, J. Ohe, Y. Tokura, T. Mineno, and J. Nitta, "Spin–orbit induced electronic spin separation in semiconductor nanostructure", Nat. Commun. **3**, 1082 (2012).

[Kow+94] B. Kowalski, P. Omling, B. K. Meyer, D. M. Hofmann, C. Wetzel, V. Härle, F. Scholz, and P. Sobkowicz, "Conduction-band spin splitting of type-I $Ga_xIn_{1-x}As$/InP quantum wells", Phys. Rev. B **49**, 14786–14789 (1994).

[Kri+15] S. S. Krishtopenko, K. V. Maremyanin, K. P. Kalinin, K. E. Spirin, V. I. Gavrilenko, N. V. Baidus, and B. N. Zvonkov, "Exchange enhancement of the electron g factor in strained InGaAs/InP heterostructures", Semiconductors **49**, 191–198 (2015).

[KS05] J. Knobbe and T. Schäpers, "Magnetosubbands of semiconductor quantum wires with Rashba spin-orbit coupling", Phys. Rev. B **71**, 035311 (2005).

[Lan30] L. Landau, "Diamagnetismus der Metalle", Z. Phys. **64**, 629–637 (1930).

[Le +97] P. Le Jeune, D. Robart, X. Marie, T. Amand, M. Brousseau, J. Barrau, V. Kalevich, and D. Rodichev, "Anisotropy of the electron Landé g factor in quantum wells", Semiconductor Science and Technology **12**, 380 (1997).

[Lee+14] K. Lee, B. Fallahazad, J. Xue, D. C. Dillen, K. Kim, T. Taniguchi, K. Watanabe, and E. Tutuc, "Chemical potential and quantum Hall ferromagnetism in bilayer graphene", Science **345**, 58 (2014).

[LFS88] S. E. Laux, D. J. Frank, and F. Stern, "Quasi-one-dimensional electron states in a split-gate GaAs/AlGaAs heterostructure", Surf. Sci. **196**, 101–106 (1988).

[LG08] A. V. Larionov and L. E. Golub, "Electric-field control of spin-orbit splittings in GaAs/Al_xGa_{1-x}As coupled quantum wells", Phys. Rev. B **78**, 033302 (2008).

[Luo+88] J. Luo, H. Munekata, F. F. Fang, and P. J. Stiles, "Observation of the zero-field spin splitting of the ground electron subband in gasb-inas-gasb quantum wells", Phys. Rev. B **38**, 10142–10145 (1988).

[Luo+90] J. Luo, H. Munekata, F. F. Fang, and P. J. Stiles, "Effects of inversion asymmetry on electron energy band structures in GaSb/InAs/GaSb quantum wells", Phys. Rev. B **41**, 7685–7693 (1990).

[MAH14] P. Miro, M. Audiffred, and T. Heine, "An atlas of two-dimensional materials", Chem. Soc. Rev. **43**, 6537–6554 (2014).

[Mei+01] I. Meinel, D. Grundler, D. Heitmann, A. Manolescu, V. Gudmundsson, W. Wegscheider, and M. Bichler, "Enhanced magnetization at integer quantum Hall states", Phys. Rev. B **64**, 121306 (2001).

[Mei+07] L. Meier, G. Salis, I. Shorubalko, E. Gini, S. Schon, and K. Ensslin, "Measurement of Rashba and Dresselhaus spin-orbit magnetic fields", Nat Phys **3**, 650–654 (2007).

[MH00] A. Malinowski and R. T. Harley, "Anisotropy of the electron g factor in lattice-matched and strained-layer III-V quantum wells", Phys. Rev. B **62**, 2051–2056 (2000).

[Mil+03] J. B. Miller, D. M. Zumbühl, C. M. Marcus, Y. B. Lyanda-Geller, D. Goldhaber-Gordon, K. Campman, and A. C. Gossard, "Gate-Controlled Spin-Orbit Quantum Interference Effects in Lateral Transport", Phys. Rev. Lett. **90**, 076807 (2003).

[MOL86] A. H. MacDonald, H. C. A. Oji, and K. L. Liu, "Thermodynamic properties of an interacting two-dimensional electron gas in a strong magnetic field", Phys. Rev. B **34**, 2681–2689 (1986).

[Nit+97] J. Nitta, T. Akazaki, H. Takayanagi, and T. Enoki, "Gate Control of Spin-Orbit Interaction in an Inverted $In_{0.53}Ga_{0.47}As/In_{0.52}Al_{0.48}As$ Heterostructure", Phys. Rev. Lett. **78**, 1335–1338 (1997).

[OHR96] M. Oestreich, S. Hallstein, and W. W. Ruhle, "Spin quantum beats in semiconductors", IEEE J. Sel. Top. Quamtum Electron. **2**, 747–755 (1996).

[Oos+98] T. H. Oosterkamp, S. F. Godijn, M. J. Uilenreef, Y. V. Nazarov, N. C. van der Vaart, and L. P. Kouwenhoven, "Changes in the Magnetization of a Double Quantum Dot", Phys. Rev. Lett. **80**, 4951–4954 (1998).

[Pau58] L. J. van der Pauw, "A method of measuring specific resistivity and Hall effect of discs of arbitrary shape", Philips Res. Repts. **13**, 1–9 (1958).

[PC06] P. Pietiläinen and T. Chakraborty, "Energy levels and magneto-optical transitions in parabolic quantum dots with spin-orbit coupling", Phys. Rev. B **73**, 155315 (2006).

[Pot+96] A. Potts, R. Shepherd, W. G. Herrenden-Harker, M. Elliott, C. L. Jones, A. Usher, G. A. C. Jones, D. A. Ritchie, E. H. Linfield, and M. Grimshaw, "Magnetization studies of Landau level broadening in two-dimensional electron systems", J. Phys.: Condens. Matter **8**, 5189 (1996).

[PZ06] P. Pfeffer and W. Zawadzki, "Anisotropy of spin g factor in GaAs/$Ga_{1-x}Al_xAs$ symmetric quantum wells", Phys. Rev. B **74**, 233303 (2006).

[Rie+97] S. P. Riege, T. Kurth, F. Runkel, D. Heitmann, and K. Eberl, "Confinement potential and surface state density in deep-mesa etched quantum wires", Appl. Phys. Lett. **70**, 111–113 (1997).

[RLZ59] L. M. Roth, B. Lax, and S. Zwerdling, "Theory of Optical Magneto-Absorption Effects in Semiconductors", Phys. Rev. **114**, 90–104 (1959).

[Rös09] U. Rössler, *Solid State Theory* (Springer Berlin Heidelberg, 2009).

[Ruh+06] N. Ruhe, J. I. Springborn, C. Heyn, M. A. Wilde, and D. Grundler, "Simultaneous measurement of the de Haas-van Alphen and the Shubnikov-de Haas effect in a two-dimensional electron system", Phys. Rev. B **74**, 235326 (2006).

[Ruh08] N. Ruhe, "Magnetisierungsmessung zur Untersuchung von Quantisierungs-Effekten in zweidimensionalen Elektronensystemen", Dissertation (Universität Hamburg, 2008).

[Rup+13] B. Rupprecht, S. Heedt, H. Hardtdegen, T. Schäpers, C. Heyn, M. A. Wilde, and D. Grundler, "Frequency anomaly in the Rashba-effect induced magnetization oscillations of a high-mobility two-dimensional electron system", Phys. Rev. B **87**, 035307 (2013).

[Sas+14] A. Sasaki, S. Nonaka, Y. Kunihashi, M. Kohda, T. Bauernfeind, T. Dollinger, K. Richter, and J. Nitta, "Direct determination of spin-orbit interaction coefficients and realization of the persistent spin helix symmetry", Nature Nanotech. **9**, 703 (2014).

[Sav+96] I. G. Savelev, A. M. Kreshchuk, S. V. Novikov, A. Y. Shik, G. Remenyi, G. Kovacs, B. Podor, and G. Gombos, "Spin splitting of the Landau levels and exchange interaction of a non-ideal two-dimensional electron gas in $In_xGa_{1-x}As$/InP heterostructures", J. Phys.: Condens. Matter **8**, 9025–9036 (1996).

[Sch+00] M. P. Schwarz, D. Grundler, I. Meinel, C. Heyn, and D. Heitmann, "Micromechanical cantilever magnetometer with an integrated two-dimensional electron system", Appl. Phys. Lett. **76**, 3564–3566 (2000).

[Sch+02a] M. P. Schwarz, D. Grundler, H. Rolff, M. A. Wilde, S. Groth, C. Heyn, and D. Heitmann, "De Haas–van Alphen effect in a two-dimensional electron system", Physica E: Low-dimensional Systems and Nanostructures **12**, <ce:title>Proceedings of the Fourteenth International Conference on the Ele ctronic Properties of Two-Dimensional Systems</ce:title>, 140–143 (2002).

[Sch+02b] M. P. Schwarz, D. Grundler, M. A. Wilde, C. Heyn, and D. Heitmann, "Magnetization of semiconductor quantum dots", J. Appl. Phys. **91**, 6875–6877 (2002).

[Sch+06] T. Schäpers, V. A. Guzenko, M. G. Pala, U. Zülicke, M. Governale, J. Knobbe, and H. Hardtdegen, "Suppression of weak antilocalization in $Ga_xIn_{1-x}As$/InP narrow quantum wires", Phys. Rev. B **74**, 081301 (2006).

[Sch+98] T. Schäpers, G. Engels, J. Lange, T. Klocke, M. Hollfelder, and H. Lüth, "Effect of the heterointerface on the spin splitting in modulation doped $In_xGa_{1-x}As$/InP quantum wells for B→0", J. Appl. Phys. **83**, 4324–4333 (1998).

[Sch02] F. Schwabl, *Quantenmechanik*, Springer-Lehrbuch (Springer, 2002).

[SEL03] J. Schliemann, J. C. Egues, and D. Loss, "Nonballistic Spin-Field-Effect Transistor", Phys. Rev. Lett. **90**, 146801 (2003).

[SH30] L. Shubnikov and W. J. de Haas, "A New Phenomenon in the Change of Resistance in a Magnetic Field of Single Crystals of Bismuth", Nature **126**, 500 (1930).

[Sho84] D. Shoenberg, *Magnetic Oscillations in Metals* (Cambridge University Press, 1984).

[SI88] U. Sivan and Y. Imry, "de Haas-van Alphen and Aharonov-Bohm-type Persistent Current Oscillations in Singly Connected Quantum Dots", Phys. Rev. Lett. **61**, 1001–1004 (1988).

[SKG04] T. Schäpers, J. Knobbe, and V. A. Guzenko, "Effect of Rashba spin-orbit coupling on magnetotransport in InGaAs/InP quantum wire structures", Phys. Rev. B **69**, 235323 (2004).

[Spr+06] J. I. Springborn, N. Ruhe, C. Heyn, M. A. Wilde, D. Heitmann, and D. Grundler, "Gate-controlled de Haas–van Alphen effect in an interacting two-dimensional electron system", Physica E: Low-dimensional Systems and Nanostructures **34**, 172–175 (2006).

[Spr07] J. I. Springborn, "Magnetometrie an Halbleiter-Nanostrukturen mit wenigen Elektronen", Dissertation (Universität Hamburg, 2007).

[Stö+83] H. L. Störmer, T. Haavasoja, V. Narayanamurti, A. C. Gossard, and W. Wiegmann, "Observation of the de Haas-van Alphen effect in a two-dimensional electron system", J. Vac. Sci. Technol. B **1**, 423–426 (1983).

[Str08] G. Stracke, "Magnetisierungs-Messungen an Feldeffekt-induzierten Quantenpunkten", Diplomarbeit (Universität Hamburg, 2008).

[TA02] S. A. Tarasenko and N. S. Averkiev, "Interference of spin splittings in magneto-oscillation phenomena in two-dimensional systems", Journal of Experimental and Theoretical Physics Letters **75**, 552–555 (2002).

[Tem+87] H. Temkin, G. J. Dolan, M. B. Panish, and S. N. G. Chu, "Low-temperature photoluminescence from InGaAs/InP quantum wires and boxes", Appl. Phys. Lett. **50**, 413–415 (1987).

[Tem88] I. M. Templeton, "A high-sensitivity torsional magnetometer for two-dimensional electron systems", Journal of Applied Physics **64**, 3570–3573 (1988).

[TLG04] E. Tsitsishvili, G. S. Lozano, and A. O. Gogolin, "Rashba coupling in quantum dots: An exact solution", Phys. Rev. B **70**, 115316 (2004).

[UE09] A. Usher and M. Elliott, "Magnetometry of low-dimensional electron and hole systems", J. Phys.: Condens. Matter **21**, 103202 (2009).

[Wei+97] Y. Y. Wei, J. Weis, K. v. Klitzing, and K. Eberl, "Single-electron transistor as an electrometer measuring chemical potential variations", Appl. Phys. Lett. **71**, 2514–2516 (1997).

[WG13] M. A. Wilde and D. Grundler, "Alternative method for the quantitative determination of Rashba- and Dresselhaus spin–orbit interaction using the magnetization", New J. Phys. **15**, 115013 (2013).

[WGH10] M. A. Wilde, D. Grundler, and D. Heitmann, "Magnetization of Interacting Electrons in Low-Dimensional Systems", English, in *Quantum materials, lateral semiconductor nanostructures, hybrid systems and nanocrystals*, edited by D. Heitmann, NanoScience and Technology (Springer Berlin Heidelberg, 2010), pp. 245–275.

[Wie+97] S. A. J. Wiegers, M. Specht, L. P. Lévy, M. Y. Simmons, D. A. Ritchie, A. Cavanna, B. Etienne, G. Martinez, and P. Wyder, "Magnetization and Energy Gaps of a High-Mobility 2D Electron Gas in the Quantum Limit", Phys. Rev. Lett. **79**, 3238–3241 (1997).

[Wil+04] M. A. Wilde, J. I. Springborn, C. Heyn, D. Heitmann, and D. Grundler, "Magnetization of GaAs quantum wires with quasi one-dimensional electron systems", Physica E: Low-dimensional Systems and Nanostructures **22**, 15th International Conference on Electronic Propreties of Two-Dimensional Systems (EP2DS-15), 729–732 (2004).

[Wil+08] M. A. Wilde, J. I. Springborn, O. Roesler, N. Ruhe, M. P. Schwarz, D. Heitmann, and D. Grundler, "Magnetometry on quantum Hall systems: Thermodynamic energy gaps and the density of states distribution", Phys. Status Solidi B **245**, 344–355 (2008).

[Wil+09] M. A. Wilde, D. Reuter, C. Heyn, A. D. Wieck, and D. Grundler, "Inversion-asymmetry-induced spin splitting observed in the quantum oscillatory magnetization of a two-dimensional electron system", Phys. Rev. B **79**, 125330 (2009).

[Wil+14] M. A. Wilde, B. Rupprecht, F. Herzog, A. Ibrahim, and D. Grundler, "Spin–orbit interaction in the magnetization of two-dimensional electron systems", Phys. Status Solidi B **251**, 1710–1724 (2014).

[Wil04] M. A. Wilde, "Magnetization Measurements on Low-Dimensional Electron Systems in High-Mobility GaAs and SiGe Heterostructures", Dissertation (Universität Hamburg, 2004).

[Win03] R. Winkler, *Spin-Orbit Coupling Effects in Two-Dimensional Electron and Hole Systems*, Vol. 191, Springer Tracts in Modern Physics (Springer Berlin Heidelberg, 2003).

[WMR82] O. Wada, A. Majerfield, and P. N. Robson, "InP Schottky contacts with increased barrier height ", Solid-State Electron. **25**, 381–387 (1982).

[Wol+01] S. A. Wolf, D. D. Awschalom, R. A. Buhrman, J. M. Daughton, S. von Molnár, M. L. Roukes, A. Y. Chtchelkanova, and D. M. Treger, "Spintronics: A Spin-Based Electronics Vision for the Future", Science **294**, 1488–1495 (2001).

[YC13] P. Yu and M. Cardona, *Fundamentals of Semiconductors: Physics and Materials Properties* (Springer Berlin Heidelberg, 2013).

[Zha+14] D. Zhang, X. Huang, W. Dietsche, K. von Klitzing, and J. H. Smet, "Signatures for Wigner Crystal Formation in the Chemical Potential of a Two-Dimensional Electron System", Phys. Rev. Lett. **113**, 076804 (2014).

[Zha06] D. Zhang, "Exact Landau levels in two-dimensional electron systems with Rashba and Dresselhaus spin–orbit interactions in a perpendicular magnetic field", J. Phys. A: Math. Gen. **39**, L477 (2006).

Publications

F. Herzog, S. Heedt, S. Goerke, A. Ibrahim, B. Rupprecht, Ch. Heyn, H. Hardtdegen, Th. Schäpers, M.A. Wilde and D. Grundler, "Confinement and inhomogeneous broadening effects in the quantum oscillatory magnetization of quantum dots", Journal of Physics: Condensed Matter **28**, 045301 (2015)

F. Herzog, Ch. Heyn, H. Hardtdegen, Th. Schäpers, M.A. Wilde and D. Grundler, "Micromechanical measurement of beating patterns in the quantum oscillatory chemical potential of InGaAs quantum wells due to spin-orbit coupling", Applied Physics Letters **107**, 092101 (2015)

M.A. Wilde, B. Rupprecht, F. Herzog, A. Ibrahim and D. Grundler, "Spin-orbit interaction in the magnetization of two-dimensional electron systems", Physica Status Solidi B **251**, 1710 (2014)

F. Herzog, M. Bichler, G. Koblmüller, S. Prabhu-Gaunkar, W. Zhou and M. Grayson, "Optimization of AlAs/AlGaAs quantum well heterostructures on on-axis and misoriented GaAs (111)B", Applied Physics Letters **100**, 192106 (2012)

B.A. Young, F. Herzog, P. Friedel, S. Rammensee, A. Bausch, and J.L. van Hemmen, "Tears of Venom: Hydrodynamics of Reptilian Envenomation", Physical Review Letters **106**, 198103 (2011)

F. Herzog, F. Finocchi, L. Soukiassian and O. Pluchery, "The adsorption of a substituted benzene, the ethynyl-trifluoro-toluene on Si(100)-2x1", Surface Science **605**, 166 (2011)

Acknowledgments

I would like to express my thanks and gratitude to all the people who contributed to this work and who supported me during my time as a PhD student. In particular, I want to thank

- Prof. Dr. Dirk Grundler for the opportunity to work on this interesting research topic and for the supervision of my thesis. I thank him for his great support and motivation, the many fruitful discussions we had and his numerous constructive suggestions that always allowed me to improve my work.

- Dr. Marc A. Wilde for the overall support and guidance throughout this work. The countless discussions we had always led to new insights and decisively stimulated main parts of my research. I appreciate his profound knowledge in physics, his detailed experience in engineering and measurement technology, his commitment and encouragement that helped me to move forward and his open door at all times.

- Prof. Dr. Thomas Schäpers and Dr. Hilde Hardtdegen from FZ Jülich for providing the InP/InGaAs heterostructures that formed the basis of the samples investigated throughout this work.

- Sebastian Heedt from FZ Jülich for performing the reactive ion etching on the quantum dot samples and the scientific discussions.

- Christian Heyn from Universität Hamburg for providing the AlGaAs/GaAs heterostructures that were used for the preparation of the cantilever sensors.

- Matthias Brasse, Stephan Albert, Schorsch Sauther and Benedikt Rupprecht, my cantilever co-workers, for the nice working atmosphere, the great support and introduction into the many different

and sometimes delicate preparational and experimental techniques at the early stage of my work at E10.

- Ayman Ibrahim, Susanne Goerke and Hubert Hautmann, diploma and master students, for their commitment and contributions to this work.

- Florian Heimbach for preparing the Al_2O_3 gate-insulating layers for the flip-chip samples by atomic-layer deposition. Apart from that, I want to thank him for the enjoyable time while we shared an office for almost three years. It was a pleasure to work with you!

- Claudine Voelcker, Thomas Rapp, Thomas Neukel, Johannes Seitz, Stephan Lichtenauer and Herbert Hetzl from the E10 organizational and technical staff for the helping hands, the organizational support, quick technical solutions and for thousands of liters of liquid helium.

- Georg Dürr, Rupert Huber, Thomas Schwarze, Florian Brandl, Ioannis Stasinopoulos, Stefan Mändl, Haiming Yu and Vinayak Bhat and all diploma, master, bachelor and exchange students for the exceptionally nice working atmosphere at E10, the many scientific and non-scientific discussions as well as the innumerable coffee-breaks.

- My parents and parents-in-law for their unlimited support and for helping to take care of our children, especially during the time when I was writing up my thesis.

- My wife Melanie for her support, patience, encouragement in any possible aspect, for her expertise in all LaTeX-, TikZ- and any other typesetting-related topics and for just always being there.

This research has received funding from the priority program 1285: "Semiconductor Spintronics", the Transregio program TRR 80: "From Electronic Correlations to Functionality" of the Deutsche Forschungsgemeinschaft and the German Excellence Initiative via Nanosystems Initiative Munich (NIM), which is gratefully acknowledged.